# Batteryless solutions for implantable and wearable wireless medical devices

Luigi Di Trocchio

université de BORDEAUX

# Thèse de Doctorat
## de l'Université de Bordeaux

**École doctorale** des Sciences Physiques et de l'Ingénieur

**Spécialité** Électronique

**Préparée au** Laboratoire IMS

**Par** Luigi Di Trocchio

---

# Batteryless solutions for implantable and wearable wireless medical devices

---

**Sous la direction de** Corinne Dejous , Alexander Kuhn **et** Simon Hemour

**Après l'avis de** Tan-Phu Vuong **et de** Alexandru Takacs

**Soutenue le** 12 décembre 2019

**Devant le comité d'examen formé de :**

| | | |
|---|---|---|
| M. Tan-Phu Vuong | Grenoble INP | Rapporteur |
| M. Alexandru Takacs | Université de Toulouse III Paul Sabatier | Rapporteur |
| Mme. Valérie Vigneras | Bordeaux INP | Examinatrice |
| Mme. Gaëlle Lissorgues | ESIEE-Paris | Présidente de Jury |
| M. Arnaud Vena | IES Montpellier | Examinateur |
| Mme. Claudine Boiziau | INSERM | Invitée |
| Mme Corinne Dejous | Bordeaux INP | Directrice de Thèse |
| M. Alexander Kuhn | Bordeaux INP | Directeur de Thèse |
| M. Simon Hemour | Université de Bordeaux | Co-encadrant |

Thèse réalisée
dans le laboratoire **IMS**
au sein de l'équipe **MDA**.

Université de Bordeaux Laboratoire IMS
CNRS UMR-5218 351,
cours de la Libération
33405 TALENCE Cedex

# Abstract

Electronic medical devices are nowadays blossoming, revolutionizing the way of thinking the healthcare. These innovative devices are increasingly substituting the conventional pharmaceutical approach to monitor and treat various diseases, improving results and limiting side effects. Recently, advances in bioelectronics have brought miniaturized implantable medical devices, which can be placed directly on the desired spot of the body, and wearable solutions, allowing body parameters to be monitored with minimum impact on the patients. Moreover, these devices are now embedding wireless communication capabilities, to facilitate remote monitoring. In order to further improve this technology, one of the most challenging and still not solved design problems is the research of a suitable powering approach, since classical batteries are not the optimal choice due to their size, weight and discharge in time. This dissertation proposes new batteryless solutions for both implantable and wearable wireless medical devices.

On the implantable side, the first steps towards a highly integrated implantable micro-energy platform with communication capabilities are carried out. Two alternatives to batteries were selected to power the device: Wireless Power Transfer (WPT) and glucose Biofuel Cells (BFC). The first involves the transmission of energy from a transmitter to a receiver through an oscillating magnetic field and the second uses living organisms to produce electricity, using glucose and oxygen, both abundant inside the human body. The proposed design is able to merge these two technologies into a single object, having both antenna and electrode capabilities, in order to allow the further miniaturization of the platform by providing a hybrid powering system. Regarding wearable devices, fully-passive Ultra High Frequency Radio Frequency Identification (UHF-RFID) sensor solutions are proposed with application on laboratory rodents and human healthcare.

In this work, the proposed hybrid implantable technology was successfully validated. Improvements of the structure, starting from a simple design, were defined and proven, in order to increase the efficiency of the wireless link. This allows to reduce the impact of dielectric losses associated to the body environment, while keeping the antenna/electrode in contact with the tissues. Moreover, four wearable RFID sensors were developed in order to continuously monitor a BFC implanted in a laboratory rat, leading to successfully monitoring of a BFC in-vivo for about 24 hours. Finally, a passive ultra-low-cost wearable RFID tag, with temperature monitoring capabilities, was also designed and developed using corrugated cardboard as substrate, allowing the easy screening of the human body temperature, for example in developing countries, in case of emergencies or diseases outbreak.

# Keywords

Implantable device, Wearable device, Wireless Power Transfer, Biofuel cell, RFID.

# Résumé

Les dispositifs médicaux électroniques sont aujourd'hui en plein essor, révolutionnant la façon de définir les soins de santé. Ainsi, ces dispositifs innovants remplacent de plus en plus l'approche pharmaceutique conventionnelle pour suivre et traiter diverses pathologies, en améliorant les résultats et en limitant les effets secondaires. Récemment, les avancements en bioélectronique ont permis la création de dispositifs médicaux intra- et extra-corporels de nouvelle génération : des dispositifs miniaturisés sont implantés directement à l'endroit souhaité, des solutions portables à même la peau permettent de suivre les paramètres corporels avec une incidence minimale sur les patients. De plus, ces dispositifs ont également la capacité de communiquer sans fils, facilitant le suivi à distance. Pour améliorer cette technologie, une des plus grandes difficultés de conception, non résolue à ce jour, est la recherche d'une approche adaptée pour alimenter ces dispositifs, puisque les batteries classiques ne sont pas optimales, en raison de leur dimension, leur poids et leur décharge dans le temps. Cette thèse propose de nouvelles solutions sans piles pour alimenter des dispositifs implantables et portables.

Concernant les dispositifs implantables, les premiers pas vers une plateforme à micro-énergie hautement intégrée et dotée de capacités de communication ont été effectués. Deux alternatives aux piles ont été sélectionnées pour alimenter ce dispositif : la récupération d'énergie sans fil et les piles à combustible biologique (biopiles). La première implique la transmission d'énergie à partir d'un émetteur vers un récepteur à travers un champ magnétique oscillant et la deuxième alternative utilise le vivant pour produire de l'énergie, en utilisant le glucose et l'oxygène, tous deux abondants dans le corps humain. Le dispositif proposé fusionne ces deux technologies dans un seul objet, présentant à la fois les fonctionnalités de l'antenne et de l'électrode, permettant ainsi une forte miniaturisation du dispositif en constituant un système d'alimentation hybride. Concernant les dispositifs portables, des capteurs passifs à identification par ultra haute fréquence (UHF-RFID) sont proposés avec une application sur des rongeurs de laboratoire et à la santé humaine.

Dans ce travail, la technologie implantable hybride a été validée avec succès. Les améliorations de la structure à partir d'une conception simple ont été définies et ont permis d'améliorer l'efficacité du lien sans fil. Ces solutions réduisent l'effet des pertes diélectriques associées au milieu corporel, bien qu'elles gardent le contact entre l'antenne/électrode et les tissus. De plus, quatre capteurs RFID portables ont été développés pour suivre en continu une biopile implantée dans un rat de laboratoire, qui a conduit au monitoring d'une biopile in-vivo pendant près de 24 heures. Enfin, un dispositif pour utilisation cutanée, passif, à très faible coût et permettant de suivre l'évolution de la température a été conçu et développé en utilisant du carton ondulé comme support. Ce dispositif permet le suivi de température corporelle, et peut par exemple trouver des applications dans les pays en développement, en cas d'urgence et d'épidémies.

# Mots-clés

Dispositif implantable, Èlectronique médicale, Biopile, Récupération d'énergie sans fils, RFID.

# Résumé substantiel

Une branche importante de la recherche technologique a toujours eu pour objectif l'amélioration des techniques de soins de santé afin d'assurer un diagnostic précoce, précis et efficace et le traitement de certaines maladies. Aujourd'hui, l'électronique fusionne avec la biologie afin de fournir des solutions innovantes pour surveiller les signes vitaux et supplanter les dysfonctionnements des organes.

Les progrès de la bioélectronique au cours de la seconde moitié des années 1900 ont révolutionné la façon de penser les soins de santé, en apportant de nouveaux dispositifs médicaux extra- et intra-corporels. Ces appareils réussissent là où les traitements chimiques classiques échouent et enregistrent avec précision l'activité corporelle, pour suivre la présence d'une pathologie. Ainsi, dans le monde entier, des millions de diabétiques portent des systèmes de surveillance du glucose pour vérifier leur glycémie et des stimulateurs cardiaques aident des centaines de milliers de cœurs à continuer de battre. La stimulation électronique du cerveau est utilisée avec succès pour limiter les tremblements de la maladie de Parkinson et pour aider les patients atteints d'épilepsie, de dépression ou de douleur chronique. Plus récemment, des appareils médicaux électroniques sont également utilisés pour restaurer les sens perdus comme l'ouïe, la vue et le toucher. Beaucoup plus d'applications aujourd'hui, bien d'autres seront proposées à l'avenir. Les progrès des communications sans fil, qui ont amélioré les dispositifs bioélectroniques implantés, ont également joué un rôle clé dans les dispositifs médicaux électroniques portables. Ces appareils sont maintenant programmés à distance et les données collectées par les capteurs peuvent être récupérées sans fil, améliorant le confort du patient et l'efficacité du traitement. Par conséquent, ces technologies améliorent considérablement la qualité de vie des personnes handicapées et prolongent l'espérance de vie de personnes atteintes de certaines maladies.

Le plus grand défi à relever pour continuer de perfectionner cette technologie est la miniaturisation de ce type de capteurs et stimulateurs intelligents, afin de permettre la mise en place de l'implant à l'endroit souhaité du corps, sans provoquer de déplacement des tissus, de dommages ou d'altération des fonctions biologiques. De même, les nouveaux appareils portables miniaturisés et légers peuvent également améliorer considérablement le confort du patient lors du soin, sans contraindre la vie du patient. Les tâches les plus importantes pour y parvenir sont notamment le choix de la source d'alimentation, pour alimenter de manière optimale les appareils, et le moyen de récupérer les informations, en privilégiant une communication sans fil pour éviter les désagréments d'une liaison directe, filaire (ex. gêne, risque

d'infection). Les batteries sont historiquement le moyen le plus courant d'alimenter les appareils, car elles peuvent fournir la quantité d'énergie requise par les circuits électroniques à faible puissance de manière fiable. Cependant, les batteries sont peu efficaces sur le plan énergétique, elles ne sont pas durables et doivent être rechargées/remplacées, exigeant une opération chirurgicale en cas d'implants. De plus, elles occupent un volume souvent supérieur à celui du dispositif électronique lui-même, limitant leur portabilité. Cette recherche vise à concevoir des dispositifs médicaux électroniques sans batterie et sans fil, qui peuvent être facilement portés ou implantés, tout en minimisant les effets collatéraux.

La récupération d'énergie d'une source externe peut être une solution pour réduire la présence des batteries. Dans ce cas, un émetteur dédié est couplé au dispositif récepteur médical qui récupère la puissance nécessaire. De nombreuses solutions ont été proposées pour y parvenir, en utilisant des techniques différentes, sur la base de liaisons électromagnétiques, acoustiques ou optiques. Une telle liaison sans fil peut également être utilisée comme canal de communication. Néanmoins, une source d'alimentation extérieure au corps est constamment requise et doit être correctement couplée aux dispositifs implantés, c'est-à-dire alignée sur le faisceau d'ondes transmis et sans atténuation excessive. Fournir la quantité d'énergie requise est difficile, en raison des caractéristiques diélectriques et mécaniques du corps humain.

Une alternative consiste à produire de l'électricité sur site, par grappillage d'une ou plusieurs énergies disponibles à proximité, par exemple solaire, chimique ou cinétique. Dans ce cas, aucun couplage avec l'émetteur n'est nécessaire, les dispositifs sont alors complètement autonomes. Cependant, ces techniques présentent également de nombreux inconvénients. Les densités de puissance pouvant être atteintes sont beaucoup plus faibles que celles obtenues par liaisons sans fil, limitant la miniaturisation du dispositif, en particulier dans le cas d'implants, et cette approche n'offre pas de possibilité de communication.

Cette thèse présente une nouvelle philosophie d'alimentation, en se concentrant sur les dispositifs médicaux intra- et extra-corporels sans fil et sans batterie. Pour le scénario intra-corporel, une nouvelle approche hybride est proposée, combinant des techniques de récupération d'énergie avec et sans source externe. Dans ces conditions, la liaison sans fil peut fournir de l'énergie à la charge et permettre la fonctionnalité de communication. D'un autre côté, la dépendance de la position de l'implant par rapport à la source externe d'énergie est limitée par la présence d'un générateur autonome, de faible puissance. Ainsi, pour assurer la sécurité de fonctionnement, une source d'alimentation interne peut sécuriser les dispositifs implantés en cas de défaillance temporaire de la liaison sans fil. L'implant peut alors être conçu pour offrir deux modes de fonctionnement distincts : un mode de faible puissance, avec des fonctionnalités limitées (actif lorsque la source dédiée externe n'est pas présente), et un mode de fonctionnement complet à plus haute puissance (actif en présence de l'émetteur externe). Dans ce travail, le couplage par résonance magnétique en champ proche a été sélectionné comme approche de transmission de puissance sans fil et la pile à combustible biologique (biopile) au glucose pour la cellule autonome. Le premier vise un maximum d'efficacité

de transfert de puissance tout en limitant les effets biologiques négatifs, la seconde utilise du glucose et de l'oxygène, tous les deux largement disponibles dans le corps humain, pour produire en continu de l'énergie.

Ce manuscrit décrit pour la première fois un prototype qui, non seulement combine ces deux fonctions, mais les intègre également dans le même support physique, ouvrant la voie à une miniaturisation critique des dispositifs. Dans ce cas, l'implant peut fonctionner en continu (par exemple en collectant les informations, alimenté par la pile à biocarburant) et, si nécessaire, l'émetteur externe peut être couplé à l'implant, augmentant la puissance disponible et permettant notamment la manipulation et la récupération de l'information.

En ce qui concerne les dispositifs portables, deux plateformes de détection sans fil et sans batterie différentes ont été développées, toutes deux utilisant des techniques de radio-identification par radiofréquence (RFID) passive en champ lointain. Le premier dispositif est un élément clé dans la conception d'une configuration de mesure sans fil pour surveiller en continu des biopiles implantées dans des rongeurs de laboratoire, qui seront celles utilisées pour le développement du dispositif implanté hybride. Le second est lié aux soins de santé humaine, proposant un nouveau capteur de température corporelle à très faible coût pour le dépistage massif de la température d'une population dans les pays émergents ou les zones touchées par des catastrophes.

Le premier chapitre présente le contexte scientifique, en différenciant les dispositifs intra- et extra-corporels. Les premiers sont décrits d'abord en présentant les applications les plus courantes actuellement, comme les implants cardiaques, les implants pour la stimulation neurologique et les pompes à insuline pour les diabétiques. Pour chaque application, la technique habituellement utilisée pour alimenter le dispositif est aussi présentée.

Puis, les alternatives existantes aux batteries sont analysées pour les dispositifs médicaux, en les divisant en systèmes autonomes (sans besoin de source externe) et à transfert d'énergie sans fil. Dans la première catégorie, une attention particulière est dédiée aux piles à biocarburant (biopiles) de type glucose enzymatique, utilisées dans le cadre de cette thèse, et aux approches de transfert d'énergie sans fil, par liaison optique, par ultrasons et par ondes électromagnétiques. Cette dernière approche est particulièrement développée, car utilisée pour la conception des dispositifs présentés dans les chapitres suivants. Les implants médicaux hybrides sont ensuite introduits, utilisant au moins deux approches énergétiques afin de limiter les limitations d'une technique unique et notamment de maximiser la puissance disponible pour ces dispositifs. De cette synthèse de la littérature, il est conclu qu'un implant hybride qui présente au moins une approche énergétique autonome et une technologie de récupération d'énergie sans fil n'a pas encore été développé, justifiant la nouveauté de ces travaux.

Les stratégies de conception des dispositifs de transfert d'énergie sans fil en champ proche pour les implants sont ensuite décrites. Dans un premier temps, les propriétés diélectriques des tissus biologiques sont présentées, en particulier la constante diélectrique et les pertes qui les caractérisent. Le non-magnétisme des tissus est également mis en avant, justifiant le choix d'une liaison magnétique pour alimenter les implants. Puis, une étude bibliographique est développée afin

de présenter les paramètres importants de la conception de tels dispositifs. Ceux développés dans la littérature sont classés par leur taille : avec une dimension de l'ordre de quelques centimètres, et de quelques millimètres (objet de cette étude). La fréquence de fonctionnement est un des paramètres les plus importants, elle est présentée à partir des structures existantes, les meilleures performances étant obtenues pour des fréquences allant de quelques MHz à quelques GHz. Des stratégies de conception pour limiter l'effet de la présence des tissus sur le récepteur sont proposées. On observe que la présence d'une couche de revêtement diélectrique peut améliorer les caractéristiques des dispositifs, en limitant la présence de pertes dues aux tissus biologiques. Bien que cette solution soit largement utilisée dans les dispositifs de la littérature, aucune étude approfondie n'a été menée. Pour compléter cette partie, une stratégie de design des implants est présentée, permettant de séparer la conception du transmetteur et du récepteur.

Enfin, le premier chapitre est terminé par des exemples de capteurs portables, avec une attention particulière sur les solutions sans batterie basées sur des capteurs passifs à identification par ultra haute fréquence (UHF-RFID). Les appareils existants sont passés en revue et leurs stratégies de conception sont décrites. En particulier le paramètre le plus important pour le design d'un dispositif de ce genre, est le gain réalisé de l'antenne RFID, c'est-à-dire le produit entre le gain de l'antenne portable et l'adaptation d'impédance entre l'antenne et la puce RFID.

Le deuxième chapitre porte sur la conception et le développement d'une configuration de mesure sans fil qui permet la surveillance continue d'une biopile implantée dans un rongeur (rat) de laboratoire. Le chapitre présente le flux de développement, décrivant les antennes et les configurations proposées. La technologie sélectionnée est le UHF-RFID passif, pour éviter l'utilisation de piles afin d'améliorer l'acceptabilité par l'animal. La configuration principale est constituée de deux antennes : une antenne connectée au lecteur RFID et placée au dessus de la cage du rat interroge et alimente la deuxième antenne. Celle-ci est positionnée sur un gilet, spécialement développé pour et porté par l'animal, qui comprend aussi le système de télémétrie, c'est-à-dire la puce RFID connectée aux électrodes de la biopile, implantées sous la peau du rat. De cette façon, l'activité de la biopile est enregistrée en continu, sans fil, pendant que l'animal est libre de se déplacer à l'intérieur de la cage. La partie la plus difficile de ce travail est le design de l'antenne portable, du fait des caractéristiques diélectriques des tissus biologiques. En conséquence, un effort particulier a été dédié à la conception de cette antenne. Au cours de la thèse, quatre antennes ont été réalisées et caractérisées.

La première antenne, un dipôle avec une boucle, a été conçue pour permettre la validation de la méthodologie de simulation et de mesure. Elle a été dimensionnée en prenant en considération les dimensions du rat, l'impédance de la puce RFID et le rayonnement de l'antenne. Après simulations, elle a été développée et testée in vivo. Un très bon accord entre les simulations et les mesures a été observé, ainsi que la forte influence des tissus sur les caractéristiques électroniques de l'antenne. En prenant en compte ces résultats, un deuxième système de télémétrie a été conçu, avec une attention particulière pour limiter l'influence de l'animal sur l'antenne portable. Aussi, une antenne patch a été proposée pour le côté lecteur et une antenne à fente de type CSSR (complementary split-ring resonators) avec plan

de masse pour le tag. La présence du plan de masse limite les pertes dues à la forte constante diélectrique du rat. Les antennes réalisées ont été caractérisées et montrent une efficacité de transfert de puissance bien plus élevée que la valeur minimale requise pour effectuer une mesure de la totalité de la surface de la cage. Néanmoins, la présence du plan de masse et d'une antenne volumineuse limitent la portabilité de ce système.

Pour augmenter la portabilité du système de télémétrie, une nouvelle antenne a été conçue. De type boucle carrée (39,4x39,4 cm) excitée par un dipôle, très fine et pliable, elle est destinée à être placée à un millimètre de la peau (épaisseur du gilet) avec un effet minimal sur le comportement de l'animal. Cependant, l'absence de plan de masse rend cette structure fortement altérée par les tissus, impliquant une distance de lecture maximale plus faible que l'antenne précédente. Le tag RFID a été dimensionné et validé lorsqu'il est placé sur un bras humain et dans le cas réel, sur un animal. Une lecture de température a été effectuée avec succès dans les deux cas, avec une distance de lecture maximale d'environ 45 cm, assez grande pour l'application sélectionnée.

La dernière antenne conçue est de type monopole et est plus petite (42x21,5 cm). Avec les mêmes caractéristiques de portabilité que l'antenne précédente, elle atteint une distance de lecture maximale de 60 cm. Cette antenne a été utilisée pour la validation in vitro et in vivo dans le cadre de l'application sélectionnée. En particulier, la tension en circuit ouvert délivrée par une biopile a été enregistrée, pendant qu'elle était placée dans un liquide tampon phosphate saline (PBS) (in vitro) et implantée dans un rat (in vivo). Dans les deux cas la liaison RFID ainsi que la surveillance de la biopile, effectuée pendant près de 24 heures, ont été validées. En particulier, les valeurs de tensions enregistrées in vitro et in vivo montrent une très bonne concordance. En outre, la mesure in vivo démontre la capacité à surveiller l'animal dans n'importe quel endroit de la cage où il se trouve, validant ainsi la conception proposée.

Le troisième chapitre est consacré à la conception de la première plateforme hybride implantable de taille de l'ordre du millimètre. A partir de l'analyse des différentes alternatives aux batteries pour alimenter un dispositif médical électronique, une solution autonome et une autre de transfert d'énergie sans fil ont été sélectionnées : les biopiles et le couplage de résonateurs magnétiques en champ proche, présentés dans le premier chapitre. Le plus grand défi est de fusionner ces deux approches dans la même structure, afin de maximiser la miniaturisation de l'implant. Les contraintes les plus importantes ont alors été définies, ce qui a conduit à la conception d'une ligne de transmission dédiée, imperméable à l'eau, qui a permis la caractérisation des structures conçues.

La suite du chapitre est dédiée à la démonstration de faisabilité du concept de la plateforme hybride. Un fil d'or de 250 micromètres a été sélectionné pour les électrodes de la biopile. Ce fil a été aussi enroulé en forme de bobine pour réaliser l'antenne couplée avec la source externe. Les deux bobines obtenues ont été modifiées avec les enzymes pour obtenir la biopile. Le concept a été démontré, les résultats sont présentés, montrant une efficacité du transfert de puissance sans fil faible, à cause des pertes du milieu simulant la présence des tissus biologiques.

Une possible solution pour augmenter le facteur de qualité des bobines implan-

tées, et donc l'efficacité du lien, est présentée par la suite, et plus particulièrement une configuration à double bobine. Cette configuration permet de dissocier la bobine résonante de la charge résistive, et ainsi d'augmenter le facteur de qualité de l'implant. Cette solution a été démontrée, en mettant en évidence une meilleure efficacité par rapport à la structure à bobine unique utilisée pour la démonstration de faisabilité du concept.

Dans le quatrième chapitre, une autre amélioration du dispositif hybride est décrite pour augmenter l'efficacité de la récupération d'énergie sans fil en champ proche, toujours en utilisant l'antenne comme électrode. Cette solution se base sur l'isolation du champ électrique par des structures diélectriques à faibles pertes, afin de limiter les pertes dues aux tissus. Cette structure, conçue sous forme de vis afin d'optimiser l'occupation de volume interne à la bobine, est placée à l'intérieur de l'antenne implantable, où le champ électrique est maximal. Après la définition de la structure diélectrique, les bases théoriques pour le choix de la forme et du matériel sont présentées, ainsi que des simulations montrant l'intérêt de l'objet conçu.

La structure a ensuite été optimisée en prenant en compte un cas réel : pour la première fois, le volume global de l'implant (bobine et diélectrique) est considéré et les meilleures caractéristiques physiques compatibles avec ce volume sont recherchées. Pour trouver l'optimum, une figure de mérite (FoM) a été définie, elle prend en compte le facteur de qualité du récepteur ainsi le facteur de couplage entre le transmetteur externe et l'implant. Les structures simulées ont été fabriquées en utilisant l'impression 3D et mesurées dans de la viande hachée, pour simuler les tissus musculaires humains. Les mesures ont montré un bon accord avec les simulations, confirmant l'obtention d'une structure optimale.

Pour conclure le chapitre, une application réelle de la structure est démontrée, au-delà de la plateforme hybride. Le dispositif conçu a été utilisé pour mesurer l'impédance de tissus ex vivo, en particulier d'un cœur porcin. Cette application pourrait être utilisée pour surveiller la formation de fibrose des tissus en réponse à une implantation d'un système médical électronique.

Enfin, le cinquième et dernier chapitre présente une extension aux applications humaines des capteurs UHF-RFID passifs présentés dans le deuxième chapitre de cette thèse. Un capteur de température corporelle à très faible coût de fabrication a été développé. Ce capteur adresse le contrôle de masse de la température en cas d'épidémie, avec une attention particulière pour les pays en voie de développement. Pour contenir le coût du tag RFID, le carton ondulé a été choisi comme substrat, car localement disponible (récupérable) partout, et l'antenne a été conçue comme une mono-pièce de scotch en cuivre réalisable par découpe, avec la puce RFID assemblée par brasage possible manuellement. L'opérateur peut ainsi découper le carton à la dimension nécessaire et coller le scotch de cuivre correctement positionné sur les deux surfaces du carton pour obtenir l'antenne.

L'antenne a été conçue à partir de l'antenne CSSR présentée dans le deuxième chapitre, qui a été dimensionnée pour adapter l'impédance à celle de de la puce et maximiser la distance de lecture. Le plan de masse permet le blindage par rapport aux tissus, et ainsi une distance plus longue de lecture. L'antenne, optimisée par simulations, a été réalisée et caractérisée lorsque portée par un sujet sur différentes

zones du corps. Les mesures ont mis en évidence un très bon accord avec les simulations et une distance de lecture maximale d'environ 1,2 m, quand le tag est placé sur le front. Cette distance est largement suffisante pour l'application sélectionnée.

Pour valider le design, des mesures de température ont été effectuées dans un scénario réaliste, avec l'antenne placée sur un patient à différents endroits du corps. Les résultats ont montré que le capteur est capable de surveiller la température corporelle, mais qu'un étalonnage est nécessaire.

En conclusion, cette thèse offre de nouvelles solutions et perspectives pour le développement de systèmes médicaux électroniques intra- et extra-corporels. Pour la partie implantable, une nouvelle solution d'alimentation des capteurs sans utiliser de batteries a été développée. Une approche hybride a notamment montré la possibilité d'alimenter ces implants sans dépendre en continu d'une source externe. Pour les dispositifs portables, de nouvelles solutions passives ont été conçues pour la surveillance des animaux de laboratoire ainsi que l'homme. Toutes les structures proposées ont été validées par des mesures, qui ont systématiquement été comparées avec la théorie et/ou des simulations, en montrant à chaque fois un très bon accord entre les deux.

A partir de ces travaux, de nombreuses perspectives sont proposées. La principale limitation aujourd'hui est liée à la durée de vie de la biopile, dont la prolongation permettra d'envisager des applications sur de longues durées. Indépendamment de la biopile, les solutions proposées pourront être adaptées pour de nombreuses autres applications. Par exemple, le suivi à distance de différents paramètres vitaux sur une population (pandémie, etc.) ou de nouveaux dispositifs médicaux autonomes intra- et extra-corporels sont envisagés.

# Contents

**List of Figures** 16

**List of Tables** 18

**Abbreviations** 19

**Introduction** 20

**1 Scientific context** 23
1.1 Implantable Medical Devices . . . 23
1.1.1 Applications and conventional powering overview . . . 24
1.1.2 The powering challenge: batteryless implantable devices . . . 26
1.1.3 Hybrid powering of Implantable Medical Devices (IMDs) . . . 31
1.2 Design strategies for a near-field Wireless Power Transfer (WPT) link to power an IMD . . . 33
1.2.1 Dielectric properties of body tissues . . . 33
1.2.2 Best frequency and receiver structure . . . 34
1.2.3 Strategies to limit the effect of body tissues at the receiver side . . . 36
1.2.4 Separation of the Transmitter (TX) and Receiver (RX) coil design . . . 37
1.3 Wearable medical devices . . . 38
1.3.1 Wearable passive Ultra High Frequency (UHF)-Radio Frequency Identification (RFID) sensors . . . 38
1.3.2 Key parameters for the wearable UHF-RFID sensors design . . . 40
1.4 Research context . . . 41
1.4.1 Research partners . . . 41
1.4.2 Research projects . . . 42

**2 Wireless *In-vivo* biofuel cell monitoring** 43
2.1 Introduction to the experiment . . . 43
2.2 Simulation and measurement methodology validation . . . 44
2.2.1 Simulations performed . . . 45
2.2.2 Construction and measurements . . . 45
2.2.3 Conclusion . . . 47
2.3 Complementary Split Ring Resonator Antenna . . . 47
2.3.1 Design of the monitoring system . . . 48

2.3.2 Results . . . 50
2.3.3 Conclusion . . . 52
2.4 Wearable loop antenna . . . 52
2.4.1 Introduction . . . 52
2.4.2 Tag antenna design . . . 53
2.4.3 Tag fabrication and measurement performed . . . 54
2.4.4 Results . . . 55
2.4.5 Conclusion . . . 55
2.5 Wearable monopole antenna . . . 55
2.5.1 Tag antenna design . . . 55
2.5.2 RFID link validation . . . 59
2.5.3 Preliminary *in-vivo* measurements . . . 60
2.5.4 *In-vitro* and *in-vivo* biofuel cell monitoring . . . 61
2.5.5 Conclusion . . . 64
2.6 Conclusion of Chapter 2 . . . 64

**3 Biofuel cell antenna project** **66**
3.1 Background . . . 66
3.2 Experiment constraints . . . 68
3.2.1 Electrochemical constraints . . . 68
3.2.2 Electromagnetic constraints . . . 68
3.3 The proposed stripline structure . . . 70
3.3.1 Design of the transmission line . . . 71
3.3.2 Mechanical problems encountered and measurements performed . . . 72
3.3.3 Conclusion . . . 73
3.4 Proof of concept of the experiment . . . 73
3.4.1 Design of the experiment . . . 73
3.4.2 Results . . . 76
3.4.3 Conclusion . . . 78
3.5 High-Q coil structure . . . 78
3.5.1 Background . . . 78
3.5.2 Design of the receiver devices . . . 79
3.5.3 Results . . . 81
3.5.4 Conclusion . . . 83
3.6 Conclusion of Chapter 3 . . . 83

**4 The Threaded-Furrow Geometry** **85**
4.1 Introduction . . . 85
4.2 The proposed structure . . . 85
4.2.1 The role of the quality factor . . . 86
4.2.2 The Threaded-Furrow dielectric structure . . . 87
4.2.3 Validation of the structure . . . 88
4.3 Design of the receiver at constant volume . . . 91
4.3.1 The design at constant volume . . . 91
4.3.2 Simulation results . . . 92
4.4 Measurements . . . 95

4.4.1 Experimental setup . . . 95
4.4.2 Results . . . 95
4.5 Application . . . 98
4.5.1 Bioimpedance measurements of a swine heart . . . 99
4.5.2 Conclusion . . . 100

**5 Low-cost UHF RFID temperature sensor 102**
5.1 Introduction . . . 102
5.2 Tag design . . . 104
5.2.1 Design constraints and needs . . . 104
5.2.2 The proposed tag antenna . . . 105
5.2.3 Tag antenna dimensioning . . . 107
5.3 Antenna characterization . . . 108
5.3.1 VNA measurements and results . . . 108
5.3.2 Radiation characterization . . . 109
5.4 Temperature measurements . . . 111
5.5 Conclusion . . . 113

**Conclusion 114**

# List of Figures


1.1 IMD powering approaches. . . . . 26
1.2 Working principle of a glucose Biofuel cell (BFC). . . . . 28
1.3 Typical application of an implanted near-field WPT system. . . . . 30
1.4 The dielectric permittivity and conductivity of fat and muscle tissue. 34
1.5 Functional principle of an UHF-RFID sensor network. . . . . 39

2.1 The setup of the proposed telemetry system. . . . . 44
2.2 The dipole antenna. . . . . 45
2.3 The antenna measurements . . . . . 46
2.4 The rat during a measurement. . . . . 47
2.5 The dipole antenna input impedance . . . . . 48
2.6 The slot antenna . . . . . 49
2.7 The measurement setup for the slot antenna . . . . . 50
2.8 Simulated and measured reflection coefficients of the developed slot antenna. . . . . 51
2.9 The slot antenna transmission measurements . . . . . 51
2.10 The wearable loop antenna . . . . . 54
2.11 The wearable loop antenna measurements . . . . . 56
2.12 The wearable monopole antenna . . . . . 58
2.13 The monopole antenna RFID link validation . . . . . 59
2.14 The implantation of the Zn-Cu electrodes inside the rat and the measurement of the open circuit voltage. . . . . 60
2.15 The wireless measurement of subcutaneous implantation of two electrodes in the rat . . . . . 61
2.16 The *in-vitro* and *in-vivo* biofuel cell monitoring setup . . . . . 62
2.17 The *in-vitro* and *in-vivo* BFC wirelessly monitoring results . . . . . 63

3.1 The two different powering levels of the proposed hybrid-powered IMD. . . . . 67
3.2 The experiment constraints . . . . . 69
3.3 The stripline transmission line . . . . . 70
3.4 The designed stripline structure, exploded view . . . . . 71
3.5 The built stripline prototype . . . . . 72
3.6 The setup for the Biofuel Cell Antenna (BCA) experiment. . . . . 74
3.7 The biofuel cell antenna experiment . . . . . 75
3.8 The electrochemical results. . . . . 77
3.9 The power transfer efficiency with respect to frequency . . . . . 77

3.10 acmcr-WPT link. . . . . 79
3.11 The 2-coil receiver system . . . . . 80
3.12 The effect of the phase offset application in order to correctly measure the Q factor of the structures. . . . . 81
3.13 The results obtained. . . . . 82

4.1 The proposed dielectric structure. . . . . 88
4.2 The simulation results. . . . . 89
4.3 The simulated energies and power. . . . . 90
4.4 The measurement of the proposed structure. . . . . 91
4.5 The design at constant volume. . . . . 92
4.6 The resulting simulated Figure of Merit in muscle tissue. . . . . 93
4.7 The simulated maximum Figure of Merit (FoM) and the corresponding $Q$ at constant volume in different tissue environments. . . . . 94
4.8 The built prototypes. . . . . 96
4.9 Measurement results 1. . . . . 97
4.10 Measurement results 2. . . . . 98
4.11 The bio-impedance measurement on a swine heart. . . . . 100
4.12 The measured bio-impedance magnitude and phase. . . . . 101

5.1 The setup of the proposed temperature screening system. . . . . 103
5.2 The proposed patch tag . . . . . 106
5.3 The simulation results. . . . . 107
5.4 The fabricated tag antenna . . . . . 109
5.5 The tag characterisation. . . . . 110
5.6 The measured realized gain. . . . . 112
5.7 The validation of the temperature monitoring system. . . . . 112

# List of Tables

2.1 The results of the validation procedure. . . . . 47
2.2 The dimensions of the designed antennas, including the lumped capacitor and inductor. . . . . 58

3.1 The resulting dimensions of the stripline, the size names refer to Fig. 3.3a. . . . . 71
3.2 The dimensions of the developed structures. . . . . 80
3.3 The comparison between this work and 4-coil structures present in the literature. . . . . 83

# Abbreviations

| | |
|---|---|
| ADC | Analog-to-Digital converter |
| BCA | Biofuel Cell Antenna |
| BFC | Biofuel cell |
| BOD | Bilirubin Oxydase |
| EM | Electromagnetic |
| EMA | European Medicines Agency |
| EMD | Electronic Medical Device |
| FDA | Food and Drug Administration |
| FoM | Figure of Merit |
| GOx | Glucose Oxidase |
| IC | Integrated Circuit |
| IMD | Implantable Medical Device |
| MCR | Magnetically Coupled Resonant |
| PBS | Phosphate-Buffered Saline |
| PTE | Power Transfer Efficiency |
| RF | Radio Frequency |
| RFID | Radio Frequency Identification |
| RR | Reading Range |
| RX | Receiver |
| TFG | Threaded-Furrow Geometry |
| TX | Transmitter |
| UHF | Ultra High Frequency |
| VNA | Vector Network Analyzer |
| WBAN | Wireless Body Area Network |
| WMD | Wearable Medical Device |
| WPT | Wireless Power Transfer |

# Introduction

An important branch of the technological research has always aimed to improve the healthcare techniques in order to insure early, precise and effective diagnostic and treatment. The origin of this can be addressed to the invention of the thermometer, by the Italian scientist Galileo Galilei in 1593, used in the beginning of the XVII century by another Italian inventor, Santorio Santorio, to first monitor the body temperature. A few centuries later, the newborn electronics merged with biology in order to provide innovative solutions to monitor the vital signs and to supplant organ dysfunctions.

The advancements in bioelectronics through the second half of 1900s have revolutionized the way of thinking the healthcare, bringing new portable and implantable medical devices. These devices succeed where the classical chemical treatments fail and accurately record the body activity, to keep trace of the presence of a pathology. Glucose monitoring systems are worn by millions of diabetic people around the word to check their blood sugar levels and cardiac pacemakers helps myriads of hearts to keep beating. Brain electronic stimulation is successfully used to limit Parkinson's disease tremors and to help patients effected by epilepsy, depression or chronic pain. More recently, electronic medical devices are also used to restore lost senses like hearing, sight and touch. A lot more applications are nowadays used and many more will be proposed in future. The advancements in wireless communications, that improved bioelectronics implantable devices, have also played a key role in portable electronic medical devices. These devices are now remotely programmed and the data collected by sensors can be retrieved without wires, improving the patient comfort and the treatment efficacy. Therefore, these technologies are drastically improving the life quality of people with disabilities, and they are also greatly prolonging the life expectation in presence of a particular diseases.

The key feature to unlock the major drawback of this technology is the miniaturization of those kind of smart sensors and actuators, in order to allow the placement of the implant on the desired spot of the body, without causing tissue displacement, damage or altering the normal biological functions. Similarly, new miniaturized and lightweight wearable devices can also drastically improve the patient comfort on provide care, without modifying patient's normal behaviors. Some of the biggest tasks to achieve this are the choice of the power source, to optimally power the devices, and the mean to retrieve the information, i.e. the wireless communication, since any direct link, by means of wires, are unwanted. Batteries

are historically the most common mean to power the devices, because they can provide the fair amount of energy required by low power/low duty cycle electronic circuits in a reliable way. However, battery are energy inefficient, unsustainable and need to be recharged/replaced, demanding surgery in case of implants. They are big, often occupying much more volume than the device itself, and bulky, thus limiting their wearability. To overcome this, this research is aiming to design wireless batteryless electronic medical device, that can be easily worn or implanted, minimizing their collateral effects.

Harvesting the power from an external source could be a possible solution to minimize the presence of the batteries. In this case a dedicated transmitter is coupled to the medical receiver device that retrieves the needed power. Many different solutions has been successfully proposed to accomplish this, using many different techniques, e.g. electromagnetic link, acoustic links and even with light. Moreover, this wireless link can also be used on a communication channel. On the other hand, an external power source outside the body is constantly required, and it needs to be correctly coupled, i.e. aligned, to the implanted devices. Furthermore, delivering the required amount of energy is highly challenging, due to the dielectric and mechanical characteristics of the human body.

A possible alternative is to generate power *on-site*, often scavenging other energy sources available in the direct environment of the device, e.g. solar, chemical, kinetic. In this case, no coupling with the transmitter is needed, thus the devices are completely autonomous. Unfortunately, these techniques present also many downsides. The power densities that can be achieved are much smaller than the one obtained trough wireless links, thus limiting the device miniaturization especially in case of implants, and no channel is ready for communication.

This dissertation presents a novel powering philosophy, focusing on implanted medical devices, and new completely batteryless wearable wireless sensors.

For the implant scenario, a new hybrid-powered approach is proposed, combining wireless and autonomous harvesting techniques. Under this conditions, the wireless link can deliver high power levels to the load, and provide the communication functionality. On the other hand, the position-dependent power source-to-implant is seconded with an autonomous (low power) generator. In fact, to ensure safe operation, a inner power source can secure the implantable devices in case of temporary failure of the wireless link. The implant can also be designed to have two different operational modes: a low-power one, with limited features (active when the external dedicated source is not present), and a high-power full-operational mode (active in presence of the transmitter). In this work near-field magnetically resonant coupling was selected as wireless power approach, and glucose biofuel cell for the autonomous one. The first can achieve high power transfer efficiency, delivering high amount of energy to the load, and the second use glucose and oxygen, both widely available in human body, to continuously produce energy.

This manuscript describe for the first time a prototype that not only combine those two functions, but also integrate them in the same physical medium, leading the way for critical miniaturization of the devices. Moreover, in this case, the implant can operate continuously (e.g. collecting the information, powered by the

biofuel cell) and, when required, a transmitter can be coupled to the implant, boosting the available power and allowing the manipulation and retrieve of the information.

Regarding wearable devices, two different batteryless wireless sensing platforms have been developed, both upon using far-field passive Radio Frequency Identification (RFID) techniques. The first is a key element in the design of a wireless measurement setup that continuously monitors biofuel cells implanted in laboratory rodents. In fact, the implanted biofuel cell to be monitored is the one eventually used to the development of the hybrid powered implanted device. The second device is related to human healthcare, proposing a new ultra-low-cost body temperature sensor for massive population temperature screening in emerging countries and post-disaster areas.

This dissertation is organized as follows. The first chapter introduces the scientific context, by differentiating implantable and wearable devices. The first is described through the most common currently applications, and existing alternatives to batteries are analyzed, with special attention to hybrid solutions. The design strategies of implantable near-field electromagnetic links is then reported. Finally, wearable devices are presented, with special attention on batteryless solutions based on RFID sensors. Existing devices are reviewed, and their design strategies are described.

In the second chapter, the design and development of a wireless measurement setup that allows the continuous monitoring of a biofuel cell implanted in a laboratory rodent is shown. The chapter presents development flow, describing the proposed antennas and setups. The deployment of the wireless monitoring setup is then reported, including the monitoring of a biofuel cell *in-vitro* and *in-vivo* during 24 hours.

The third chapter is dedicated to the actual technical design of the hybrid power platform. Design constraints are defined and resulting design choices are presented. A structure characterized by high quality factor, based on two resonators, is implemented to increase the power transfer efficiency.

In the fourth chapter, an improvement of the hybrid device is described, to boost the near-field link efficiency. This chapter includes theoretical bases, simulations and measurements of an optimum device structure, optimized by taking into account the whole implant volume. An alternative application to this device is also presented, including *ex-vivo* impedance measurements on animal tissues.

The fifth and last chapter presents a passive body temperature sensor. Widely available corrugated cardboard is selected as a substrate and the tag antenna is fabricated using simple adhesive copper tape (becoming an "antenna sticker"). The sticker can be attached to the substrate to implement the whole tag. Design and simulations are validated through measurement and proof-of-concept is demonstrated in a real case scenario.

# Chapter 1

# Scientific context

Electronic Medical Devices (EMDs) are used today as a common practice in clinical application. These devices are designed and used to perform different functions such as continuous monitoring of vital signs, or treatment of various diseases [1, 2]. EMDs are currently successfully used to treat diseases that do not respond well to chemical treatments [3] and also allow continuously monitoring of vital signs and parameters (glucose [4], vital sign monitoring review [5]).

In the past decades, new small, light, portable and intelligent devices have been proposed, having also wireless capabilities, opening the path to a complete echosystem of biosensors and/or bioactuators described as the Wireless Body Area Network (WBAN) [6]. Moreover, the miniaturization of these devices allows the development of solutions that do not interfere with the everyday life of the patient wearing it, drastically increasing their quality of life [7]. More recently, new solutions have been proposed to power the EMDs, replacing batteries by alternative power sources, further decreasing the dimension and weight of these devices [8].

Wireless portable devices can be divided in two main categories: Wearable Medical Devices (WMDs), placed on the outside of the body, in direct contact or close to the skin, and Implantable Medical Devices (IMDs), implanted inside the body, for various biomedical applications [9]. The next sections present this class of devices, with particular attention to batteryless systems.

## 1.1 Implantable Medical Devices

In the past years, the advancements in biomedical implantable electronic devices have blossomed [10]. This has led to a drastic improvement in health monitoring, moving the measurements from outside the body to directly *on-site*. In fact, the limitation of monitoring parameters that are only available from the outside of the body is the main downside of wearable devices, while IMDs are able to directly monitor or stimulate the targeted body part. Therefore, IMDs are now gaining more attention as an alternative to chemical treatment. These devices can be placed all over the body, from the subcutaneous areas [11], to deeper zones like heart [12] or brain [13]. In order to correctly place them, IMDs can be implanted, injected or ingested [14].

### 1.1.1 Applications and conventional powering overview

Since the first implantation of a complete working cardiac pacemaker in 1958, multiple novel IMDs have been proposed and are currently employed, for different and various applications [15]. These devices can be found in many different body areas, depending on their functionality. A (non exhaustive) list of applications is presented below. For each application an overview of the classical way to power the implant is indicated.

#### Cardiac Implants

Cardiac implants are by far the most known IMD application, they can be used for example to treat bradycardia, tachycardia or heart arrhythmia diseases [16]. Hundreds of thousands people in the world have increased drastically their life expectancy and improved their life quality thanks to these devices. Their are classically made up of two parts: (i) the electrodes placed on the heart wall, actually stimulating the heartbeat, and (ii) the pulse generator, packaged with the battery. The latter is conventionally implanted subcutaneously in the chest, because the overall package is too big to be implanted on the electrode location. It also allows easy battery replacement. The two parts are connected by means of leads. The presence of leads can bring patient discomfort, presenting infections [17], or electromagnetic interference [18, 19]. In fact, when the implanted device is exposed to high magnetic fields, a current is induced on the leads, provoking heating and/or device reset. Recently, leadless, small pacemakers have been proposed, having the battery, with a declared lifetime of about 12 years, embedded in the stimulating system [20]. Heart surgery is needed when the device end of life occurs, and the common practice consists in leave the old pacemaker and implant a new one inside the heart, next to the previous one [21].

#### Brain implants

Another widely stimulated organ is the brain, i.e. Deep Brain Stimulation [22]. It is successfully used to treat many different disorders, such as Parkinson's, depression, epilepsy... This IMDs have a similar structure to cardiac implants: an implanted package containing the pulse generator and the battery, the electrode(s) and the leads. The electrodes are implanted via brain surgery and are connected to the generator (placed normally below the clavicle) by means of the leads. Therefore, patients wearing this kind of device are subject to issues similar to those of cardiac implants. Moreover, in this case, the electrodes dimensions are critically triggering side effects with relation to brain tissue displacement.

#### Vagus nerve stimulators

The stimulation of the vagus nerve, the longest nerve present in the body, is another type of neurostimulation used for instance to treat epilepsy or treatment-resistant depression [23]. As for cardiac and brain implants, also in this case an implanted package, containing the battery and the generator, is implanted subcutaneously, often in the upper left part of the chest. The pulse generator and the

actual electrodes, placed in contact with the cervical vagus nerve, are connected by means of flexible leads. Therefore, also in this case the presence of leads can cause problems to the patients. On the other hand, the limited depth of the cervical vagus nerve, of about 1 cm underneath the skin, make this technology a good candidate to be wirelessly powered from the outside of the body, using powering approaches presented in the next section.

### Cochlear implants

Cochlear implants are used to treat severe hearing loss [24]. They consist of two main parts, one implanted subcutaneously and one placed outside the head. These two parts are generally attached by means of a permanent magnet. The external part has a microphone and a sound processor and a transmitter. The environmental sounds are collected by the microphone, then processed and selected and transmitted by wireless Radio Frequency (RF) link to the receiver, implanted directly behind the skin. The receiver transforms this information to drive an electrode array, placed inside the cochlea, that stimulates the auditory nerve. In this case the implant is batteryless, wirelessly powered by an inductive link. This technique is explained in the next section. The device miniaturization plays a key role, since the big implant dimension (in the order of square centimeters) need invasive surgery to be placed *in-situ*.

### Other applications

Beside the most common applications already presented, other interesting application have been proposed, and they are here briefly presented. Retinal prosthesis are used to eletrically reactivate the retina in case of retinal degenerative deseases [25]. They have a similar structure to cochlear implants, but they stimulate the vision nerve. In this case, the implant powering is carried out by an external battery, connected to the device by a percutaneous cable [26], or, as for cochlear implants, by inductive coupling [27].

Gastric electrical stimulators are another type of neurostimulator IMD, used to threat patients with gastroparesis [28]. Also in this case commercial devices are battery-powered, so the IMD needs to be replaced at the end of its life [29]. Similar stimulation can be used for bladder dysfunctions [30].

In case of diabetic people, implantable insulin pumps can be used to deliver, on the contrary to external pumps, the insulin directly to the liver, better mimicking the natural function of this organ [31]. Commonly, batteries are used to power this kind of IMDs.

Wireless capsule endoscopy is a possible alternative to more invasive fibre-optical endoscopy [32], demanding miniaturized batteries [33]. The same problem is faced by new drug delivery devices [34].

IMDs are used in various other applications, and are expected to cover even more areas in the future. As presented in this section, device miniaturization and implant powering are one of the most challenging aspects of IMD design, limiting their use. An overview of the methods to powering the IMDs is presented in the next section.

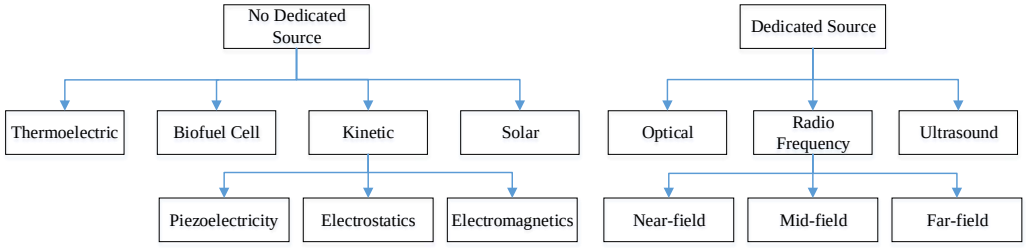


**Figure 1.1** – IMD powering approaches.

### 1.1.2 The powering challenge: batteryless implantable devices

The key feature to further improve IMD technology is the miniaturization [7], in order to allow the placement of the implant near the desired spot of the body with minimum biological tissue displacement. This aims to avoid any damage, any alteration of the normal biological functions and also without decreasing the life quality of patients. As already mentioned, the presence of the battery limits this process, since current technology uses batteries having dimensions of few cubic centimeter in order to provide the energy amount needed over years [35], slowing down the path towards miniaturized biodevices.

A possible solution to avoid the mandatory battery feature in IMDs is to harvest the power from the environment [8, 35, 36, 37, 38]. Fig. 1.1 shows possible approaches to power IMDs, alternative to batteries. These methods can be divided in two main families: the technologies that require an external dedicated source and the ones that do not, harvesting energy from sources already available in the surrounding space.

#### Autonomous powering approaches

Autonomous systems are independent from an external source, harvesting the energy from the ambient environment in many different ways [37, 36]. They use sources available inside the human body, like heat, motion, glucose and oxygen, and solar energy passing though the skin. Therefore, this kind of systems may be a very good alternative to batteries, to design completely independent and batteryless IMDs. On the other hand, they have many limitations: mainly the miniaturization and the amount of energy that can be generated from the low surrounding energy density. But they can be a suitable solution to power ultra-low power implants. In fact, the constant reduction of demanded power by IMDs, towards few tens of microwatts, thanks to technological advancements, is making these power harvesting techniques more and more attractive [39, 40].

**Thermoelectric power harvesting** This kind of devices, normally made in solid-state technology, use strong temperature gradients to generate power, thanks to the Seebeck effect [8, 41]. This technology is a suitable candidate to power

IMDs, since the body is a natural heat generator. On the other hand, it is difficult to find temperature differences inside the body, except for the gradient between skin and inner temperatures. Therefore it is difficult to develop this technology for deep implants. Finally, since thermoelectric generators generate DC power with low efficiency, their surface has to cover typically centimeter scale, being an issue for miniaturization, critically required for such organ as brain.

**Kinetic power harvesting** Since the body is in continuous motion, e.g. breathing, heartbeat, muscle and blood vessel contractions, it has been proposed to harvest this energy by of means different devices [42]. Piezoelectric materials can transform mechanical deformation in electric potential [43, 44], electrostatic transducers convert the motion by using variable capacitors [45] and electromagnetic devices take advantage of the Faraday-Neumann-Lenz law, using a coil and a permanent magnet [46]. Limited to relative motion, they have to be precisely attached on the desired spot. Moreover, the miniaturization is not simple (especially for electromagnetic devices), they can be very costly and have biocompatibility issues (piezoelectrics). Finally, they may present a high output impedance, limiting the output current, and they usually need a voltage source to be initially polarized (electrostatic).

**Solar power harvesting** This kind of devices harvests the solar power from the light that penetrates inside the human skin, especially in the infrared spectrum [47, 48] and they have been also completely integrated in a single chip [49]. Solar devices are limited to subcutaneous application, since the light does not penetrate deep in the body. Finally, as light is being attenuated through the skin, available power and conversion efficiency tend to be low, thus limiting the miniaturization.

**Biofuel cells** Biofuel cells (BFCs) transform biochemical fuels into electricity, thanks to chemical reactions [50]. In particular enzymatic glucose BFCs harvest energy directly from living organisms, using often specially designed enzymes [51]. This kind of cells use two electrodes, the surface of which is modified by placing the enzymes, to perform the electrochemical reaction. They take advantage of the oxidation of the glucose and the reduction of molecular oxygen to water in order to produce electrons, as follows:

$$\begin{aligned} \textit{Anode side} &: \mathrm{C_6H_{12}O_6} \longrightarrow \mathrm{C_6H_{10}O_6} + 2\,\mathrm{H^+} + 2\,\mathrm{e^-} \\ \textit{Cathode side} &: \mathrm{O_2} + 4\,\mathrm{H^+} + 4\,\mathrm{e^-} \longrightarrow 2\,\mathrm{H_2O}. \end{aligned}$$

At the anode side, the glucose ($C_6H_{12}O_6$) is electrooxidized, producing gluconolactone ($C_6H_{10}O_6$), two hydrogen ions and two electrons. These electrons flow towards the cathode side, where they combine with oxygen and hydrogen ions to produce water by a reduction process. The produced electron flow, passing trough a load, generates the energy needed to power the IMD: Fig. 1.2 shows the operating principle of a glucose biofuel cell. At the anode side, the most commonly used enzyme is the Glucose Oxidase (GOx), while different ones are used at the cathode side. From them, the Bilirubin Oxydase (BOD) is a popular one [52]. In order to optimize the electron transfer, special designed polymers, that help the electron

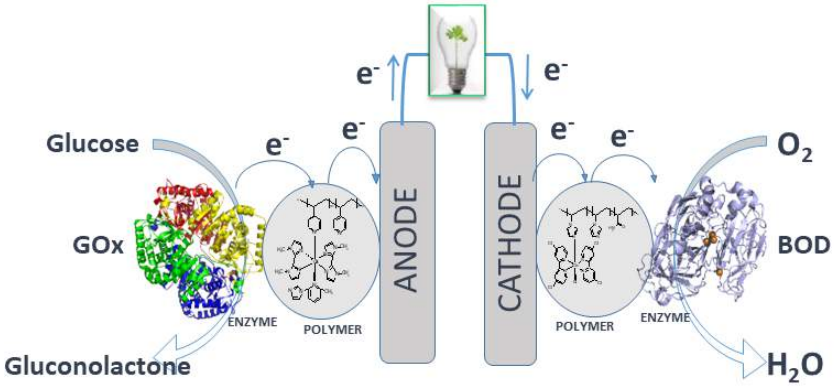


**Figure 1.2** – Working principle of a glucose BFC.

passage from the enzymes to the electrodes, are added to the enzymes, as Fig. 1.2 shows.

Since glucose and water are widely present in biological environment, e.g. in the human body, the IMDs could be powered by the body's own resources, in a completely renewable way. Therefore, no movement or external sources are required. Moreover, the glucose biofuel cells have evidenced a glucose concentration dependence of the power output [52], allowing the direct monitoring of the glucose concentration in the organism [53, 54, 55].

This technology has been demonstrated *in-vivo*, in several animals [56]. Recently, biofuel cells have been used to power electronic devices, in particular wireless sensors [57, 58, 59].

BFCs can be a suitable solution to power autonomous IMDs, and they have flexible design, since the electrodes can be shaped following the designer's needs. For some time, one of the main limitation of BFCs were the poor energy density that can be achieved. However, studies have demonstrated that design optimization of the electrodes, e.g. by using highly ordered macroporus ones [60], increase the electrode effective surface, thus boosting the power density of these structures towards hundreds of microwatts per square centimetre of active surface [61, 62]. On the other hand, the limited lifetime of these devices and possible long-term biocompatibility issues are the main challenges that have to be faced to improve BFCs capable to succesfully power an IMD [63].

### Powering approaches demanding a dedicated source

Above-mentioned autonomous systems can be an elegant and comfortable way to power IMDs, not demanding an external source. However, they can generally provide low power, thus high-energy demanding devices (from hundreds of µW to tens of mW) cannot be sustainably powered. Moreover, each technology has the limits presented in the last sections. Finally, no communication unit is embedded in these devices. Therefore engineering efforts have to be made if it is needed to retrieve the data from the outside of the body, increasing the dimension of the IMDs to include the communication unit, e.g. the antenna.

To overcome these restrictions, systems that receive the power from a dedicated

source can be implemented, developing a Wireless Power Transfer (WPT) link [35, 8, 38, 64]. They can produce enough power for IMDs and the wireless power link between the inside and the outside of the body can be also exploited to perform communication with the implants, allowing the development of self-powered wireless communicating IMDs. On the counterpart, the straightforward limitation of these systems is the constant need of an external source, that has to be coupled to the implant. Moreover, many challenges have to be faced in order to deliver sufficient power to a tiny implant placed deep inside the body. To quantify the quality of the designed link, the main Figure of Merit (FoM) to characterize these links is the Power Transfer Efficiency (PTE), defined as the ratio of power delivered to the implant load with respect to the power transmitted by the source:

$$PTE = \frac{P_r}{P_t}, \tag{1.1}$$

where $P_r$ and $P_t$ are the received and transmitted power respectively.

**Optical wireless power transfer** Following the solar power harvesting, implanted photodiodes can be used also to generate energy from an optical source, e.g. a laser, placed close to the human body [65, 66]. This technology can be successfully used in subcutaneous implants, taking also advantage of the high achievable data-rate for communication and the possible miniaturization towards sub-mm scales [65]. On the other hand, the skin dramatically attenuates the light, resulting in a maximum penetration depth between 5 and 10 mm [67]. Therefore, as mentioned previously, this technique cannot be used for deep IMDs. Finally, the emitting source can heat the skin, limiting the emitter power levels.

**Ultrasonic wireless power transfer** Similarly to optical power beaming, energy can also be transmitted using acoustic waves. In this case, an implanted piezoelectric material retrieves the mechanical wave, often in the ultrasonic frequency range (>20 kHz), generated by a dedicated source placed on the skin [68, 69]. In the last years this technique has attracted increasing attention to the research community, thanks to the advancement on material research.

Acoustic waves present low attenuations inside the tissues, allowing the focusing of the transmitted beam on a mm-scale implant placed several centimetres inside the body. Moreover, the mechanical waves do not interact with Electromagnetic (EM) waves, so no EM interference is created. Finally, the regulations on exposition to ultrasonic waves allow an higher transmitted power with respect to EM fields. For these reasons ultrasonic WPT is a very good candidate to power mm and sub-mm IMDs, especially if the targeted implant spot is deep (few centimeters) inside the body [70].

On the other hand, acoustic waves are effected by the inhomogeneity of the human body, resulting in possible high reflections at the separation between two different tissues, especially the air-skin or muscle-bone ones. Therefore it is very important to achieve a good acoustic impedance matching and to maximise the matching between the transducer and the tissue [71]. Moreover, ultrasonic waves are almost totally reflected by bones, limiting their applications. Finally, there

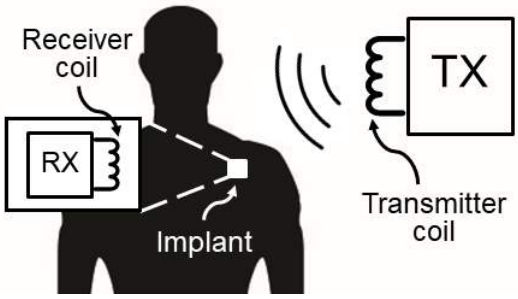


**Figure 1.3** – Typical application of an implanted near-field WPT system.

could be unknown effects of long-term exposure to ultrasonics that have to be monitored [72].

**Radio frequency wireless power transfer** It is well known, from the first Tesla experiments that WPT through EM waves is a suitable method to deliver power wirelessly [73]. In the last decades, myriads of designs have been proposed using this method, leading to Food and Drug Administration (FDA) (in US) and European Medicines Agency (EMA) (in Europe) approved commercially available IMDs, e.g. cochlear implants and retinal prosthesis, as presented earlier in this sections. The RF-WPT can be divided in near-field [74], mid-field [75] and far-field [76] EM coupling, depending on the region of the EM field, generated by the Transmitter (TX), where the Receiver (RX) is placed. In particular, far-field coupling takes advantage of radiative fields, near-field coupling non-radiative one and mid-field WPT places itself between the two.

Near-field coupling is made by inductive coupling, based on the Faraday's law of induction, exploiting the mutual induction between two (or more) coils, one placed inside the body and one outside it [77]. Fig. 1.3 shows the typical near-field WPT scheme: a device, having a coil, is implanted and it is magnetically coupled to a transmitter placed close to the subject's skin. This technique is particularly suitable to power IMDs thanks to the nonmagnetic proprieties of the human tissues [78] (as presented in the next section), leading to a myriad of proposed solution in literature [74]. Morover, inductive coupling WPT is also suitable for communication, achieving data rates in the order of several Mb/s [79]. The main limitation of this technology is the poor distance that can be achieved, but this distance can be increased by making the two coils resonate at the same frequency, developing a Magnetically Coupled Resonant (MCR) WPT scheme [80]. The typical operating frequencies range from low-kHz to hundreds of MHz.

MCR-WPT can achieve very high PTE, higher than ultrasonic coupling, and it is also independent from the tissue characteristics. On the other hand, efficiency drops dramatically when the distance between the two coils increases. In fact, the magnetic field generated on the axis of a circular coil having $N$ turns can be derived by the Biot-Savart's law:

$$H_z = \frac{NI}{2} \frac{r^2}{(z^2 + r^2)^{3/2}}, \tag{1.2}$$

where $I$ is the current carried by the coil, $r$ is the coil radius and $z$ is the distance

between the coil and the observation point. Eq. (1.2) shows that the generated magnetic field, and thus the received power, are strongly dependent by the TX-RX separation. This kind of link is also highly dependent on the coil alignment and when the surface of the implant coil is decreased, i.e. coil miniaturization [70]. Finally, the transmitter power is limited by regulations, to avoid effects of the exposure to RF EM fields [81], limiting thus the received power. The main strategies to design an MCR-WPT will be presented in the next section.

In order to overcome these problems and to achieve more communication distance, mid-field WPT has been developed [75]. Using this technology, the IMDs are less dependent on the alignment with the transmitter and higher distance can be achieved. Moreover, since higher frequencies are used [82], the receiver coil can be further miniaturized. As an example, a miniaturized stimulator IMD (volume $< 12\,\mathrm{mm}^3$) has been used to power *in-vivo* a cardiac pacemaker in a porcine animal, placed more than 4 cm inside the body [83]. In order to overcome tissue absorption of EM waves, especially in the low-GHz frequency range used in mid-field coupling, and to allow the transmitter signal to reach the implant, a specially designed source is needed [83, 84]. On the other hand, the need for this kind of transmitters to produce the required wave propagation inside tissues is also the main limitation of these devices, limiting their design flexibility. Moreover the power delivered is still lower than the achievable power using near-field coupling [64].

Finally, a "classic" far-field link can be also used to power IMDs [76]. Far-field coupling allow miniaturization of the implant, thanks to the high permettivities of body tissues, and does not require alignement between the two antennas, especially when circularly-polarized receivers are used [85]. Also, thanks to higher frequencies used than near-field coupling, higher data rates can be achieved. On the other hand, far-field EM WPT is not free from challenges: the tissue absorption, that also limits the maximum transmitted power, and the poor gain of these antennas limit the implant depth to few millimetres or lead to low PTE, limiting dramatically the harvested power with respect to the other two techniques presented here.

### 1.1.3 Hybrid powering of IMDs

Every approach to power an IMD presents some advantages and disadvantages, that limit the available power to the implants. In order to overcome this problem, some hybrid solutions have been presented in literature, using two (or possibly more) different techniques in one single implant. Moreover, adding different power sources increase the system reliability and resilience, since the harvested sources can vary unpredictably [86].

Regarding systems that use autonomous-only powering approaches, some hybrid power management platforms have been proposed [86, 87, 88, 89]. In [86], a multi-purpose platform has been reported, able to harvest power from solar, thermal and kinetic (piezoelectricity) energies. Unfortunately, the device requires a minimum of 1 mW of power to operate efficiently, which is far higher than the ambient power available in implanted solution (in the order of µW). In [87], a thermoelectric harvester is combined with two different kinetics transducers (electromagnetic+piezoelectricity), while in [88] two kinetics harvesters (electromag-

netic+piezoelectricity) are implemented. These solutions have been designed for wearable application and are too bulky to be implanted. Finally, in [89] a hybrid energy harvester interface is proposed, using thermoelectric energy and an implanted BFC. This system can switch between dual or single-source modes but this switch cannot be controlled remotely, since it does not have a communication feature. This device is the only one especially designed for implants purposes, therefore it is compact and optimized for the amount of energies typically available, but the superposition of the two harvesters leads to more volume, hence more tissue displacement, which is a drawback.

Also in the case of IMDs using power harvesting techniques needing a source the design of hybrid solutions can bring benefits. In fact, the use of more than one powering approach can overcome the limitations that a single technology presents, in order to achieve high PTE on implants placed deep inside the body [90, 91]. Some hybrid devices have been proposed also to separate the WPT and the communication links [92, 93, 94], but in this case it is not fair to speak about hybrid powered devices. For example, in [92] a first proposition of an inductively powered devices, communicating with an optical link, is proposed. It can achieve high data rates (of the order of 10 to 100 Mbit/sec) while taking advantage of the high efficiency of the near-field WPT to transmit high power. In [93], an implant is powered by an ultrasound link having a carrier frequency of 1 MHz, in order to allow the powering of small implants placed 3 cm deep inside the body. The carrier provides also the downlink path for communication, having a data rate in the order of kbps. The up-link is implemented with a far-field RF transmission, at 4 GHz, to achieve high data rates ($\tilde{\text{M}}$bps), for recovering *in-vivo* images. In fact, although the high power transmission losses of a far-field link are unacceptable for WPT, they can be overcomed by the high sensitivity of the external data receiver towards high signal-to-noise and data rate communication. Similarly, in [94], in continuity with the last design, the communication is made by a far-field link, while the powering is achieved by a 13.56 MHz inductive link. Three different prototypes are proposed, working at three different communication frequencies (415, 905 and 1300 MHz).

True hybrid power systems are found in [90] and [91] where a hybrid near-field RF and ultrasonic WPT link is proposed. The efficient inductive coupling is used to cross the air/skin barrier, that presents a high acoustic discontinuity, while the ultrasonic link is used to power an implant placed deep inside the body, e.g. 7 cm in [90]. In [90] the inductive harvested signal is amplified to drive the acoustic link, adding considerably complexity, size and power loss to the IMD. In [91] the two WPT links, RF and acoustic, are optimally placed in cascade without any amplifier. This device allows to power a device, having a diameter of 1.1 mm, at a distance of 6 cm (3 cm in air and 3 cm inside the tissue). The achieved total PTE is 0.16%, remarkable if compared to the state-of-the-art mid-field proposed link having an efficiency of 0.04% (receiver diameter: 2 mm, distance: 5 cm) [95] and 0.056% (receiver diameter: $\tilde{2}$ mm, distance: 4.2 cm) [83].

Although the proposed hybrid devices ensure higher power to the IMDs than the single-approach ones, they are still limited. Autonomous hybrid systems [86, 87, 88, 89] do not allow the harvesting of high power levels, due to the limitations of each technology and no communication with the external of the body is provided. WPT schemes [90, 91] require the constant presence of a source to provide the amount

of power needed. Moreover, the presence of the two transducers add volume and complexity to the systems and surgery.

In order to avoid the constant presence of the source, a hybrid powered IMD, using one (or more) autonomous harvesting technology and a WPT solution can be designed. In [96] the near-field RF WPT (13.56 MHz) and thermoelectric power harvesting is used to charge a microbattery, but it is not capable to extract energy simultaneously by the two sources. In [97] the power is harvested using solar, kinetic (piezoelectric) and far-field RF WPT (designed to harvest ambient RF signals). In this case, high efficiency is achieved, at the cost of a large implantable volume. As a conclusion, to the author knowledge, no hybrid solution to power IMDs, including at least one independent power harvesting approach and a WPT scheme has been proposed in literature. In chapter 3 a possible hybrid IMD is proposed, harvesting the power with a BFC and a near-field WPT link.

## 1.2 Design strategies for a near-field WPT link to power an IMD

As presented in the last section, the most important FoM to be taken into account while designing a WPT link is the PTE. In case of a near-field MCR-WPT, this parameter is defined as [98] (without taking into account the load circuit):

$$PTE = \frac{P_r}{P_t} = \frac{k_{12}^2 Q_1 Q_2}{1 + k_{12}^2 Q_1 Q_2}, \tag{1.3}$$

where $P_t$ and $P_r$ are respectively the power transmitted and received, $k_{12}$ is the coupling factor between the two coils, $Q_1$ and $Q_2$ are the quality factors of the TX and RX, respectively. Eq. (1.3) shows that the PTE is a function of the frequency, the geometrical characteristics of the coils and the medium where the coils are placed. In IMDs, the implant coil needs to be small compared to the wavelength, thus high quality and coupling factors are difficult to be achieved. Moreover, the presence of the body tissues further decrease the TX and RX quality factors, as shown in the next section.

### 1.2.1 Dielectric properties of body tissues

The body tissues, unlike the free-space, present high dielectric permittivity. Moreover, they are lossy and frequency dependent [78]. Therefore, the tissue permittivity is a complex number and it can be defined as:

$$\epsilon_{tissue} = \epsilon_0(\epsilon_r' - j\epsilon_r''), \tag{1.4}$$

where $\epsilon_0$ is the vacuum permittivity, $\epsilon'$ and $\epsilon''$ are the real and imaginary part of the complex permittivity. The real part describes the dispersion phenomena and the imaginary part the tissue absorption (or losses). The losses can be evaluated also taking into account the conductibility, defined as:

$$\sigma_{tissue} = \omega\epsilon_0\epsilon'', \tag{1.5}$$

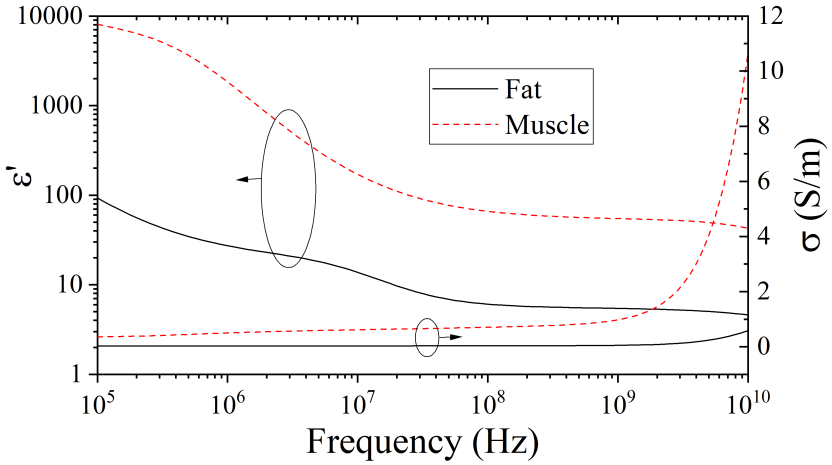


**Figure 1.4** – The dielectric permittivity and conductivity of fat and muscle tissue. Source: [99].

with S/m unit, and where $\omega$ is the angular frequency (rad/s). These characteristics change in different tissues and they are mainly dependent on the tissue water concentration. In fact, higher water concentrations result in higher permettivity and losses. For instance, Fig. 1.4 shows the $\epsilon'$ and $\sigma$ for fat and muslcle tissues as a function of frequency. The muscle presents higher permittivity and losses, due to the higher water concentration. Since the IMDs are often implanted in muscle, the high losses have to be taken into account: they lower the receiver quality factor, limiting the PTE shown in Eq. (1.3). Moreover, the presence of tissue losses limits the power that can be emitted by the TX, in order to insure safe operation of IMD, because the losses lead to tissue heating, which impact the biological cells [81, 100].

On the other hand, the tissues are non-magnetic, therefore the magnetic permeability can be defined as:

$$\mu_{tissue} = \mu_0(\mu_r' - j\mu_r'') = \mu_0, \tag{1.6}$$

where $\mu_0$ is the vacuum permeability, $\mu_r'$ and $\mu_r''$ are the real and imaginary part of the permeability, $\mu_r' = 1$ and $\mu_r'' = 0$. Thanks to the non-magnetic properties of tissues, the near-field WPT, that uses magnetic coupling, can be used without tissue coupling, and high PTE can be achieved. Moreover, the tissues transparency to magnetic fields makes this technology insensitive to tissue discontinuities. On the other hand, the dielectric tissue properties explain also the difficulties to achieve high efficiency in far-field coupling, due to the presence of electric field-induced tissue losses.

### 1.2.2 Best frequency and receiver structure

The two main parameters that have to be chosen while designing a WPT link are the receiving coil diameter and the operating frequency. The first one is selected by the designer, taking into account the targeted IMD application. In fact, the coil dimension has ideally to be minimized for every application, in order to minimize the inflammatory response of the body [101]. On the other hand, smaller coils

dramatically reduce the coupling factors, due to the less quantity of transmitted magnetic flux harvested by the RX coil. Therefore, a design tread-off between the two has to be taken into account. Typically, IMD coils dimension range from cm-size, in case of sub-epidermal implants, e.g. cochlear implants, towards mm or even sub-mm size for neural application.

The frequency selection has a key-role in the design of MCR-WPT links, to maximise the PTE and limit the tissue absorption. In fact, higher frequencies allow implant miniaturization and higher quality factors. On the counterpart, the tissue absorption increases with $f^2$, limiting the transmittable power [100].

Traditional cm-sized implants operate in the order of 10 MHz (the 13.56 MHz band is the most commonly used) or below [98, 102, 103, 104, 105, 106, 107, 108, 109]. In fact, as shown in [102], the best frequency for printed spiral coils is at about 10 MHz. Printed spiral coils are mostly used for cm-sized coils, down to 5 mm coils [108], thanks to their easy manufacturing, that can be done also on flexible substrates. When the implant dimension are in the low millimetre range, e.g. 1-2 mm, solenoidal coils are preferred because they can reach higher quality factors and they present more design flexibility [83, 95, 110, 111, 70, 112]. In [82] it has been shown that the best frequency to power mm-sized implants is in the low-GHz range, this frequency lowers towards hundreds of MHz if the TX dimension is in the centimetre range. As presented in Sec. 1.1, a special designed source is needed to overcome the high tissues losses at these frequencies (Fig. 1.4) that limits the field penetration and the allowed transmitted power. A mm-sized WPT (1 mm diameter) link using a traditional printed coil as TX is presented in [110]. In this case the optimal design frequency was 200 MHz. A figure of merit that takes into account the tissue absorption is defined in [111]. In this case an optimal frequency of 20 MHz was found to deliver the maximum amount of power to the implant within the safety limitations. In this case the operating frequency was lowered to overcome the tissue absorption increase with the frequency.

All of these proposed designs optimize at the same time the transmitter and the receiver, since the PTE is dependent on both. In [112], the PTE formula was divided in two FoMs, in order to allow the separate design of the TX and RX. In this case two different 1 mm coils are optimized with resulting best frequencies of 500 and 700 MHz. This particular technique, presented in Sec. 1.2.4, is used also in the present work, as presented in chapter 4.

In general, two different cases can be faced when designing a MCR-WPT link to power IMDs. In the case when the operating frequency is defined by design constraint, the geometries of the two coils need to be optimized, to insure the maximum quality and coupling factors. When the frequency is not a constraint, the receiver coil can be optimized respecting the geometry constraints, e.g. diameter and/or maximum occupied volume, and the operating frequency is chosen in order to maximize the receiver Q factor [64]. This because the transmitter coil has less constraints, and can be optimized at the chosen frequency in order to insure the maximum delivered magnetic field at the receiver position, respecting the safety limits. To design the structures presented in this work, this second approach was used.

### 1.2.3 Strategies to limit the effect of body tissues at the receiver side

As already mentioned, to correctly design an implantable MCR-WPT link, the PTE, defined in Eq. (1.3), has to be maximized. Therefore the main challenge is to maximize the parameter:

$$\Pi = k_{12}\sqrt{Q_1 Q_2}. \tag{1.7}$$

The coupling factor $k_{12}$ is only dependent on the two coil geometries, but it does not depend on the media where the coils are placed, since in tissues $\mu_r = 1$. On the contrary, the quality factor depends on the surrounding medium. In fact, it can be defined as [113]:

$$Q = \omega \frac{W_{net}}{P_L + P_\epsilon + P_{rad}}, \tag{1.8}$$

where $W_{net}$ is the net energy stored by the coil, $P_L$ are the conductor losses, including ohmic losses, skin and proximity effects, $P_\epsilon$ is the time-average power lost due to dielectric losses and $P_{rad}$ is for the radiation losses.

Therefore, when the receiver is placed inside the tissue, the dielectric losses (absent in the free space case) appear and lower the overall quality factor. In order to limit this Q factor decrease, often a biocompatible low-lossy material is added to encapsulate the receiver. This material, often PDMS, ensures also the biocompatibility of the implanted structure. However, this coating increases the overall volume of the implant and its presence needs to be taken into account. Despite the importance of the encapsulation, its presence is rarely taken into account in research papers, and just a published one, to the author knowledge, studies the optimal coating dimension [103].

In the case of printed spiral coil, a superstrate and a substrate (only in case no substrate is included) are added to the design [103, 108]. In [108], the reported receiver quality factor is 24 in air, while only 11 inside muscle tissue. After the coating, the Q factor increase to 17, but the coating thickness and/or the external dimension are not reported. The silicone superstrate is considered in [103], where an optimum tickness of 300 µm was found in muscle environment, but no trade-off between coating thickness and performance improvement was studied.

Taking into account solenoidal mm-sized coil, the use of coating is often reported but not optimized. In mid-field structures, the encapsulation with PDMS is reported, but its optimization is not carried out [83, 75]. In [75] the implant volume is reported without taking into account the coating, while it is reported to be 12 $mm^3$ in [83]. An arbitrarily chosen coating thickness of 100 µm is reported in [111] for simulation, but no encapsulation is present in measurements. Two different coating thickness, not optimized, having values 100 µm and 500 µm are reported during the design of the coil proposed in [112], reporting an expected improving of the Q factor with the coating thickness increase. But no optimization has been carried out, the encapsulation thickness was not controlled during the fabrication of the measured device, and it was way higher than the simulated thickness (the final coating thickness value is not reported). Finally, the presence of PDMS was not taken into account in the implant total volume.

In chapter 4 an extensive analysis of the encapsulation presence is carried out,

and a structure that insures at the same time good Q factor and the contact between the implanted coil and body tissues is presented.

### 1.2.4 Separation of the TX and RX coil design

Eq. 1.3 shows that the design of the TX and RX coil has to be carried out simultaneously, since the coupling factor $k$ depends on both. On the other hand, the implant volume constraints and the presence of body lossy tissues make the design of the receiver side more challenging. Therefore, it could be useful to separate the developing of the two sides of the WPT link. As introduced earlier in this chapter, in [112] two FoMs are proposed for this purpose, and used in this work (Chap. 4). For the sake of completeness, the definition process of these FoMs are here reported.

Since the small size of RX coils and the high TX-RX separation distance (generally higher than the RX diameter in mm-sized coils) result in small coupling factors, it can be assumed that $k_{12}^2 Q_1 Q_2 \ll 1$ and Eq. 1.3 can be approximated:

$$PTE \approx k_{12}^2 Q_1 Q_2, \tag{1.9}$$

where $Q_1$ and $Q_2$ are the TX and RX coil quality factor respectively. Moreover, the coupling factor can be expressed as:

$$k_{12} = \frac{M}{\sqrt{L_1 L_2}} = \frac{\mu_{eff} H_0 S_{RX}}{\sqrt{L_1 L_2}}, \tag{1.10}$$

where $M$ is the mutual inductance between the two coils, $L_1$ and $L_2$ are the TX and RX self inductances. $S_{RX}$ is the effective receiver area where the magnetic flux is calculated, $\mu_{eff}$ is the magnetic permeability of the area surrounding the implant coil, $H_0$ is the magnetic field, normal to the RX coil, generated at the implant position by the TX coil, driven by 1 A of current. By inserting Eq. 1.10 in Eq. 1.9 and taking into account that in body tissues $\mu_{eff} = \mu_0$ the PTE can be written as:

$$PTE \approx \frac{(\mu_{eff} H_0 S_{rx})^2}{L_1 L_2} Q_1 Q_2. \tag{1.11}$$

Thanks to the small size of the implant coil with respect to the TX one, it can be assumed that the magnetic field generated by the transmitter is homogeneous at the RX coil. Therefore, the TX and RX dependence inside Eq. 1.11 can be separated, by defining two FoMs:

$$PTE \approx F_{TX} \cdot F_{RX}, \tag{1.12}$$

where:

$$F_{TX} = \frac{H_0^2}{L_1} Q_1 \quad , \quad F_{RX} = \frac{(\mu_0 S_{RX})^2}{L_2} Q_2. \tag{1.13}$$

Acting like this, the design of the MCR-WPT is simplified and the two coils can be separately optimized: the TX coil has to deliver the highest possible magnetic field at the implant position within the exposition regulations [81], and the RX side has to harvest the maximum portion of the generated field.

## 1.3 Wearable medical devices

When the presence of an IMD is not required, Wearable Medical Devices (WMDs) can be a very good, less-intrusive, alternative to allow real-time easy monitoring of the patient [5, 114]. The presence of these devices is now spreading thanks also to the diffusion of smartphones, embedding healthcare monitor capabilities [115]. Including smartphones, great attention has been paid to the development of wireless WMDs, allowing the remote health monitoring [116]. Since WMDs have less design constraints respect to IMDs, the miniaturization can be less aggressive, allowing the use of a battery. On the other hand, high capacity batteries, that allow long lifetime, are still bulky, augmenting the device weight and the discomfort to users [117]. The minimization of the patient discomfort is very important in order to allow easy acceptation of the device by the final user. In order to avoid the presence of batteries, the same powering approaches shown in Fig. 1.1 and presented in the last section can be implemented [118]. In addition, these techniques are easier to implement, thanks to the fact that less constraints are present, e.g. less light absorption by the skin, higher available surface and volume, and the absence of complete biocompatibility requirement. A myriad of batteryless WMDs have been proposed in literature, and their analysis goes beyond the purposes of this work. Therefore, this section focuses on a subset of batteryless WMDs: the Ultra High Frequency (UHF) Radio Frequency Identification (RFID) wearable sensors.

### 1.3.1 Wearable passive UHF-RFID sensors

Inside the batteryless wireless WMD family, completely passive systems are gaining high attention in WBANs, thanks to their flexibility and the absence of batteries. Inside this family of devices, UHF-RFID sensors are an interesting choice, since they can work without a battery and can be developed in flexible substrates in order to improve their wearability [119]. Moreover, the technology advancements on RFID Integrated Circuits (ICs) (e.g. improvement of chip sensitivities [120]), are making this technology more and more attractive. Classical UHF-RFID tags allow the simultaneous identification of people (or objects) at a distance up to 10 m, without requiring line-of-sight, and thus they are widely used in several applications, like supply chain management and personal identification [121]. Beside this capability, in recent years growing interest has been dedicated to the development of RFID tags with sensing capabilities, added to the identification purposes [122]. As a natural consequence, this technology it is also suitable for batteryless WBAN applications [123].

Fig. 1.5 shows the typical scenario for an UHF-RFID sensor network. An RFID reader sends a modulated carrier having a frequency within the UHF band (860-960 MHz), that powers and interrogates the RFID tags. This carrier is re-modulated by the sensor tags, including information such the tag ID and the data collected by the sensors, and sent back, via backscattering, to the reader. The reader then collects and, eventually, processes the data.

The UHF-RFID sensor tags can be divided in two main and distinct branches. The first exploits the change of the EM characteristics of the tags, e.g. reso-

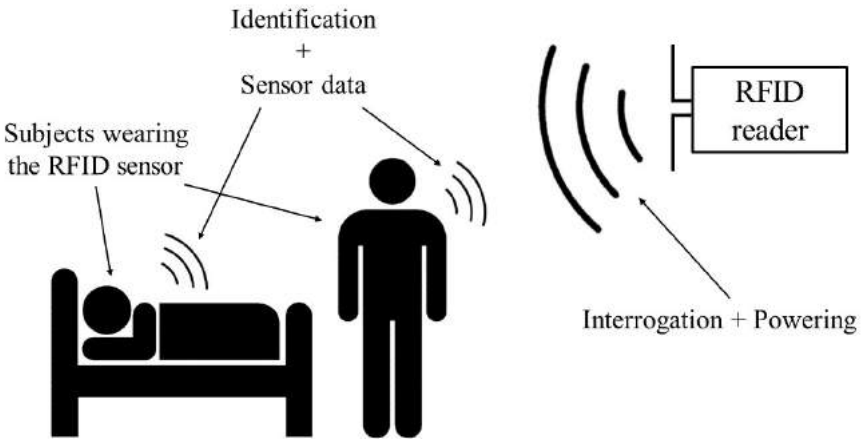


**Figure 1.5** – Functional principle of an UHF-RFID sensor network.

nance frequency and/or backscattered power shifts, to retrieve the information. In this case no data are collected by the tags, simplifying the wearable sensor design to a classical identification-only tag. On the other hand, additional coding and/or external circuitry are demanded on the reader side, increasing its complexity. Examples of this category are real-time activity recognition [124], particularly useful for elderly people monitoring, movement detection [125] and breath monitoring [126]. Moreover, an RFID solution has been proposed to restore lost senses on fingers [127]. Other sensors that are part of this category, take advantages of their shape or surrounding environment modifications, that change their EM characteristics, to encode the information. For instance, strain sensors on textile antennas use the antenna stretching [128, 129] and moisture sensors take advantage of the environmental dielectric change [130, 131]. These sensor tags are quite easy to be implemented but they are limited by the fact that it is difficult to isolate the modifications of the EM characteristics to the monitored magnitude. This because the tag response is also influenced by environmental changes, e.g. increased path losses, interferences, etc.

The second branch of batteryless UHF-RFID sensors uses special designed RFID chips, often including an Analog-to-Digital converter (ADC), having embedded sensor capabilities or external sensor interfaces, that allow the data processing directly in the RFID tag [132]. Therefore, in this case the tag design is more challenging, in order to embed the sensors. On the other hand, this technology allows incredible flexibility to the tags and countless applications, having the sensed data independent from the path. The only constrain is that the sensor tag has to be within the reading range of the reader. On the counterpart, the sensitivity of these chips (i.e. the minimum received power needed to turn-on the IC), one of the key parameter of RFID ICs as shown in the next section, is generally lower than the one of ICs used for the devices described previously. This because a portion of the harvested energy is needed to control the internal and/or external sensors.

The most common application for this type of sensors is the body temperature monitor [132, 133, 134], since RFID ICs with embedded temperature sensor are commercially available [135, 136]. Vital signs monitoring systems have also been proposed, like ECG [137] or EEG [138] monitoring systems. Moreover, a smart

sock, capable to detect abnormal relative plantar pressure is presented in [139]. An accelerometer integrated batteryless RFID sensor is used in [140] to track in real-time bed-regress in elderly people. More recently, a general purpose high-wearable RFID data-logger [141], a graphene oxide-based wearable sensor for breath monitoring [142], and a pH sensor for human skin [143] were proposed by the same research group.

As just shown, this kind of batteryless sensor tags are a very interesting solution for real-time body monitoring. Two different applications are presented in this work. A passive sensor tag for implanted BFC monitoring in laboratory rodent and an ultra-low-cost body temperature monitoring device are presented in Chapters 2 and 5 respectively.

### 1.3.2 Key parameters for the wearable UHF-RFID sensors design

As explained in the previous section, the key parameter to take into account when designing an UHF-RFID tag is the Reading Range (RR), in order to maximise the readability of the tag, and thus to increase the comfort for the patients, the number of detectable tags at the same time and the covered area. The RR is given by [144]:

$$RR = \frac{\lambda_0}{4\pi}\sqrt{\frac{EIRP \cdot G_r \cdot \tau}{p_{min}}}, \tag{1.14}$$

where $G_r$ is the gain of the receiver tag antenna, $\tau = 1 - |S_{11}|^2$ is the tag power transmission coefficient, $p_{min}$ is the sensitivity of the RFID chip and $EIRP$ is the equivalent isotropic radiated power, defined as:

$$EIRP(dBm) = P_t(dBm) + G_t(dB) - L_c(dB) + \alpha_{plf}(dB), \tag{1.15}$$

where $P_t$ is the power transmitted by the reader, $G_t$ is the reader antenna gain, $L_c$ are the cable losses and $\alpha_{plf}$ is the polarization efficiency. Since the reader antenna is commonly circularly-polarized, this last term can be often neglected. Since most of the terms in (1.14) depends on the reader side, and $p_{min}$ is an intrinsic characteristic of the selected RFID IC, the tag optimization consists in the maximization of the following:

$$Realized\ gain = G_r\,\tau. \tag{1.16}$$

Therefore, the designer challenges that have to be faced, under the design constraints, are: the matching between the antenna and the IC, to maximize the transmission coefficient, and the tag antenna gain. Moreover, in particular applications, design constraints on the antenna radiation pattern might be added.

When designing a wearable tag, in continuity with the implant design, the presence of the body has to be taken into account. In fact, the high permittivities and losses of body tissues, as seen in Sec. 1.1, change the EM antenna characteristics, and both the gain and $\tau$ are effected [145]. The trade-off that has to be faced by designers is between the RFID tag performances, defined by Eq. (1.16), and the wearability of the device. In fact, for instance, bigger tag footprint enhances

the antenna gain, but it results also in a less comfort to the person wearing the device. Thin, flexible tags, often directly attached to the skin, insure the higher possible wearability, at the cost of poor reading ranges [146]. Bulky devices, in contrast, presents higher EM performances, but they could introduce patient discomfort [134].

In the next Chapter, all these aspects will be taken into account in order to propose several wearable batteryless UHF-RFID tags.

## 1.4 Research context

This PhD thesis was developed in the MDA team (*Microsystèmes de Détection à ondes Acoustiques et alternatives*, Acoustic wave based and other innovative Detection Microsystems) of the *Ondes* (Waves) group in the framework of the IMS (*Laboratoire de l'Intégration du Matériau au Système*, Integration: from Material to Systems) in Talence, France. The team research focuses on the propagation of waves in resonant devices and dynamical interaction mechanisms with an adjacent solid, liquid or gaseous medium, e.g. the body tissues, targeting the realization of sensitive and reliable microsensors.

In the framework of the MDA team, the micro-energy platform research program aims to develop novel miniaturized smart implantable sensors/actuators using novel powering and communication approach. Beside this PhD work, different researches are being carried out. The main topic are: the study of a novel hybrid RF/ultrasonic IMD, the proposition of innovative RF transmitters to wireless powering IMDs and the design of miniaturized electronic RF circuits, in particular oscillators, that will be used to implement the smart devices.

Moreover, given the high multidisciplinary nature of this research project, many external laboratories have helped and collaborated during this three years work. In the next sections the research structures that have been involved, specifying their role, are listed, as well as the research projects linked to this dissertation.

### 1.4.1 Research partners

Laboratory/Team: **NSysA group, Institute of Molecular Sciences (ISM) of the University of Bordeaux**
Role: Development and fabrication of the macroporus electrodes used to build the BFCs.

Laboratory/Team: **Biotechnology and Bioengineering group, Centre de Recherche Paul Pascal CRPP**
Role: Development of whole set of Biofuel cells used during this thesis.

Laboratory/Team: **Laboratory for the Bioengineering of Tissues (BioTis), French National Institute of Health and Medical Research (INSERM) and the Université de Bordeaux**
Role: All the *in-situ* and *in-vivo* experiments on laboratory rodent, including the BFC implantations, were carried out in collaboration with this laboratory.

Laboratory/Team: **Pervasive Electromagnetic Laboratory, University of Rome Tor Vergata, Rome, Italy**
Role: Provision of instrumental tools to perform the electromagnetic characterization of the wearable tag antenna presented in Chapter 5.

Laboratory/Team: **MultiFAB project, Laboratoire d'analyse et d'architecture des systèmes (LAAS-CNRS), Toulouse, France**
Role: 3D printing of the dielectric structures presented in Chapter 4.

### 1.4.2 Research projects

**LabEX (Cluster of Excellence) AMADEus (Advanced MAterials by DEsign) research project** The overall ambition of this research project is to become a worldwide-recognized major cluster in materials science, engineering and technology, carrying out scientific research and innovation at the interfaces of chemistry, physics, biology and engineering [1].

**Bio3 research project** The project, BIOcompatible and BIOfunctional porous electrodes for miniaturized enzymatic BIOfuel cells, aims to design a fully integrated, extremely miniaturized and perfectly biocompatible glucose/O2 biofuel cell as an *in-vivo* source of electricity that may power for example, a subcutaneously implanted, continuous glucose monitor for diabetes management.

1. Source: https://amadeus.labex.u-bordeaux.fr/en/

# Chapter 2

# Wireless *In-vivo* biofuel cell monitoring

Prior to design any hybrid-powered implantable devices, that use glucose and oxygen to produce energy, the Biofuel cell (BFC) operation has to be validated *in-vitro* and, if possible, *in-vivo*. Unfortunately, typical monitoring of implanted BFC involves anesthesia, resulting in heavy follow-up and very limited number of measurements. The goal of the work presented in this chapter will be to monitor continuously the activity of a BFC in a rodent, paving the way for a wireless telemetry tag, with possible human wearable application.

## 2.1 Introduction to the experiment

The wireless monitoring of body parameters is nowadays one of the most interesting aspect of the Ultra High Frequency (UHF) Radio Frequency Identification (RFID) standard technology. In fact, thanks to the advancements in low-power electronics, continuously monitoring the physiological signals (e.g. ECG, temperature, heart rate) are increasingly realistic[147][148]. By using the UHF-RFID technology, the wireless sensor can be implemented as totally passive, as shown in Sec. 1.3.1, avoiding the drawbacks due to battery presence.

Besides human health, an interesting application of this technology is the monitoring of laboratory rodents, commonly used in medical research to investigate various diseases [149]. In this case the wireless monitoring is even more critical: wired telemetry often leads to complications, limiting thus the movement of the animals and modifying their natural behavior.

Various BFCs operating *in-vivo* in living rats were reported in literature [150, 151, 152], but all of them have been measured with wires to retrieve the signal. Therefore, the animal is kept under anaesthesia or put in a small cage, where it is not free to move. More recently, a BFC implanted in a rabbit was monitored for two months wirelessly, using a Bluetooth link [153]. In this case the Bluetooth technology requires batteries to work.

Alternatively, UHF-RFID technology appears as an elegant way to monitor BFCs. In this case no batteries are necessary and the antenna can be placed on the back of the rat and connected to the BFC implanted subcutaneously. Fig. 2.1

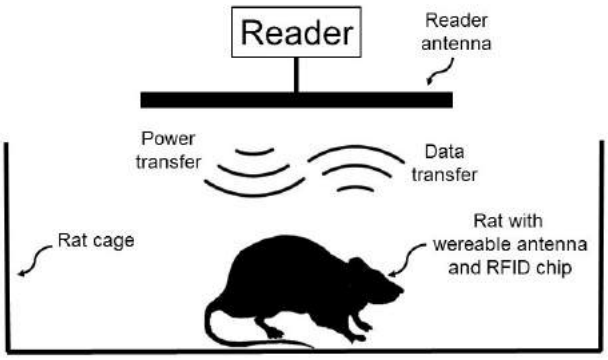


**Figure 2.1** – The setup of the proposed telemetry system.

shows the proposed monitoring setup: an active RFID reader placed on the top of the rodent cage interrogates (and powers) the RFID tag. Inside the cage, the animal wears a special designed jacket that includes the tag antenna, the RFID chip and the telemetry system. In this way the animal is free to move inside the cage while the BFC is being wirelessly, continuously monitored, securing a measurement that will not be affected by the rat behaviour.

To monitor and record the energy produced by the implanted BFC, an ADC-embedded silicon RFID Integrated Circuit (IC) (AMS-SL900A) was selected. This IC has two analogical inputs that can be used to connect the electrodes. Moreover, it has a built-in temperature sensor, allowing the monitoring of the temperature of the animal during the experiment, all without any external battery.

The following sections will describe the design and construction of a dedicated wearable antenna that will be connected to the chip. A special care will be given to the high dielectric constant and the dielectric losses of the rat tissues, which influences the input impedance of the antenna.

To insure the maximum telemetry Reading Range (RR): (i) the complex input impedance of the antenna and the chip have to be matched; (ii) the radiation characteristics of the antenna have to be optimized. Finally, (iii) the wearability of the antenna has to be taken into account, in order to make it comfortable to be carried by the rat.

In the next sections, all the designed antennas are presented, including *in-situ* characterizations on a rat.

## 2.2 Simulation and measurement methodology validation

This section presents an early antenna, developed to validate the antenna design process and the measurement setup used to characterize the RFID tag antenna.

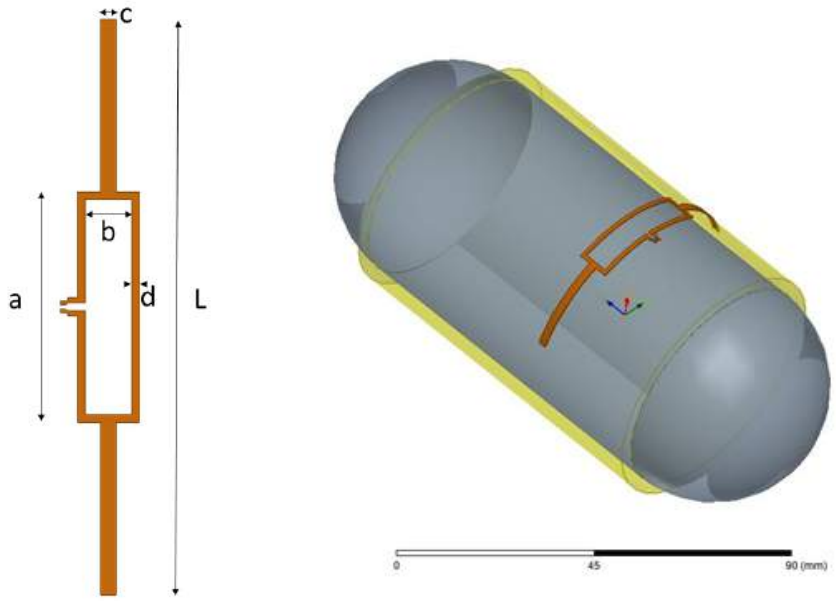


(a) (b)

**Figure 2.2** – Antenna 1: the designed antenna (a) and the full 3D simulated structure, including the rat model (b). L=75 mm, a=30 mm, b=6 mm, c=2 mm, d=1 mm.

### 2.2.1 Simulations performed

For this first antenna, a typical RFID input impedance of $Z_c = 20 - j300\,\Omega$ have been considered. Full wave FEM electromagnetic simulation have been performed using the HFSS software, to optimize the antenna impedance.

The selected antenna was a dipole with a square loop, providing the high inductive behaviour required. Fig. 2.2a shows the antenna with all the main dimensions, as well as the real case scenario (Fig. 2.2b). The antenna is wound around the surface of a rat model, having diameter 54 mm and height 140 mm. The material properties were defined as a weighted average upon all body tissues at 900 MHz [154], having the following values: relative permittivity $\epsilon_r = 55.03$ and electric conductivity $\sigma = 1.01\,\mathrm{S/m}$. In order to separate the antenna from the conductive body tissue, and to allow easy placement of the antenna on the animal, a spacer, having a thickness of 3 mm, modelled using electromagnetic vacuum ($\epsilon_r = 1$, $\sigma = 0\,\mathrm{S/m}$), was inserted in the simulation render. This object simulates the presence of an idealized jacket on the back of the rat.

The antenna was designed to match the chip impedance, taking into account the maximum allowed length of the antenna, given the rat dimensions, and the maximum bending radius.

### 2.2.2 Construction and measurements

Prototypes of the antenna were built, from 0.3 mm thick copper (2.3a) (rigid antenna) and 30 µm copper tape (flexible antenna) (Fig. 2.3b). Since the antenna has balanced configuration, it can not be measured on the (unbalanced) Vector

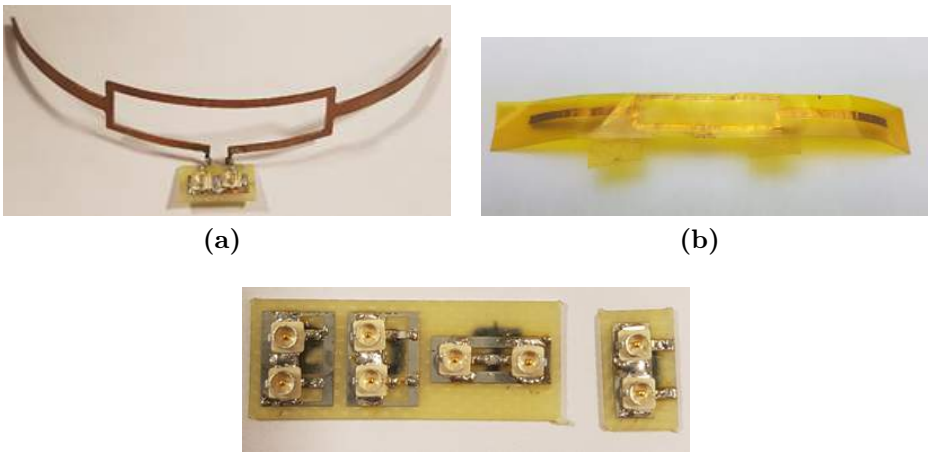

**(a)** **(b)**

**(c)**

**Figure 2.3** – The antenna measurements: the rigid antenna with the U.fl connection-based test fixture (a), the flexible antenna sandwiched in adhesive kapton (b) and the custom balanced calibration kit (c).

Network Analyzer (VNA) ports, since this would lead to measurements error [155]. Therefore, a especially designed calibration kit and a test fixture were developed in order to allow proper measurements without using a balun, as explained in the next section. A velcro jacket was also developed, in order to insure the simulated separation between the animal and the antenna, when it is worn by the rat.

**Test fixture and calibration kit** The balanced input of the designed antenna cannot be evaluated by the majority of measurement instruments, often terminated by coaxial port, i.e. unbalanced ports. In fact, if a balanced object is directly connected to an unbalanced port, the currents on the two terminal of the antenna are not equal, leading to inaccurate results. Since measurements using a balun or imaging method [156] are not the optimal choice, a method that leads to the correct evaluation of the antenna impedance, using a text fixture, is described in [157]. This test fixture consist of two unbalanced connector, that will be connected to a 2-port VNA, having common ground. Starting from the measured S parameters, the differential input impedance ($Z_d$) can be computed as:

$$Z_d = 2Z_0 \frac{1 - S_{11}S_{22} + S_{12}S_{21} - S_{12} - S_{21}}{(1 - S_{11})(1 - S_{22}) - S_{12}S_{21}}, \tag{2.1}$$

where $Z_0$ is the characteristic impedance of the transmission line.

In order to maximize the miniaturization of the test fixture, U.FL connectors were used. The developed text fixture was soldered to the two ends of the antenna, as 2.3a shows. In order to correctly measure the scattering parameters, a custom SOLT calibration kit was also fabricated (Fig. 2.3c).

The method was then briefly assessed by measuring two loads: 0 Ω (short circuit) and a 11 Ω resistor (RTC RMR/RC01 11R, having 10% tolerance). As Tab. 2.1 shows, the measured values are sufficiently comparable to the expected ones, confirming the unbalanced-to-balanced transformation.

**Table 2.1** – The results of the validation procedure.

| Load | $Z_d$ @ 100 MHz ($\Omega$) | $Z_d$ @ 900 MHz ($\Omega$) |
|---|---|---|
| Short | $0.2 + j0.1$ | $1.3 + j3.5$ |
| 11 $\Omega$ | $10.9 + j0.7$ | $11.3 + j6.3$ |

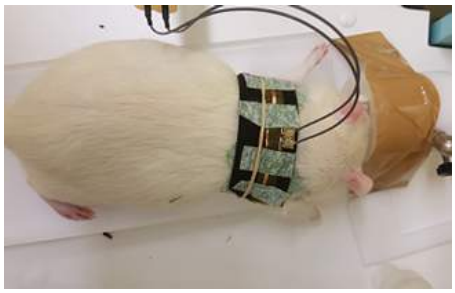

**Figure 2.4** – The rat during a measurement.

**Results obtained** After having validated the measurement method, antenna measurements where performed in air and on a sleeping rat, in order to compare the simulated and built prototypes.

Fig. 2.4 shows the rat wearing the jacket and the antenna, connected to the the test fixture.

Measurements were performed on a laboratory rat (Sprague–Dawley) that has not been bred for this study. In order to place the antenna on its back, the animal was anesthetized during the dressing and measurement process.

Fig. 2.5 shows the simulated and measured input impedance of the antennas, in air (only the rigid antenna was measured) and on the rat. As it can be seen, the rigid antenna has a behaviour highly comparable with the simulation, while the impedance of the flexible one slightly differs from the expected values. This is mainly explained by the unreliability related to the deformation of the antenna shape during the measurement, due to the flexible characteristics of the latter.

### 2.2.3 Conclusion

Though validating the antenna design process, the study mainly highlighted the influence of the body tissues on the impedance of the structure.

One solution to this problem could be the design of an antenna independent from the medium where the structure is placed, as presented in the next section.

## 2.3 Complementary Split Ring Resonator Antenna

This section reports the efforts made to screen the antenna from the underneath tissues, in order to minimize impedance variations related to the rat movement. It presents a complete communication setup including the transmitter (reader) and receiver (tag) antenna. Simulations, using Ansoft High-Frequency Simulation

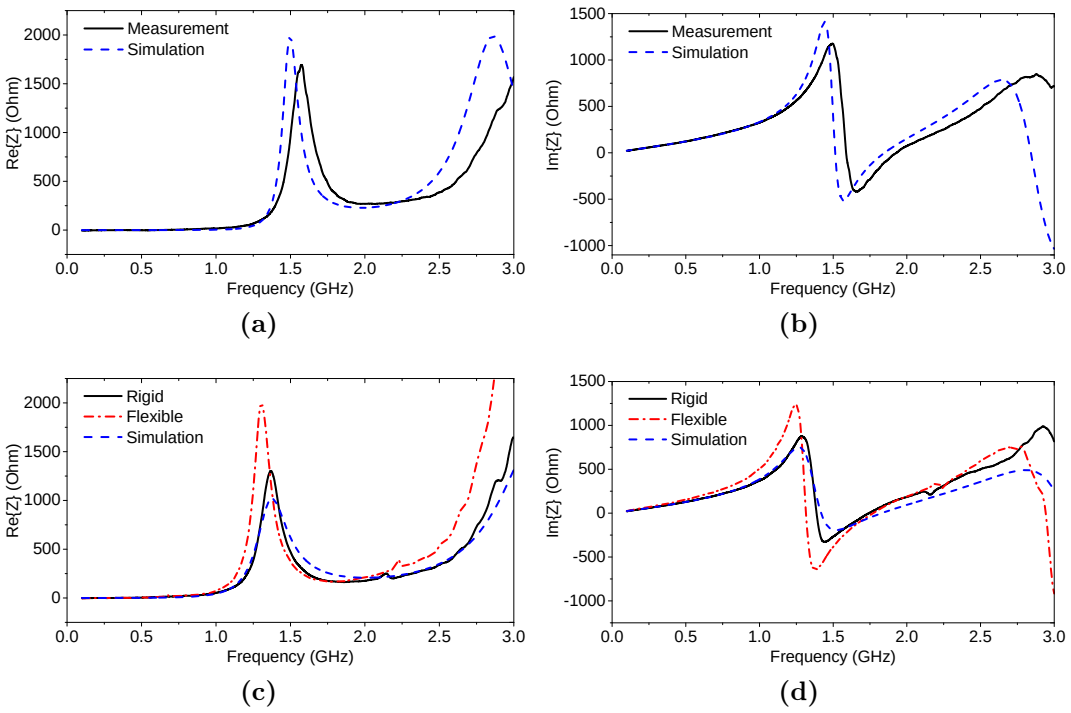


**Figure 2.5** – The antenna input impedance: Comparison between simulations and measurements in air (rigid antenna only), real part (a) and imaginary part (b); and on the rat (both antennas), real part (c) and imaginary part (d).

Software (HFSS), were performed and they were validated through measurements, including *in-situ* experiments on laboratory rats.

### 2.3.1 Design of the monitoring system

**Tag antenna** The main challenge in a wereable telemetry antenna design is to circumvent the biological impact on its operation. Conventional RFID tag antennas, e.g. meandered dipoles, tend to be highly affected by the presence of tissue mediums, and are not an optimal choice. In order to screen the antenna from the complex medium, we have chosen to design a grounded slot antenna. We have built a square tag antenna inspired by the complementary split ring resonator topology [158], using Rogers RT/Duroid 6002 ($\epsilon_r = 2.94$, $\tan\delta = 0.0012$) substrate. It consists of a square metal patch and three concentric folded slots, as seen in Fig. 2.6a. 3D FEM simulations are performed, with a simplified model of the rat, having dielectric characteristic equal to a representative weighted average of all rat tissues ($\epsilon_r = 55.03$, $\sigma = 1.01\,\mathrm{S/m}$) [154]. In order to further screen the E field of the antenna from the complex medium, a copper foil, having dimensions 90x75 mm was integrated in the rat jacket.

To emulate a real application the antenna was designed to conjugate matching the complex input impedance of an RFID chip having impedance $Z_c = 31 - j320\,\Omega$, having a sensitivity of -7 dBm.

Simulations were performed by varying the geometrical parameters of the tag in order to match the above mentioned impedance at 900 MHz. The resulting

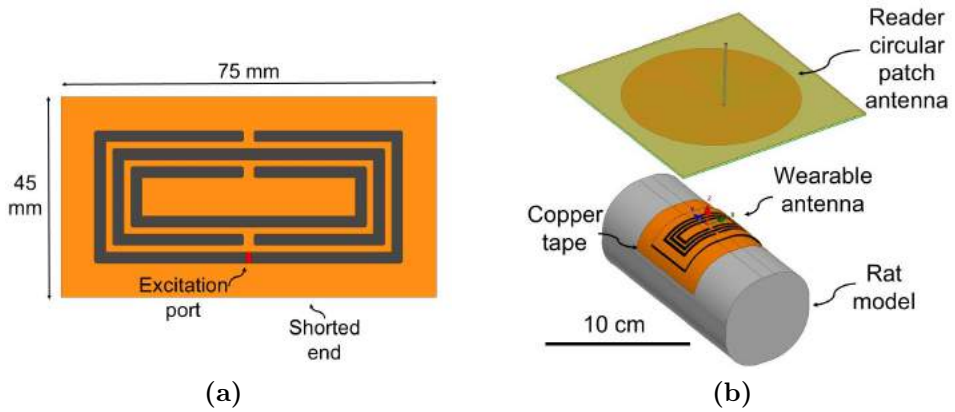


**Figure 2.6** – The slot antenna: Antenna shape and dimensions (a) and the simulation setup (b)

structure has a footprint of 75x45x1.52 mm.

**Reader antenna** By analyzing the simulated field emitted by the tag antenna, it turned out that the best reader structure has to emit a strong electric field. Moreover, since the rat would be placed into the cage, an omnidirectional antenna is not needed. These assumptions led to the selection of a 50Ω coaxial-fed circular microstrip patch antenna as reader antenna. This component was build on a 1.54 mm-thick Rogers RT/Duroid 5870 ($\epsilon_r = 2.33$, $\tan\delta = 0.0012$) with a patch diameter of 125.2mm in order to match the resonance frequency of the tag antenna. Fig. 2.6b shows the complete simulation setup, including the two antennas and the rat model.

**Measurement setup** The two designed antennas were manufactured, by means of a precision milling machine with numerical control (by LPKF), and characterized using a Keysight E5061B Vector Network Analyzer. The patch antenna was tested with conventional 1-port measurement, but, since the wearable antenna has a balanced configuration, his input impedance and consequently the reflection coefficient were measured using the procedure described in Sec. 2.2.2. The antenna was then embedded in the jacket of a rat, in order to measure the input impedance and transmission parameters. To excite differentially the RFID tag, a balun (Mini-Circuits TCM1-83X+) was soldered to the antenna and connected to the VNA by means of an U.FL cable. The balun was then de-embedded during the data post-processing using the Advanced Design System (ADS) software (Fig. 2.7c). The custom SOLT calibration kit, presented in Fig. 2.3, was also used to secure correct measurements at the end of the U.FL cable. Measurements were performed on a Sprague–Dawley (Charles River Laboratories, L'Arbresle, France) female rat. In order to place the antenna on its back, the animal was anesthetized under 5% isoflurane during 2 minutes and then maintained anesthetized under 2.5% isoflurane with mask inhalation. Fig. 2.7b and 2.7c show the measurement setup for the impedance ($S_{11}$) and transmission ($S_{21}$) measurements, respectively.

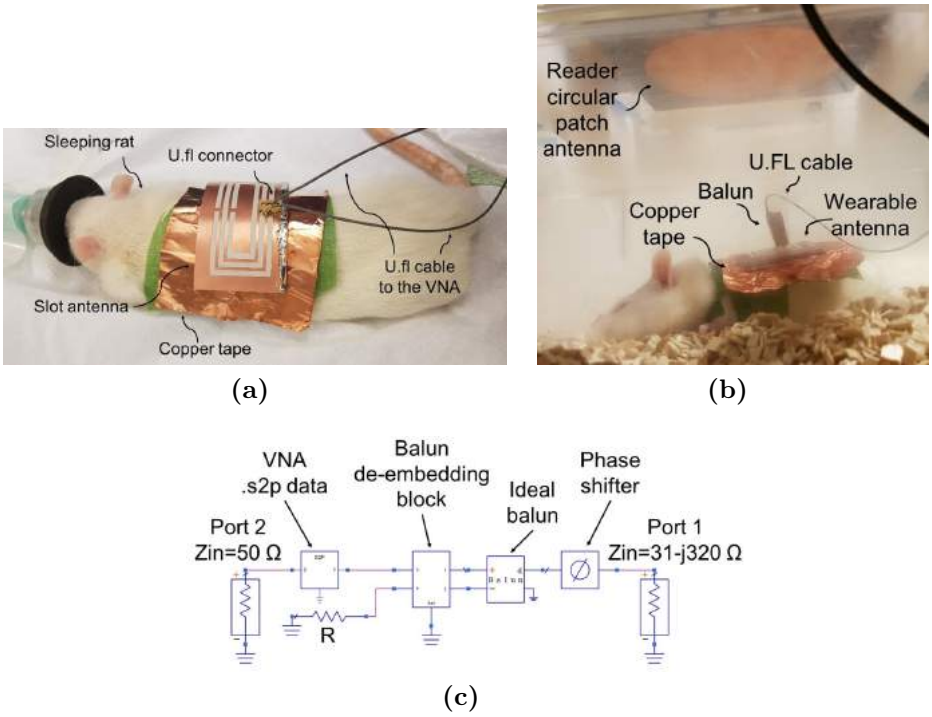


**Figure 2.7** – The measurement setup: Reflection (a) and transmission (b) measurements, and the de-embedding post-processing routine (c).

### 2.3.2 Results

Fig. 2.8 shows the simulated and measured reflection coefficients of the manufactured antennas. In particular, for the rat antenna, two measurements are shown: one following the procedure of Sec. 2.2.2, one with the balun. Both are in good agreement with simulations. Most importantly, Fig. 2.8 shows that the tag antenna characteristics are minimally affected by the presence of the biological tissue.

Transmission measurements were implemented in order to map the efficiency of the link in the whole area of the rat cage. This efficiency is defined as:

$$\eta = \frac{P_r}{P_t} = |S_{21}|^2 , \tag{2.2}$$

where $P_r$ and $P_t$ are, respectively, the received and transmitted power, and $S_{21}$ is the scattering parameter measured by the VNA.

To map the efficiency, the position of the rat antenna was fixed and the patch antenna, placed 10.5 cm above it, was scanned in the x and y direction, with a step of 3 cm, to cover the whole surface of a typical rat cage. Due to the difficulty to perform this experiment with the rat, and considering that the antenna response is not affected by the animal (Fig 2.8), both simulations and measurements were performed in air, respecting the polarization of the patch antenna.

Fig. 2.9a shows the resulting efficiency map, with measurements matching well the simulations, although with a slight asymmetry. This could be explained by the presence of the balun circuit and the cable used during measurements that

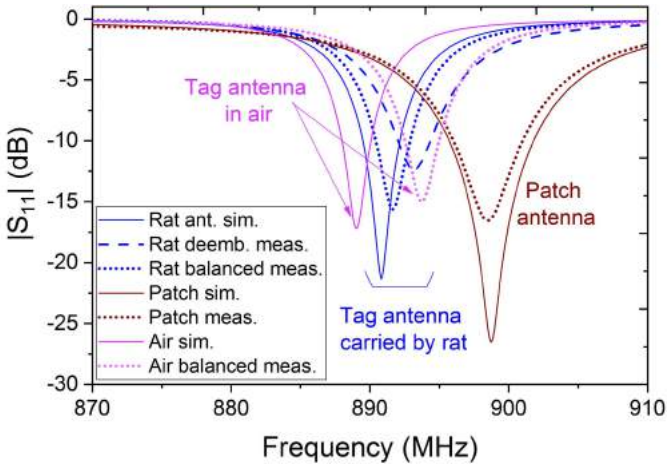


**Figure 2.8** – Simulated and measured reflection coefficients of the developed antennas. The S11 parameters of the patch antenna refers to 50 Ω while the ones of the rat wearable antenna refers to the complex input impedance of the RFID chip (31-j320 Ω).

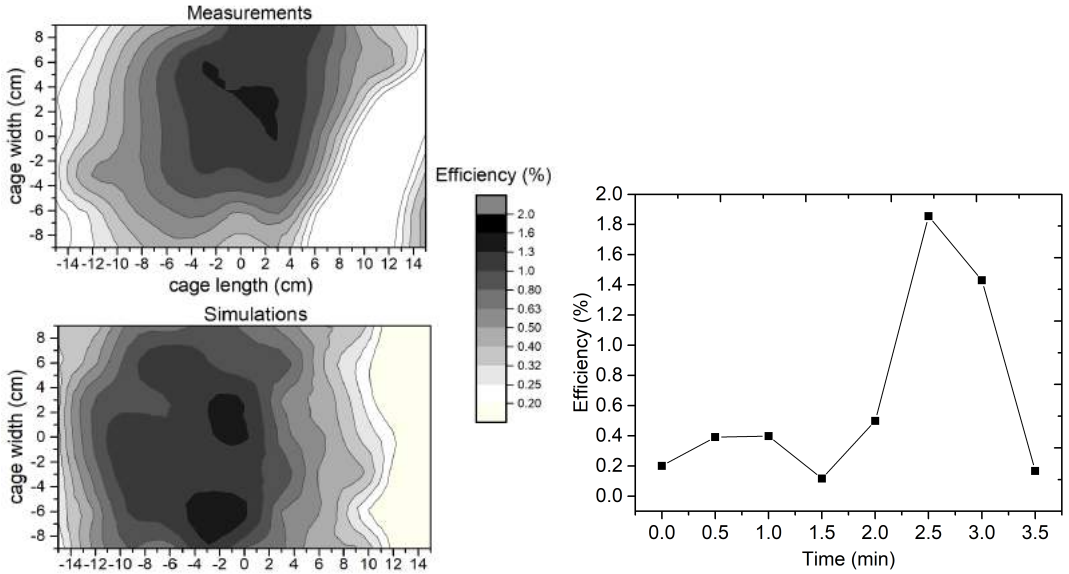


**(a)** **(b)**

**Figure 2.9** – The transmission measurements: Efficiency map (a) and the transmission efficiency, as a function of time, recorded while the rat was free to move inside his cage (b).

may interfere with the Electromagnetic (EM) field in the neighbourhood of the tag antenna.

Meanwhile, in both cases the minimum efficiency registered is largely above (about one order of magnitude) the minimum efficiency required to communicate with the chip ($\eta_{min}$ = 0.02% when Pt=30 dBm) ensuring thus the RFID link wherever the rat would be located.

In order to further validate the design, the efficiency was recorded when the antenna was carried by the awaken rat moving freely inside his cage (2.9b). It is seen that for all the recorded values, the efficiency was above $\eta_{min}$ and consistent with mapped efficiency values without the animal, confirming the good isolation of the antenna from the biological tissue of the rat. The high variations of the efficiency versus time could be explained by the fact that the rat was moving fast inside the cage, occupying places of very high and very low efficiency. Furthermore the rat was often rotating and standing on two legs, which was not considered for the field mapping measurements.

### 2.3.3 Conclusion

Pared with a linearly-polarized patch, the slightly curved, slotted ring antenna clearly attains exceptional transmission efficiency, securing wireless telemetry reading in any location of the cage. The power transfer efficiency is, in the worst case, about a factor of ten above the minimum efficiency required to power the chip, when 1 W is emitted from the reader.

However, this achievement is traded in for a low-wearability: the resulting tag is too thick and stiff for appropriate long term wear. Therefore, in the following work, we have given priority to the wearability of the antennas.

## 2.4 Wearable loop antenna

In this section a highly wearable antenna is presented. On the contrary of the previous one, this structure is very thin and foldable, and can be placed in the neighbourhood of the skin. Due to the absence of any shielding from the tissues, however, this antenna is highly affected by the presence of the body, resulting in poorer radiation characteristic with respect to the one in previous section.

The antenna was designed to conjugate match the SL900A chip, presented in section 2.1, and to have sufficiently RR to perform the monitoring of the BFC implanted in the rat while the animal is placed in the cage.

In the next sections, the design flow as well as the measurements performed are presented.

### 2.4.1 Introduction

Introduced in past years, the concept of epidermal electronics brings radical change to the wearable antenna design process, by prioritizing extra lightweight electronic payload, to ensure longterm (weeks) wearability [159, 160]. This category of devices consists in very thin, single-layer foldable antennas, attached on the skin

at a maximum of one millimetre from it, by means of a flexible (and sometimes elastic [160]) substrate.

Epidermal antennas were implemented to design wireless RFID sensors that continuously monitor the body temperature [133] (with a reported gain of the order of -13 dB) and both skin temperature and humidity [141] (with a reported maximum gain of -16 dB). The state-of-the-art gain for this category is currently of the order of -13 dB, taking into account an homogeneous human model ($\epsilon_r = 41.2$, $\sigma = 0.95$ S/m).

### 2.4.2 Tag antenna design

The selected chip in this design is the AMS-SL900A, characterized by an input impedance $Z_c = 123 - j303\,\Omega$ and a sensitivity $p_{min} = -6.9$ dBm in battery-less mode. It operates in the whole UHF-RFID frequency band (860-960 MHz) [135].

A recent study has indicated loop antennas as the best choice for an epidermal antenna [146]. But, due to its poor isolation between the RF and the DC, the SL900A cannot be connected to a closed path, that would lead to a DC short circuit. Therefore, simple loop antennas, as well as classical T-match can not be implemented.

The antenna was designed as a folded dipole, coupled to a square loop, in order to maintain a loop shape. 1 mm spacing is considered between the antenna on the animal skin, to reduce the electric field penetration into the tissues. As for the flexibility, 40 µm thick Kapton ($\epsilon_r = 2.94$, $\tan\delta = 0.0012$) was selected as substrate, and 30 µm copper as metal. The trade-off between size and gain have led to a footprint of 39.4x39.4 mm$^2$, resonating at $f_c = 924$ MHz. The design includes the chip pads and a 30 nH inductor, that is implemented in order to compensate the capacitive influence of the tissues (and conjugate match the highly capacitive RFID chip impedance). Figs. 2.10a and 2.10b shows the resulting design and the simulated structure, including the rat model.

Fig. 2.10c shows the resulting simulated $S_{11}$. The antenna shows a resonance at $f_c = 924$ MHz and, as a result of the tissue losses, the -10 dB bandwidth is equal to 70 MHz, allowing to work in almost all the operating band of the IC. As Fig. 2.10c shows, the maximum gain of the antenna is quite flat in the whole range of frequency, having comparable values with respect to the state-of-the-art epidermal tags [133, 141]. Finally, Fig. 2.10d shows the simulated radiation characteristics of the antenna at the resonance frequency. As shown, design efforts were made to make the antenna highly omnidirectional in the upper semi-sphere of the animal. This allows to monitor the rat while it is moving and rotating inside the cage.

The RR of the tag can be estimated by the following, as shown in 1.3.1:

$$RR = \frac{\lambda_0}{4\pi}\sqrt{\frac{EIRP \cdot G_r \cdot \tau}{p_{min}}}, \tag{2.3}$$

where $EIRP$ is the equivalent isotropic radiated power, $G_r$ is the gain of the receiver antenna, $\tau$ is the power transmission coefficient and $p_{min}$ is the sensitivity of the RFID chip. By assuming the maximum allowed radiated power in the EU (EIRP=3.2 W), the resulting RR is RR=46.5 cm. Therefore, the resulting RR is high enough to allow the rat monitoring.

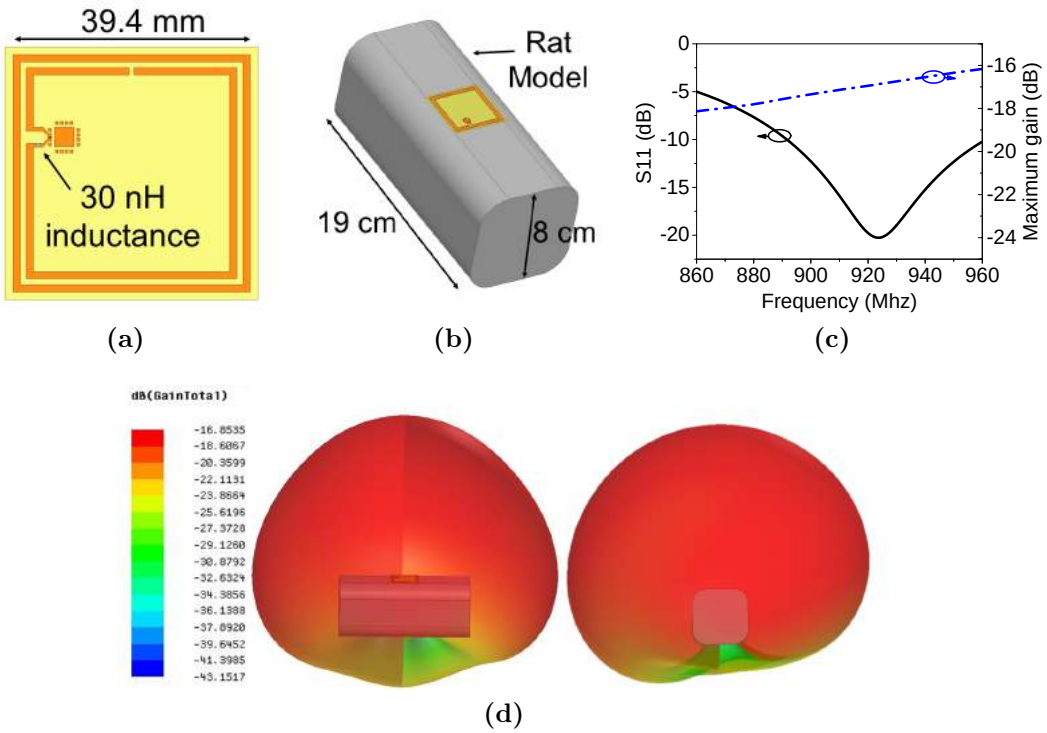


**Figure 2.10** – The wearable loop antenna: Antenna shape (a), simulated structure (b), resulting reflection coefficient and maximum gain with respect to frequency (c), and the radiation pattern (d).

### 2.4.3 Tag fabrication and measurement performed

The optimized structure was manufactured using 40 µm kapton as substrate. The antenna was implemented with copper tape (30 µm), cut by means of a laser cutter. The copper tape was first fixed on a bulk metal plate and etched by laser. The remaining copper traces were then placed between two layers of 40 µm kapton tape, to protect both sides of the antenna and avoid the displacement of the routes. On the upper kapton layer windows were etched by laser, to allow the soldering of the components (IC, inductor, electrodes connector). The connector was placed on the antenna in order to allow the connection of the BFC electrodes. Fig. 2.11a shows the developed RFID sensor tag.

As first validation, the antenna was placed on a velcro band and worn by the designer (Fig. 2.11b). The antenna was then measured by means of an RFID reader (AMS AS3993 Fermi), delivering 22 dBm, connected to the patch antenna presented in the previous section (Fig. 2.6b).

To further validate the structure, the tag antenna was then placed, by means of a custom-designed velcro jacket, on the back of a Sprague–Dawley rat, in order to check the communication in a real case scenario (Fig.2.11c). Measurements were then performed with an AMS AS3993 Radon reader, having 1 W of transmitted power.

### 2.4.4 Results

As Fig. 2.11d shows, the arm-worn tag was placed at a distance of about 15 cm from the reader antenna, emulating the distance between the rat and the top of the cage. As a result, the tag was successfully read by the reader. Moreover, by using the in-built temperature sensor of the chip, the temperature captured by the IC was displayed on the computer connected to the reader (Fig. 2.11e).

The same procedure was used to validate the communication link when the antenna was worn by the rat (Fig. 2.11f).

### 2.4.5 Conclusion

An highly wearable antenna was developed. Having dimensions of 39.4x39.4 $mm^2$, this compact antenna has a theoretical RR of 45 cm, enough to perform continuous monitoring of a rat placed inside his cage.

The prototype was validated by measurements on a human arm and on a laboratory rat. In both cases the reader software was capable to read the temperature registered from the IC.

In order to further miniaturize and optimize the reading characteristic of the tag antenna, a new structure was designed and built, as explained in the next section.

## 2.5 Wearable monopole antenna

The loop antenna just presented was working well enough to perform the measurement of a BFC implanted in a rat. But it was not the optimal choice to maximize the communication link (telemetry RR). This section present the novel design, as well as the measurements performed on a rat, with two implanted electrodes.

### 2.5.1 Tag antenna design

As presented in the previous sections, the IC selected to perform the BFC monitoring was the AMS-SL900A chip. This IC has input impedance $Z_c = 123 - j303\,\Omega$ at UHF-RFID frequencies and a sensitivity $p_{min} = -6.9$ dBm in battery-less mode. Moreover, the analogical inputs of the chip are capable to measure voltages between 310 and 620 mV, covering thus most of the voltage range of a BFC [52].

Since the SL900A IC has an unbalanced RF configuration, dipole-like structures, like the one presented in section 2.4 and others shown in literature [141, 161] are not the optimal choice. Therefore, a folded monopole structure was designed. The antenna is terminated by a loop, in order to enhance the inductive behaviour required, and the width of the far-end side is augmented, to increase the bandwidth of the tag. As for the last antenna, a lumped inductor is inserted, to easily match the impedance of the chip. The lodgements for the chip and the electrode connector, that allows the connection of the BFC electrodes to the input ports of the chip, were inserted onto the ground plane, to minimize the tag dimensions.

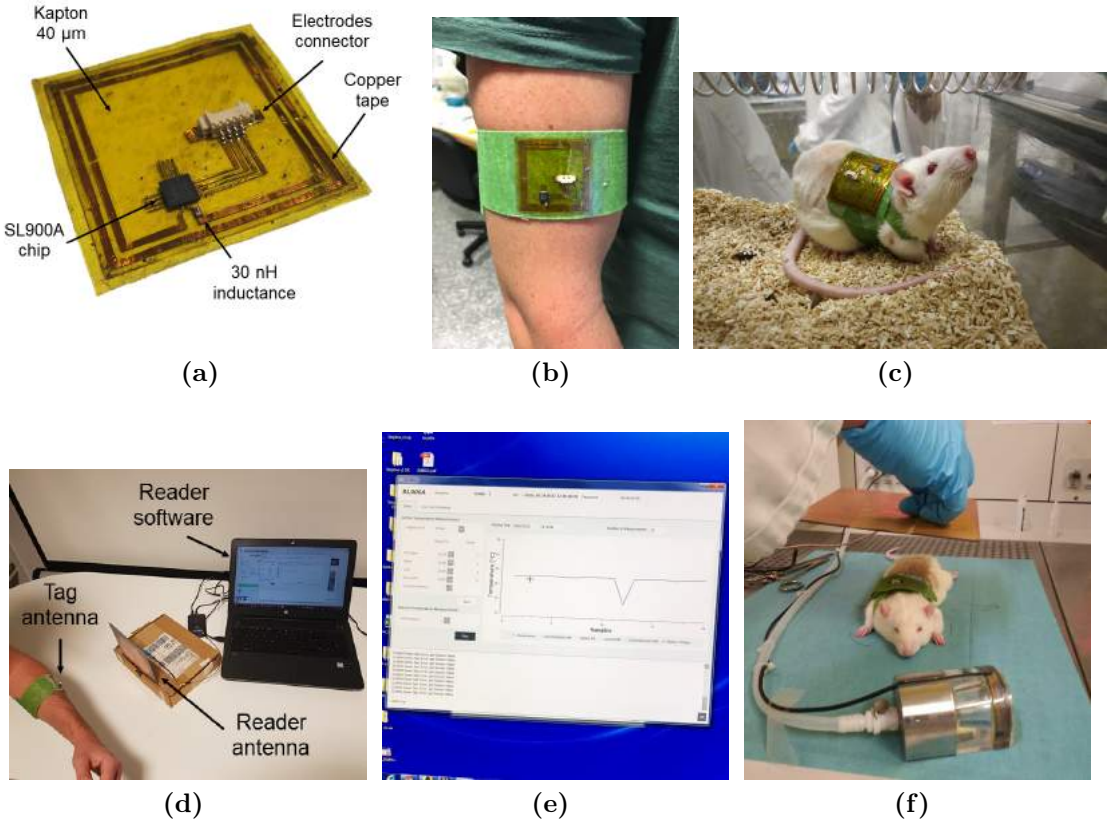


**Figure 2.11** – The wearable loop antenna measurements: Antenna prototype (a), the antenna worn by the designer (b), the antenna worn by the rat (c), the reading measurements setup (d), the monitored temperature (e), and the reading measurements on the rat (f).

Finally, a lumped capacitor is included in order to enhance the RR of the tag in battery less mode, as suggested by the manufacturer [135].

In continuity with the design of Sec. 2.4, to insure high wearability, a flexible and low-weight 40 µm thick Kapton ($\epsilon_r = 2.94$, $\tan\delta = 0.0012$) was selected as substrate and 30 µm copper was used as metal. Moreover, in order to validate the design, a first prototype was developed using a semi-foldable 0.51 mm thick Rogers RT/Duroid 5880 ($\epsilon_r = 2.20$, $\tan\delta = 0.0004$).

Fig. 2.12a shows the resulting structure, optimized using the HFFS (Ansoft, Pittsburgh, PA) simulation tool. The flexible antenna is specified for two different cases. The first one (Ant1) is the classical epidermal electronic case, where the antenna is placed with a separation of 1 mm from the skin, to insure high-wearability (in the simulations vacuum was used as medium between the antenna and the rat). In the second case, in order to simulate a real-case scenario (Ant2), a bio-silicone ($\epsilon_r = 2.2$, $\sigma = 0.005$ S/m) jacket, having thickness of 3 mm was also optimized. This is because sticking the antenna directly on the skin of the animal can cause skin inflammation [162]. Fig. 2.12b shows the 3D simulation model. Finally, as mentioned before, a third antenna (Ant3) was dimensioned using Rogers substrate, to validate the whole design. This antenna was designed to be placed at a distance of 1 mm from the rat skin, similarly to the first antenna.

In all cases, as for the previous antenna, the rat was designed as a parallelepiped object having rounded edges, as Fig. 2.12b shows. The material used was defined as a weighted average upon all body tissues at 900 MHz [154], having the following values: relative permittivity $\epsilon_r = 55.03$ and electric conductivity $\sigma = 1.01$ S/m. The rat model dimension were 19x8x8 $cm^3$.

Tab. 2.2 shows the resulting dimension, inductors and capacitors for the three cases taken into account. In continuity with the last design, the final tag external footprints are a trade-off between antenna size and gain.

Fig. 2.12c shows the simulated reflection coefficient of the three antennas, taking into account the chip impedance as reference one, and the maximum realized gain. This parameter, as presented in 1.3, is defined as $G_r^{max} * \tau$, where $G_r^{max}$ is the maximum value of the antenna gain and $\tau$ is the power transmission coefficient. The first two antennas were designed to operate in the 915 MHz band. While, for the third one, the operating central frequency (906 MHz) was chosen to be in the middle of the UHF-RFID bandwidth. As Fig. 2.12c shows, the antennas resonate at the design frequency, they have a -10 dB bandwidth of 64.3, 65.8 MHz and 55.0 MHz, for Ant1, Ant2 and Ant3 respectively, and a -3 dB bandwidth that covers all the UHF-RFID spectrum, thanks to the tissue losses.

Fig. 2.12c also shows the behaviour of the maximum realized antenna gain with respect to frequency. As a result, for all structures, the gain is quite flat in the antenna bandwidth and takes values in the order of -15 dB, comparable with others epidermal electronics antennas. Thanks to the bigger distance between the structure and the biological tissues, Ant2 has a gain slightly higher than the other structures, being at the same time quite smaller, as Tab. 2.2 evidences. This, because design priority was put to the miniaturization of the structures, while keeping a realized gain that insures enough RR to monitor a rat in its cage.

As a final remark, since the horizontal segments of the antennas are not participating in the radiation process, the antenna can be easily adapted to resonate at

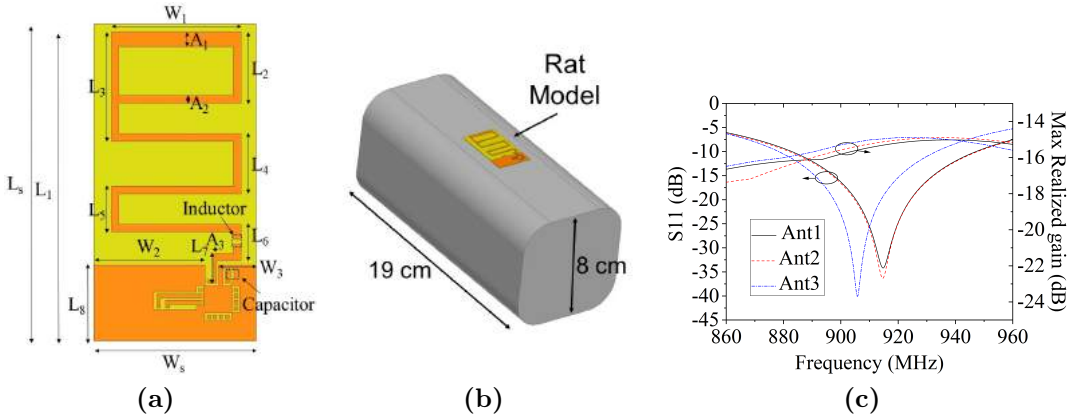


**Figure 2.12** – The wearable monopole antenna: Antenna shape (a), simulation box (b), resulting simulated reflection coefficient and maximum realised gain with respect to frequency (c).

**Table 2.2** – The dimensions of the designed antennas, including the lumped capacitor and inductor.

| Case | $A_1$ (mm) | $A_2$ (mm) | $A_3$ (mm) | $W_s$ (mm) | $W_1$ (mm) | $W_2$ (mm) | $W_3$ (mm) | L (nH) | C (µF) |
|---|---|---|---|---|---|---|---|---|---|
| Ant1 | 2 | 1 | 0.5 | 25 | 18.4 | 18.8 | 5 | 8.2 | 2.2 |
| Ant2 | 2 | 1 | 0.5 | 21.5 | 17.2 | 14.7 | 5 | 16 | 2.2 |
| Ant3 | 2 | 1 | 0.5 | 25 | 19.2 | 18.3 | 5 | 8.2 | 2.2 |
| | $L_s$ (mm) | $L_1$ (mm) | $L_2$ (mm) | $L_3$ (mm) | $L_4$ (mm) | $L_5$ (mm) | $L_7$ (mm) | $L_7$ (mm) | $L_8$ (mm) |
| Ant1 | 45 | 43.5 | 12 | 17 | 8 | 6 | 4.9 | 3.95 | 10.1 |
| Ant2 | 42 | 41 | 9.5 | 14.5 | 8 | 6 | 4.9 | 3.95 | 10.1 |
| Ant3 | 43 | 42 | 9 | 15.5 | 7.2 | 6 | 4.9 | 5 | 10 |

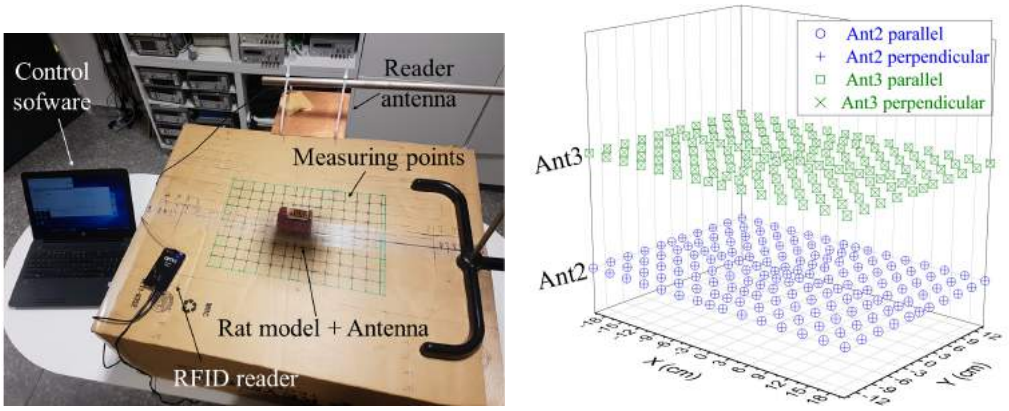


**(a)** **(b)**

**Figure 2.13** – The RFID link validation: the mapping measurement setup (a) and the achieved results (b).

all the worldwide UHF-RFID bandwidths, by acting to its overall width without changing the radiation characteristics.

Starting from the simulation, the resulting RRs, obtained by implementing Eq. (2.3) and by assuming the maximum allowed radiated power in the US (EIRP=4 W) have been computed. The resulting maximum RR are $RR_1 = 63$ cm, $RR_2 = 65$ cm and $RR_3 = 65$ cm for Ant1, Ant2 and Ant3 respectively, high enough to allow the rat monitoring.

### 2.5.2 RFID link validation

A measurement setup has first been defined in order to verify the complete coverage of a surface equivalent to a typical rat cage. A half PET bottle, having a thickness of 0.5 mm, was filled with minced bovine meat, at room temperature (21-23° C), in order to simulate the animal body tissue. On its top, two different antennas (Ant2 and Ant3) were placed. For the Ant2 case, a 3 mm silicone patch was placed between the bottle and the antenna, to emulate the real case scenario. A grid, having the external dimension of 40 x 28 $cm^2$, typical dimension of a rat cage, was drown and the bottle position was swept in order to verify the communication between the tag and the reader. The reader antenna, a 5 dB gain circularly polarized antenna (Abracon APAES915R80C16-T), was placed on the top of the grid, at a distance of 40 cm from the cage bottom. The reader antenna was connected to the reader (AMS Radon), emitting 1 W of power. Fig. 2.13a shows the measurement setup for Ant2.

Two rat positions were taken into account, for each antenna. One with the bottle axis parallel to the ground (Fig. 2.13a) and one with the bottle axis perpendicular to the floor, in order to mimic two most frequently positions assumed by the rodent while placed inside it cage. For the second case, the tag antenna was always oriented facing the grid center.

Fig. 2.13b shows the achieved results: the tag was successfully detected by the reader. As a result, for all measurement point, for both antenna positions, the

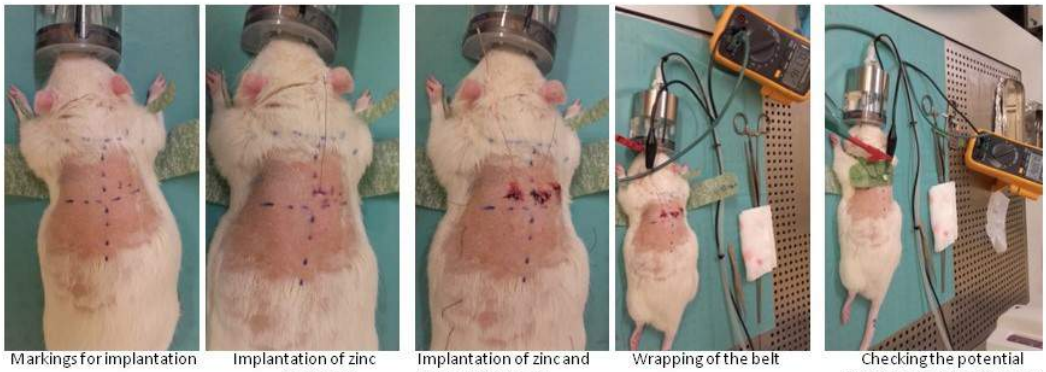


**Figure 2.14** – The implantation of the Zn-Cu electrodes inside the rat and the measurement of the open circuit voltage.

RFID link was established. Therefore, the rat should be detectable in the whole cage surface.

### 2.5.3 Preliminary *in-vivo* measurements

As first validation mark, in order to emulate a real case scenario, a wireless measurement of the voltage delivered by two electrodes implanted in a rat was performed, as explained in this part. For this purpose, the semi-flexible Ant3 was used.

**Implantation of the electrodes** Since a BFC delivers a typical voltage between 0.1 and 0.5 V [50], zinc and copper electrodes were selected to emulate this potential generation. In fact, thoses electrodes give a typical voltage of about 800 mV in saline water [163], that could be modulated by means of a variable resistance to get the typical voltage of a BFC.

A 250 µm zinc and a 500 µm copper electrodes were implanted inside the back of a rat for 3 cm. The open circuit voltage, measured by means of a digital multimeter, was about 700 mV. Fig. 2.14 shows some steps of the implantation process.

**Wireless voltage measurement** A custom designed velcro jacket was then wrapped around the animal and the antenna was placed on it. The two electrodes were plugged in the electrodes connector.

Since the open circuit potential was outside the range of the RFID chip (310-620 mV), a variable resistance, placed in parallel with the chip input port, was varied and the potential was continuously checked with the multimeter. The resistance value was fixed to R=27.8 kΩ in order to insure a potential of about 0.5 V between the electrodes.

The potential between the electrodes was then successfully monitored in different conditions: (i) when the rat was sleeping, with the antenna placed about 15 cm far from it, (ii) when the rat was recovering from the anaesthesia inside the cage

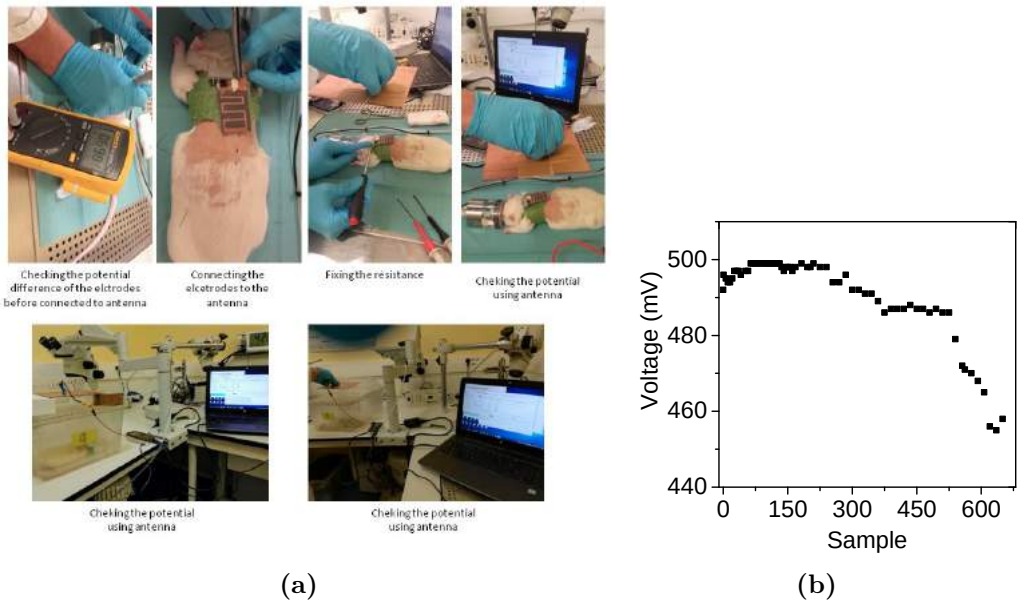


**(a)** **(b)**

**Figure 2.15** – The wireless measurement of subcutaneous implantation of two electrodes in the rat (a) and the voltage recorded while the rat was placed inside the cage (b).

(distance about 20 cm) and (iii) when the rat was awake inside the cage (distance about 20 cm). Fig. 2.15a shows some steps of the wireless measurement process.

The voltage signal registered when the rat was placed inside the cage is reported in Fig. 2.15b. The values are highly comparable with the measurements performed using the multimeter. A small drop of the potential was registered during the measurement, as shown in the graph, due to the oxidation process of the reaction. The total duration of the wireless monitoring was about 30 minutes.

As a conclusion, the RFID link and the voltage monitoring was validated *in-vivo*, the next step was to monitor a working BFC implanted inside the rat.

### 2.5.4 *In-vitro* and *in-vivo* biofuel cell monitoring

After having validated the link and the measurement capability, the continuously monitoring of the BFCs [1] was performed and the resulting voltage values were

1. The BFCs used in this section were implemented with the following process:
**Fabrication of macroporous gold electrodes for biofuel cell**: Cylindrical macroporous gold electrodes were made using a procedure described in previous work [60]. The colloidal template (silica beads with d=1170 nm) was synthesized and surface functionalized by following a reported procedure [60, 164]. Thickness of the electrodes can be controlled by number of macroporous layers that are easily measured by following the current oscillations. Macroporous gold electrodes of 11 half layers thickness were used for all the experiments *in-vitro* and *in-vivo*.
**Immobilization of enzymes onto macroporous electrodes**: Bilirubin Oxydase (BOD) mutant 52.84 mg/mL 16 µl (final concentration 6 mg/mL) was used for one electrode. The immobilization was made in glass capillar, 3 minutes under vacuum and then overnight at 4 °C. The enzyme is mixed with buffer NaPi 50 mM pH=6. The second electrode was modified with Glucose Oxidase (GOx), 38.92 mg/mL 16 µl (final concentration 6 mg/mL). 4 µl of enzyme at the appropriate dilution are mixed with 7.35 µl of polymer and 4.77 µl of hydrogel (dissolved

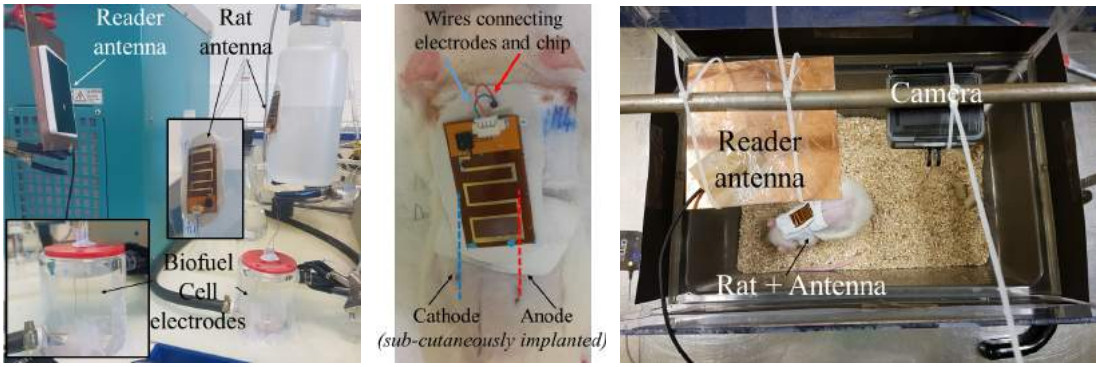


**(a)** **(b)** **(c)**

**Figure 2.16** – The *in-vitro* and *in-vivo* BFC monitoring setup: the *in-vitro* setup (a) the rat with implanted electrodes and wearing the antenna (b) and the *in-vivo* setup.

compared to *in-vitro* experiments. The following sections present the measurement performed and the results achieved.

### *In-vitro* measurements

Before implementing the *in-vivo* monitoring, the BFC was wirelessly monitored *in-vitro*, in order to allow comparison with the *in-vivo* results. Fig. 2.16a shows the measurement setup. In continuity with the link mapping, the circularly polarized antenna was connected to the RFID reader, emitting 1 W of power. On the other side of the link, the wearable antenna (Ant2) was placed on a bottle half-filled with PBS solution, in order to mimic the presence of the animal. To reproduce a real-case scenario, a patch of silicone was placed between the antenna and the bottle.

The BFC electrodes were placed in a temperature-controlled PBS solution, kept at 37° C, to mimic the natural body temperature. 5 mM of glucose were inserted in the solution, about the typical glucose concentration in a rat [165]. The solution was also saturated in oxygen, for repeatable measurement condition.

Finally, the electrodes were connected to the antenna connector and the open circuit voltage of the cell was recorded until it reached the minimum detectable value, i.e. 310 mV. One sample every 10 seconds was recorded.

### *In-vivo* measurements

In order to achieve the *in-vivo* monitoring of the BFC, a pair of modified, macroporus gold electrodes were implanted subcutaneously in the back of an Sprague Dawley female rat. Once the implantation was achieved, electrodes were connected to the inputs of the SL900A chip by means of the electrodes connector. In

in water at concentration 2 mg/mL). Immobilization is performed by secure the electrode on a glass slide and dropcast the mixture enzymes/polymer/hydrogel on top. The glass slide and the electrode are then kept overnight at 4 °C to allow complete drying and penetration. Enzyme is mixed with buffer NaPi 50 mM pH=5.1.

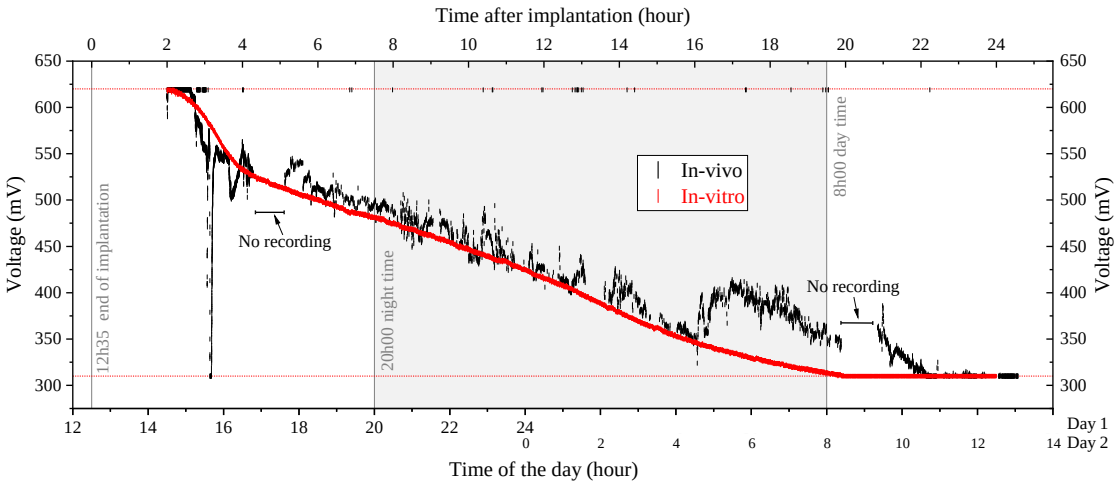


**Figure 2.17** – The *in-vitro* (red curve) and *in-vivo* (black curve) open circuit voltage of the BFC recorded wirelessly.

continuity with the *in-vitro* study, Ant2 was used for the experiment. Commercial jackets for rats (Harvard Apparatus) were used to immobilize the antenna, glued on a biosilicone patch on the rat back. Fig. 2.16b shows the rat once the electrodes were implanted, wearing the jacket and the antenna.

After surgery, the rat was placed inside its cage to recover from the anaesthesia and to perform the monitoring. Fig. 2.16c shows the measurements setup. The reader antenna was placed on the cage, at a distance of about 30-35 cm from the animal when placed in the cage center, in order to cover the whole cage surface. The same reader and reader antenna as the *in-vitro* experiment were used. In order to monitor the rat movement, a camera was also placed on the top of the cage, alongside the reader antenna.

Also in this case the BFC open circuit voltage was recorded from the end of the surgery (about one hour after the end of the implantation), until the minimum detectable value was reached. The recording time was about 24 hours, recording one sample every 10 seconds, in continuity with the *in-vitro* study.

During the whole recording, the animal, inside his cage, was placed in a temperature and humidity controlled room, with the day/night time automatically regulated.

### Results and discussion

Fig. 2.17 shows the resulting open circuit voltage of the BFC recorded *in-vivo* (black curve), compared to the *in-vitro* one (red curve). Please note that, for the sake of comparison, the *in-vitro* curve was shifted in time in order to overlap the *in-vivo* one.

As the figure shows, there is a very good agreement between the two curves. The black curve evidences more oscillations than the red one, due to the rat movement inside the cage, and the consequently electrode movements. The voltage values were higher than the maximum detectable value until about 2 hours from the end of the implantation, therefore no data were recorded. The curves evidence a fast

voltage drop between 2 and 4 hours after the implantation. This drop is reduced after 4 hours and continues regularly, in the *in-vitro* case, until the voltage reaches the minimum detectable value.

For the *in-vivo* case, the signal was registered continuously for the whole time, validating the wireless measurement setup. The absence of data from about 4.5 to 5.5 and from 20 to 21 hours from the implantation are due to the fact that the monitoring was stopped, since the animal was taken from the cage in order to perform X-ray scan to check the position of the electrodes. Moreover, videos using the camera were recorded during this time, for further study on the rat behaviour. The only significant signal interruption, of about 30 minutes, was recorded during the night, probably due an unfavourable animal position (e.g. having its body placed between the Transmitter (TX) and Receiver (RX) antenna), after that the communication is successfully recovered. Other, negligible, small signal interruptions were registered, especially during the night.

The black curve evidences an increase of the voltage after about 16 hours from the implantation. This could be explained by the fact that the rats are more active during the night than during the day. Therefore this increase can be due to increase of rat temperature (i), more oxygenation of the animal (ii), higher concentration of glucose (iii) or a movement of the electrodes (iv). The *in-vivo* voltage reached the minimum detectable value after about 22 hours from the end of the implantation.

### 2.5.5 Conclusion

A monopole RFID wearable tag antenna, designed to work with the SL900A IC, is proposed. Having compact dimensions (42x21.5 mm regarding Ant2), this passive system has a RR of more than 60 cm, allowing the wireless monitoring of a laboratory rat.

A first prototype was constructed on a semi-flexible substrate having thickness of 0.51 mm. This RFID sensor was able to monitor the voltage delivered by Zn-Cu electrodes implanted in a rat, while the animal was free to move inside his cage. The registered values are comparable to the ones given by a BFC, validating the measurement system.

The actual antenna was developed on kapton substrate, and a BFC was succesfully monitored *in-vitro* and *in-vivo*, for about 23 hours. Very good agreement between the two measurements were observed, evidencing good consistency of the BFC signal between the *in-vitro* ideal case, and the *in-vivo* real case scenario.

## 2.6 Conclusion of Chapter 2

This chapter was dedicated to the design of a wireless and batteryless communication link, in order to monitor the activity of a BFC implanted in a rat. Four antennas were designed, developed and then tested on an animal. The first one has validated the measurement setup used for the characterization of the antennas.

The complementary split ring resonator antenna was designed to be independent from the medium underneath it. The simulations were confirmed by measurement and the efficiency was mapped on a surface having dimension equals to the

ones of a rat cage. In the whole surface the efficiency was higher than the minimum efficiency required to perform the communication between the reader and the tag. As a limitation, the antenna was not so comfortable to wear, limiting the movement of the animal.

In order to make the antenna more comfortable, two epidermal antennas were designed and built. The first one, a loop-charged meandered dipole, having dimension of 39.4x39.4 mm, was developed on a 40 µm kapton structure. The resulting design has a maximum RR of 45 cm and was successfully tested when worn on a human arm and on the back of a rat. In particular the temperature registered by the IC was monitored wirelessly.

The last antenna, also designed to be highly wearable, was built on a semi-flexible 0.51 mm substrate, as a prototype, and on 40 µm kapton. The resulting compact flexible monopole antenna (42x21.5 cm), has a RR of 65 cm. This structure allowed the measuring of a BFC *in-vitro* and *in-vivo*, implanted in a rat, for about 24 hours. The resulting monitored open circuit potentials in the two different cases are highly comparable, showing the stability of the BFC respect to the body environment.

# Chapter 3

# Biofuel cell antenna project

The following sections describe the design and validation of the hybrid (biofuel cell and near field coupling) powered Implantable Medical Device (IMD) in this dissertation. To demonstrate the concept, this work aims at using two gold wires, wounded as a coil, to produce DC energy as biofuel cell electrodes while, at the same time, collecting the power transmitted from a dedicated magnetic source.

Please note that all the biofuel cells reported here are dummies: operating with largely non-optimized conditions, and orders of magnitude below their output power capability, but valid for the proof of concept.

## 3.1 Background

The powering and miniaturization of IMDs is one of the most studied research topic nowadays, as extensively shown in Chap. 1. Fig. 3.1 shows a possible power consumption scheme of an IMD as a function of time. This consumption can be divided in three different modes: a very-low power ("sleeping") mode, constantly active, needed to keep switched on the device; a low power mode, during which the device carries out its sensing and/or stimulating capability; and a high power mode, allowing to process and encrypt the data, and to communicate with the external unit. The last two modes, especially the low power one, are usually impulsive, in order to limit the total energy consumption of the devices.

To deliver as much power to the IMDs as possible, more than one energy source can be considered, as seen in Sec. 1.1, overcoming the limitations presented by a single-approach powered structure. In particular, combining a fully autonomous source capable of low output power with a "high" output power source but dependent on a remote supply. This, can lead to different advantages:

— Covering the sleeping and low power modes with the autonomous source;
— Covering the energy-intensive high power mode with the remote power supply;
— Securing the device operability in case of failure of the wireless link;
— Providing a communication link between the implant and the outside of the body;
— Providing high and low power levels, according to the demands.

In particular, the last point evidences the *double-operating-mode-implant*. In

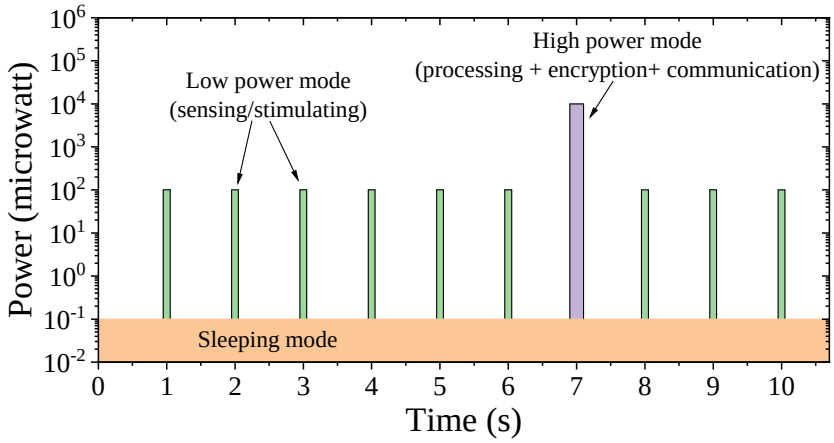


**Figure 3.1** – The two different powering levels of the proposed hybrid-powered IMD.

fact, the power demanding for sensing or stimulating is nowadays low enough (in the order of hundreds of microwatts) to be performed by an independent powering approach. On the other hand, the power needed to process the information and to deliver it to the outside of the body is higher (e.g. tens of milliwatts). Therefore a remote powering approach, that includes also a communication link, is needed.

After having considered different powering techniques, Biofuel cell (BFC) and near-field Magnetically Coupled Resonant (MCR) Wireless Power Transfer (WPT) were selected. The first is capable to deliver the demanded power in a total independent mode, without needing for instance high thermal gradients or movement, since the glucose and oxygen in the body are always available and abundant enough. Moreover, the BFC electrodes can be shaped in any conductive form and geometry. On the other hand, MCR-WPT was chosen since it can insure high Power Transfer Efficiency (PTE).

Therefore, this part of the PhD work was dedicated to the design of an hybrid-powered implantable sensor: this device harvest the energy from the glucose and the oxygen present is the body, by means of a BFC, and wirelessly, by MCR-WPT.

Eventually, the device would merge the communication and wireless powering (antenna) and autonomous powering (electrodes) functions by integrating in the same structure the solenoid antenna and the glucose BFC anode and cathode, in a concept coined Biofuel Cell Antenna (BCA).

The biggest difficulties of this experiment are due to the design and the development of the coils that will be placed inside the tissues as well as the development of the measurement setup. Many challenges are raised by the operation of the BCA, and will be identified in Sec. 3.2. Additional challenges emerging from the hybrid operation measurement call for new measurement tools and techniques, at the interface of the electrochemical and electromagnetic community (Sec. 3.3). The full multidisciplinary demonstration will be presented in Sec. 3.4. The further section will explore possible improvements of the WPT link by engineering the byproduct electrical field, by pushing away the tissues from the Receiver (RX) coil (Sec. 3.5).

## 3.2 Experiment constraints

The challenges introduced by the high multi-disciplinary operation can be sorted in two fields, respectively related to energy transformation and the communication.

### 3.2.1 Electrochemical constraints

The electrochemical reaction of the BFCs (oxidation of the glucose and the reduction of molecular oxygen to water) implies challenges in the electrochemical operation of the two electrodes/antennas, one coated with glucose-selective and the other with oxygen-selective enzymes that oxydize the first and reduce the latter.

First, only gold can be used as metal, the presence of other metals stops the proper functioning of the process. Therefore, the coils must be constructed using gold wires and no soldering is allowed. If any other metal has to be involved, it should be encapsulated into silicone-like material, to avoid contamination.

The enzymes used to perform the reaction are fragile with respect to temperature and mechanical stress. So the coating has to be the last processing step, after having shaped the coils and assembled the structure.

Special attention has to be also dedicated to the design of the measurements tools, in order to retrieve the signal generated by the BFC. Any DC short circuit between the anode and the cathode shall be avoided and the external connectors must be waterproofed, to insure operation inside aqueous environment.

### 3.2.2 Electromagnetic constraints

The main Electromagnetic (EM) constraints are due to complex dielectric medium where the devices are placed: the body tissue. Since this medium has normally high water concentration, it presents high dielectric constant and also dielectric losses at microwave frequencies [78]. Therefore, to prove the BCA concept, a worst-case scenario Phosphate-Buffered Saline (PBS) solution was selected, as explained in the next sections.

To confine the electric field away from the tissues, an external capacitor can be mounted to form a resonant LC tank with the coil.

To perform the measurements, a Radio Frequency (RF) connection is required. Since open structures, e.g. microstrips or coplanar waveguides, cannot be used due to the high dielectric constant and losses of the medium, a closed structure is required. These structures allow electric field confinement and make the characteristic impedance of the implant independent from the changes of dielectric characteristics of the medium. This transmission line has to be designed to allow the mechanical insertion of the coils without soldering and avoiding any contamination of the gold. In the next section a structure is proposed.

Finally, in IMD, the coil/antenna is often coated using a biocompatible insulation, that also stabilizes the dielectric characteristic in the neighborhood of the antenna, avoiding the presence of the lossy medium directly in contact with the metal parts. However, since in this work the antennas are used also as BFC electrodes, no coating is permitted. Therefore, a lower quality factor shall be expected,

| Electrochemical constraints / Electromagnetic constraints | Operation in tissue/ Phosfate Buffered Saline solution | Avoiding metal contamination | Avoiding enzyme damages | Avoiding A-K electrical shortcircuit |
|---|---|---|---|---|
| EM field generation | Tissue losses at RF frequencies<br>Magnetic field coupling | The reaction alllows gold only<br>Use gold to fabricate the antennas/coils | Enzymes are very fragile with respect to temperature and mechanical strees<br>Metal of the antenna should be shaped before being coated with enzymes | Use of DC block capacitor to connect the electrodes to RF or implement 2 different antennas. |
| Connection to external waveguide | Excitation field leackage<br>a) Conception of a waveguide isolated from the surrounding environment<br>b) Waterproofing the waveguide | Any metal contamination can inhibit the reaction<br>a) Avoid soldering<br>b) Coat any other metal with polymer | Enzymes are very fragile with respect to temperature and mechanical strees<br>a) RF connection before enzyme coating<br>b) Keep low temperature before implantation | ------- |
| Avoiding dielectric losses | Electrodes must be in touch with the tissue (no coating is allowed)<br>a) Use of solenoid topology that limits the straight of the E field<br>b) Antenna very close to the RF exitation | ------- | ------- | ------- |
| High quality factor | Presence of the tissue where the E field is maximum<br>a) Use of an external capacitor<br>b) E field confinement | The capacitor can be soldered in the waveguide | ------- | ------- |

**Figure 3.2** – The experiment constraints

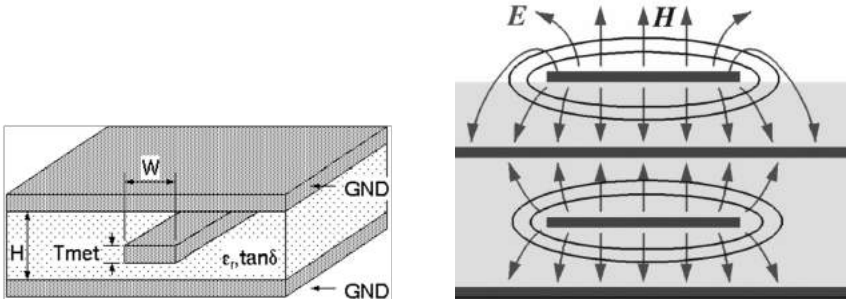


**Figure 3.3** – The stripline transmission line: main parameters (a) and field distribution comparison between stripline and microstrip transmission line (b).

decreasing the performances of the communication system.

Fig. 3.2 shows a table that summarizes all the main constraints of the BFC antenna concept. In red the problems are evidenced while in green a possible solution is indicated.

## 3.3 The proposed stripline structure

A novel transmission line structure is necessary to:

— confine the excitation field inside the structure, not in the PBS solution;
— minimize the reflections due to the transition between the coaxial cable and the proposed structure;
— allow the placement of the golden coil without soldering.

The first requirement allows the placement of the structure inside the solution, and make it independent from the characteristics of the medium. The second is required to insure the absence of any electric discontinuity before the coil, i.e. the structure must have a characteristic impedance of 50 Ω. Finally, the last feature is due to the constraints already explained in section 3.2.

The structure that best suits these requirements turned out to be the stripline transmission line. This is constituted by one metal strip sandwiched between two parallel ground planes. Moreover, the strip is insulated using a dielectric material. Fig. 3.3a shows the main parameters of this kind of transmission line.

The stripline supports the TEM mode and, if the width of the two ground planes is greater than about five times the strip width, the field is confined inside the structure. Fig. 3.3b shows the field distribution of this kind of structure, with a comparison with the microstrip structure. The figure evidences the isolation of the field from the surrounding medium.

Two different versions of the stripline were designed, fabricated and used to characterize the structures presented in the next sections. The first version was designed using 0.8 mm FR4 ($\epsilon_r = 4.5, \tan\delta = 0.018$) as substrate. To further limit the losses introduced by the transmission line, a second version of the structure was dimensioned using 0.51 mm thick Rogers RT/Duroid 5880 ($\epsilon_r = 2.20$, $\tan\delta =$

**Table 3.1** – The resulting dimensions of the stripline, the size names refer to Fig. 3.3a.

| Substrate | H (mm) | W (mm) | Tmet ($\mu$m) |
|---|---|---|---|
| FR4 | 1.6 | 0.65 | 35 |
| 5880 | 1.02 | 0.8 | 17.5 |

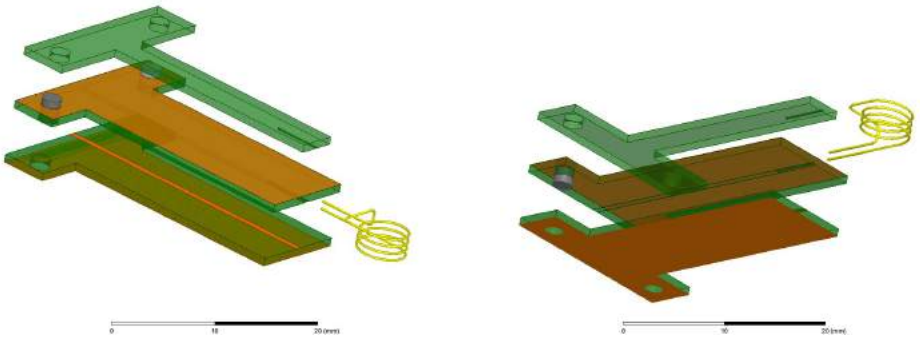

**(a)** **(b)**

**Figure 3.4** – The designed structure, exploded view: top wiew (a) bottom view (b).

0.0004). The structures were dimensioned using the LineCalc tool of the Advanced Design System (Keysight) software and simulations were performed using ADS, Momentum and HFSS in order to validate the model. Tab. 3.1 shows the final parameters of the designed transmission lines.

### 3.3.1 Design of the transmission line

The structure of the stripline presented in the last section was designed, in order to satisfy the requirement and also to make possible its construction. After an attempt with a 1.5 mm thick FR4 structure, the first selected substrate, as introduced earlier, was a 0.8 mm board of the same material, in order to better confine the field. To allow an easy construction and an optimum tightness of the coil, it was decided to use three different layers of FR4. Fig. 3.4 shows the final sketch of the transmission line with a gold coil, in an exploded view. The main parts that constitute the structure are three, as follows. The lowest one is a simple microstrip structure including the strip, having the dimensions of Tab. 3.1. The middle one is constituted by a simple substrate and the upper Ground Plane, in order to complete the structure. Finally, the third layer holds tight the coil to the structure upper Ground Plane. The width and the length of the structure were set equal to 10 mm, more than five time the strip width, and 30 mm respectively, in order to allow an easy immersion of the coil in the PBS solution.

As the figure shows, two screws were included to align and tighten the structure, the second and third layers were machined to allow the lodgement of the coil and the strip without air gaps. Finally, the top layer was designed narrower than the

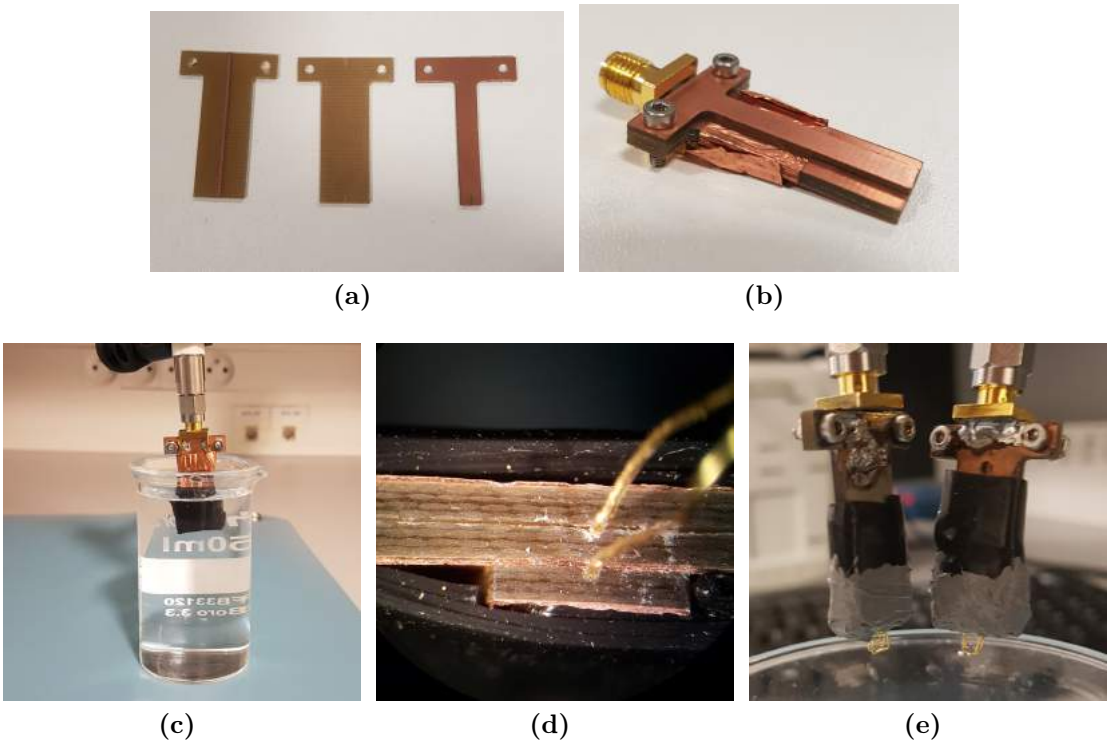

**Figure 3.5** – The built prototype: The different parts (a) and the prototype assembled (b), the measurement in buffer (c), the small apertures due to the presence of the gold wire (c), and the coil coated with the silicone rubber (e).

other two, in order to stick a copper tape shorting the two ground planes.

The structure was simulated in different situations and then built.

### 3.3.2 Mechanical problems encountered and measurements performed

**Construction limitations** The simulated structure was built to verify its characteristics and perform the measurements. Figs. 3.5a and 3.5b show the different parts of the constructed prototype and the assembled structure. In order to allow the connection to the Vector Network Analyzer (VNA), lodgements for an SMA connector were cut, in addition to the designed model. Unfortunately, it was not possible to cut the depression of the second layer, designed to allow the insertion of the strip to insure a perfect seal, due to machinery limitations.

**Measurements** In continuity with the simulations, measurements were performed in order to compare the behaviour of the structure in air and when immersed in PBS solution. In order to avoid solution infiltrations between the layers, the assembled structure was coated with silicon waterproof tape.

The coaxial cable of Port 1 of the VNA was connected to the structure by means of the SMA connector and the S11 scattering parameter was observed. Fig. 3.5c shows the measurement setup for the measurement in water.

To avoid infiltration within the multilayer transmission line, due to the imperfect layers alignment (Fig. 3.5d), the far end of the structure (where the coil is placed), was coated with a silicone rubber specifically designed for electronics (Dow Corning 3145 RTV MIL-A46146), as Fig. 3.5e shows. By adding this silicone layer, the structure is made completely waterproof, ensuring the reproducibility of the experiments.

### 3.3.3 Conclusion

A water-proof transmission line that can be used to perform the experiment has been designed, developed and validated in PBS solution. The addition of a silicone rubber allows the structure to be completely isolated from the outside liquid medium. Although all the validation process has been performed taking into account the FR4 structure, it has been used only for the proof of concept presented in the next section. The more efficient 5880 structure has been used for all other measurements presented later in this chapter.

## 3.4 Proof of concept of the experiment

After having designed the transmission line, allowing the placement of the coil, and taking into account the constraints introduced in section 3.2, a proof of concept of the BFC antenna experiment was ideated. In this section the designed experiment is presented, as well as the results obtained.

### 3.4.1 Design of the experiment

Fig. 3.6 shows the experimental setup defined to perform the experiment. Two mm-sized coils (1 and 2 in the figure) are immersed in a PBS solution that mimic the inner biological environment. To achieve the fuel cell mission, coil 1 and 2 are also modified with enzymes, to become the Anode (A) and Cathode (K). Two other coils (3 and 4) are magnetically coupled to the two immersed coils, to achieve the inductive link. As the figure shows, in order to minimize the cross-talking between the coils, two different resonant frequencies are selected. Coils 1 and 3 are designed to resonate at $f_1$, and coils 2 and 4 to resonate at $f_2$. The wireless PTE, typical Figure of Merit (FoM) used to characterize a wireless link, is measured by a VNA and the DC power delivered by the BFC is recorded by means of a potentiostat, modelled as a resistance in Fig. 3.6. In order to separate the RF and DC signals, two bias-tee are included in the setup.

The losses introduced in the DC path by a commercial bias tee were measured, in order to verify that no considerably power is lost by this component. By measurements it turned out that the bias-tee introduces a resistance $R_{bt} = 0.36\Omega$, negligible if compared to the typical load of a BFC. Therefore, this component can be correctly used to perform the experiment.

To retrieve the signal from the coils, the specially designed stripline (Fig. 3.5e) was used.

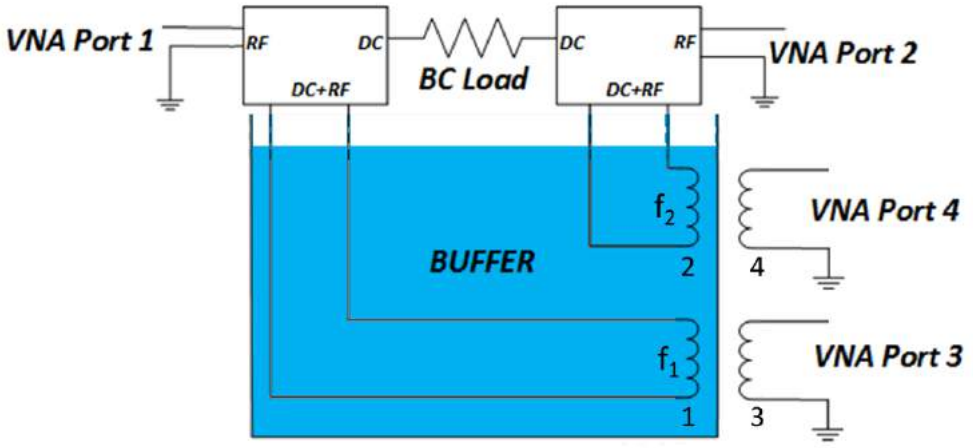


**Figure 3.6** – The setup for the BCA experiment.

### Design of the coils

The stripline presented in the last section was modified in order to allow the placement of a physical capacitance in parallel with the coil. In fact, if the electric field will be confined inside a structure, e.g. a capacitor, the structure is pretended to be less affected by the dielectric losses present in water. By adding a capacitors is parallel with the coil, an LC tank circuit is formed, and its resonance frequency, i.e. the operation frequency of the WPT link, is given by:

$$f_0 = \frac{1}{2\pi\sqrt{LC}}, \tag{3.1}$$

where $L$ is coil self inductance and $C$ is the capacitance of the physical capacitor.

In order to insert a capacitor in parallel with the coils, a hole was made in the upper part of the stripline and an SMD capacitor was soldered vertically on the strip (Fig. 3.7a), and on the upper ground plane. In order to mimic an harmonic RFID system [166], the two frequencies were chosen one the double of the other. Therefore, when the system will be implemented, the Transmitter (TX) will send the power at $f_1 = f_0$ and the RX will send back the information collected by the implant at $f_2 = 2f_0$. For this work, the two selected frequencies were $f_1 = 141$ MHz and $f_2 \approx 2f_1 = 271$ MHz.

Both coils had a diameter of 3 mm and 2 turns. 250 µm thick gold wire was use to build the solenoids. In order to tune the resonance frequency, by using Eq. 3.1, two different capacitance were selected: $C_1 = 47$ pF ($f_1$) and $C_2 = 18$ pF ($f_2$). After soldering the capacitance, the coils were mounted without soldering, to avoid any metal contamination, and the silicone tape and rubber were applied, as Fig. 3.5e shows, in order to waterproof the structure.

### Enzymes modification

After constructing the RX systems, the two gold coils were modified with enzymes, to implement the BFC. First the coils were cleaned in piranha solution, in

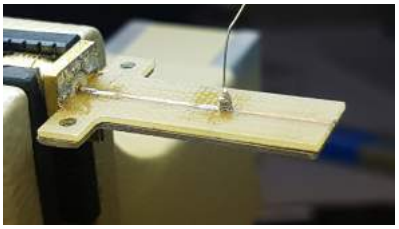

**(a)**

**(b)**

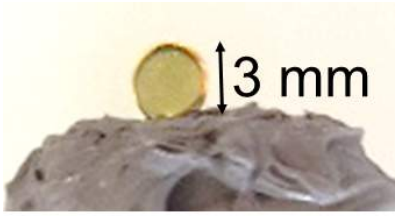


**(c)**

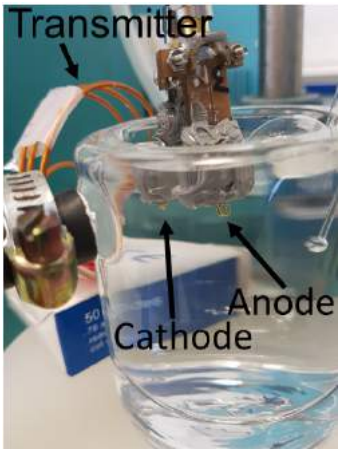


**(d)**

**Figure 3.7** – The biofuel cell antenna experiment: The soldered capacitance (a), the deposition of the enzyme on the anode (b), the anode with the deposited enzyme before the drying process (c) and the measurement setup (d).

order to avoid any contamination of the structure. Then the coils were modified, to form the anode and cathode of the cell.

Glucose Oxidase (GOx)) enzyme was used to modify the anode, and Bilirubin Oxydase (BOD) enzyme for the cathode. The coil resonating at $f_2$ was chosen as anode and the one resonating at $f_1$ as cathode. Fig. 3.7b shows the deposition of the GOx on the anode and in Fig. 3.7c the deposited enzyme on the 3-mm anode is evidenced. The same process has been also performed on the cathode. The electrodes were then dried for eighteen hours at 4 °C.

#### Measurement setup

After drying, the two coils/electrodes were immersed inside the PBS to be characterized in both the EM and electrochemical behaviors. 20 mM of NaPi and 140 mM NaCl were added to the solution and, in order to mimic the body temperature, the PBS temperature was set at 37 °C.

To characterize the electrodes, Argon was inserted in the PBS in order to avoid the electrochemical reaction. After this, 40 mM of glucose were added and the solution was saturated with oxygen, to start the reaction.

Regarding the wireless communication, the PTE, defined as:

$$PTE = \frac{P_r}{P_t} = \frac{|S_{21}|^2}{1 - |S_{11}|^2}, \tag{3.2}$$

where $P_r$ and $P_t$ are, respectively, the received and transmitted power, and $S_{xy}$ are the scattering parameters measured with the VNA, was measured. This aims to discard the mismatch between the VNA port and the small coils, not object of this study.

The two coils placed in air were implemented as self-resonant coils excited by a loop. These two structures were designed to resonate at $f_1$ and $f_2$, to match the two resonances of the coils in PBS solution. Fig. 3.7c shows the measurement setup. Since a 2-port VNA was used, the links at the two different frequencies were tested separately.

### 3.4.2 Results

In this section the results of the experiment are presented. The first part shows the results of the BFC and the second the PTE of the link.

#### Electrochemical results

Fig. 3.8a shows the obtained I-V curve in Argon. The electrodes were tested separately to verify the good deposition of the enzymes. The red curve represents the anode and the black curve the cathode. The figure shows the presence of two negative peaks, at about -0.08 V for the anode and 0.3 V for the cathode, sign of the presence of the enzymes on the electrodes.

As explained in the last section, the next step was to test the two electrodes separately, in presence of oxygen and glucose (Fig. 3.8b). The red curve (anode) and the black curve (cathode) show the presence of the glucose oxidation and the

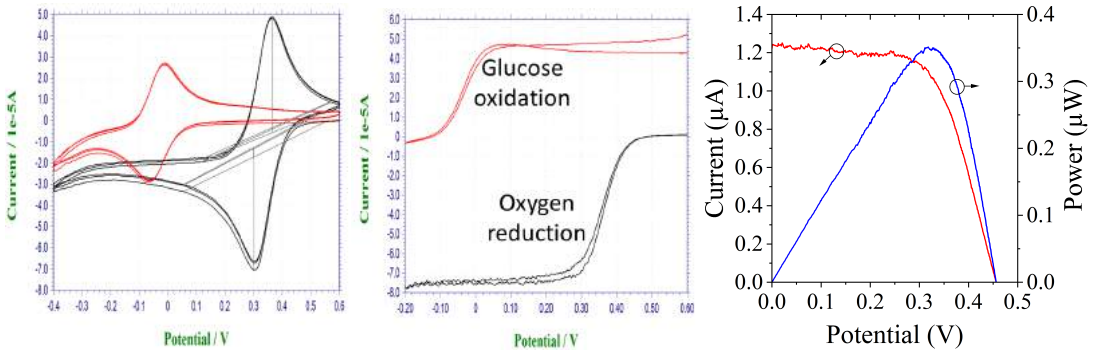


(a) (b) (c)

**Figure 3.8** – The electrochemical results: The electrode characterizations in argon (a) and in presence of glucose and oxygen (b), the red curve represents the anode and the black curve the cathode; and the power delivered from the BFC (c)

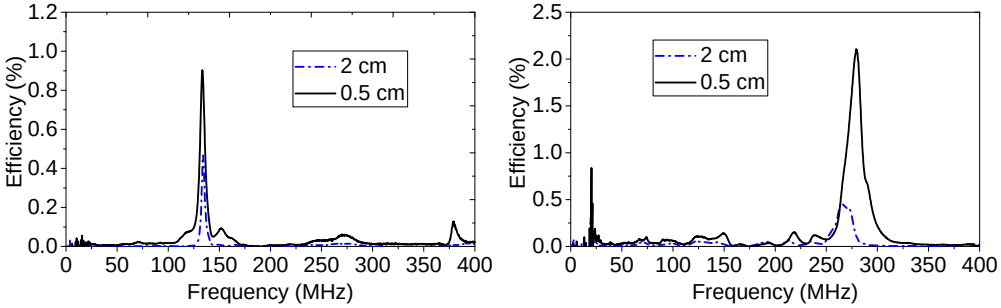


(a) (b)

**Figure 3.9** – The PTE with respect to frequency: Coil 1 (cathode) (a) and Coil 2 (anode) (b).

oxygen reduction, as indicated in the figure. Therefore, the presence of the reaction was confirmed.

Finally, the two electrodes were connected together, forming the BFC, and the power delivered, as a function of the voltage, was recorded, as Fig. 3.8c shows. The BFC was delivering power, confirming once again the presence of the reaction. Fig. 3.8c shows also that, as expected, the BFC acts as a current generator. During the experiment, it was delivering a current of about 1.2 µA.

The resulting power, having a peak of 0.35 µW was poor, but the optimization of it was not the goal of this study. Moreover, as Fig. 3.7b shows, the enzymes were deposited only on the internal part of the coil. Therefore, not all the surface of the electrode was modified, limiting the emitted power.

### Electromagnetic results

While the BFC activity was recorded, the WPT, described by Eq. (3.2), was monitored by using the VNA. The two coils in air were placed in front of the two electrodes and the scattering parameters were registered for two different TX/RX distances: 2 cm and 0.5 cm.

Fig. 3.9a shows the recorded efficiency for the coil 1 ($f_1$) and Fig. 3.9b the one for coil 2 ($f_2$). The maximum recorded efficiency was 0.95% and 2.1% respectively. As expected, the efficiency drops dramatically with the distance, resulting in just 0.47% and 0.45% at 2 cm of separation. The efficiency of the coil 2 was about two times higher than the coil 1 at 0.5 cm distance, while the two coils showed comparable efficiency at 2 cm.

The resulting sensitivity is lower than the typical value present in literature for similar structures [111]. This mainly because, as explained in section 3.2, no coating of the coil is allowed. Therefore, the structure is highly impacted by the complex liquid medium, that is a worst case scenario compared, for instance, to muscle tissue. But, as for the BFC part, the goal of this experiment was just the proof of the concept and not the optimization of the link.

### 3.4.3 Conclusion

The concept of a structure that uses two solenoidal shape gold wires both as BFC electrodes and coils for inductive resonant coupling was proven. These structures were modified with enzymes and immersed in a physiological solutions, that mimics the body environment. The two capabilities of the coils/electrodes were monitored simultaneously. The power delivered by the biofuel has reached a peak of 0.35 µW, while a PTE in the order of 1% was recorded for both coils, at a distance of 5 mm.

These values were limited by the design constraints, that have to be respected to successfully perform the experiment. Further study has to be done to optimize the deposition of the enzymes, to use all the surface of the electrodes, and to achieve higher efficiency between the TX, placed in air, and the implanted RX.

## 3.5 High-Q coil structure

In continuity with the results just showed, a novel 2-coil implantable structure is presented, in order to enhance the quality factor of the resonator and therefore to increase the PTE.

### 3.5.1 Background

In typical MCR-WPT, as the one presented in the last section, two LC tanks resonating at the same frequency are coupled to transfer energy. The Power Transfer Efficiency (PTE) can be enhanced using self-resonating coils for the TX and RX called a "4-coil system" [108, 98]. Fig. 3.10a shows the equivalent circuit for the 2-coil and 4-coil system.

A MCR-WPT link is primary dependent on the Q factor of the implanted magnetic resonator, since the transmitting bears much less design constraints.

Therefore, this work focuses on the design of an implantable resonator with implanted design constraints (dimensions, complex surrounding environment...). Major attention is given to the maximization of the quality factor of the receiving coil for the key role it plays in the PTE.

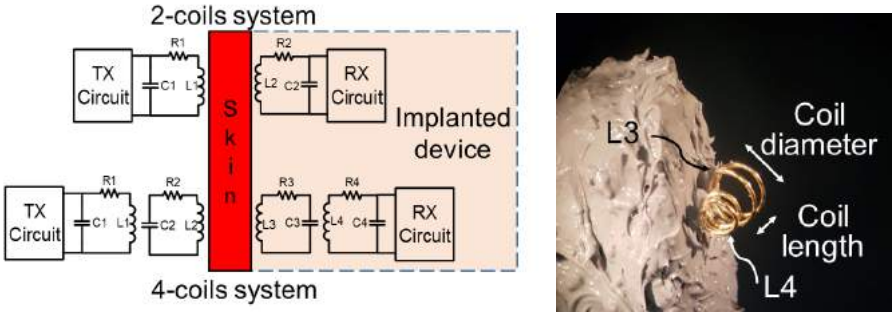


**(a)** **(b)**

**Figure 3.10** – MCR-WPT link: Equivalent circuit for 2-coil and 4-coil (self-resonating TX and RX configurations (a) and a photograph of the 2-coil RX (b).

### 3.5.2 Design of the receiver devices

#### Power transfer efficiency

The PTE can be expressed as [98]:

$$PTE \cong \frac{k_{ij}^2 Q_i Q_j}{1 + k_{ij}^2 Q_i Q_j}, \tag{3.3}$$

where $k_{ij}$ is the coupling factor between coil $i$ and $j$, and $Q_i$ and $Q_j$ are the quality factors of the respective coils. With reference to Fig. 3.10b, for the 2-coil system i=1, j=2, and i=2, j=3 with respect to the 4-coil one (although the equation is strictly true in the 2-coil case and an approximation in the 4-coil one).

#### Receiver implementation

To limit the impact of the implantation, and thus the inflammatory response of the tissues, the receiving coil has to be typically not larger than a sphere of 3 mm diameter [83]. Based on those specifications, and in continuity with the experiment presented in the last section, a solenoidal shape of 3 mm is chosen with 2 windings (note that operation frequency was not considered as a constraint in this study). Pure-gold wire of section of 250 µm has been used to build a single coil receiver (RX1) and a self-resonating coil-loaded loop receiver (RX2). The latter is formed by two coils: a self-resonating coil structure (secondary tank), having the same dimension of RX1, and a second coil (load tank) connected to the VNA. Moreover, physical SMD capacitors have been used to further confine the electric field away from the surrounding living tissues, in continuity with the last section. Details of the RXs are given in Tab. 3.2, while a photograph of the 2-coil receiver (bare gold) is shown in Fig. 3.10b.

#### Measurement setup

For the 1-coil receiver, the same transmission line presented in section 3.3 was used. Regarding the 4-coil structure, a new transmission line was designed and developed, in order to allow the lodgement of the two coils and the two capacitors.

**Table 3.2** – The dimensions of the developed structures. D is the coil diameter, N the number of turns, L the coil length and C the capacitance value.

| | Secondary Tank | | | | Load Tank | | | |
|---|---|---|---|---|---|---|---|---|
| | Coil | | | Capacitance | Coil | | | Capacitance |
| | D (mm) | N | L (mm) | C (pF) | D (mm) | N | L (mm) | C (pF) |
| RX1 | 3 | 2 | 0.9 | 47 | - | - | - | - |
| RX2 | 3 | 2 | 0.9 | 47 | 2 | 2 | 0.9 | 18 |

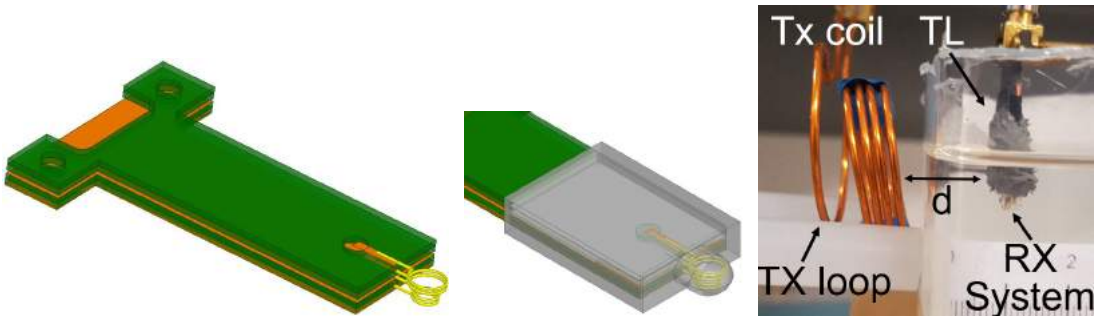


**(a)** **(b)** **(c)**

**Figure 3.11** – The 2-coil system: 3D simulation model without (a) and with (b) the silicone coating; as well as the setup used to measure the efficiency.

Fig. 3.11a shows the rendering of the novel structure, including the two coils. Two layers were added to the previous transmission line, allowing the placement of the second coil. Moreover, a hole was drilled in the last dielectric layer, in order to include the SMD capacitor in the design. Fig. 3.11b shows the 3D model with and without the silicone ($\epsilon_r = 2.83$, $\tan\delta = 0.0001$) coating, used to perform the simulation of the developed structure.

Reflection and transmission measurements were performed using a Keysight E5061B Vector Network Analyser, calibrated using a custom SOL calibration kit.

The devices were tested in two different environments: in air and inside the PBS solution (worst case scenario in term of permittivity and dielectric losses), in continuity with the previous section.

The quality factors of the structures were extrapolated, directly on the VNA, using the following procedure: (i) the S11 measurement was observed on the Smith chart in order to visualize the characteristic circle formed by a resonator in the neighborhood of the resonance frequency (Fig. 3.12, left side). (ii) A phase offset was inserted in order to bring the circle in the *detuned short position* (3.12, right side). The correct phase offset amount allows to model the measured structure as an ideal shunt RLC circuit. Therefore, the quality factors can be calculated by: (iii) visualizing the magnitude of the input impedance. (iv) Using the automatic marker function (*bandwidth*) of the VNA, the value of the quality factor was extrapolated,

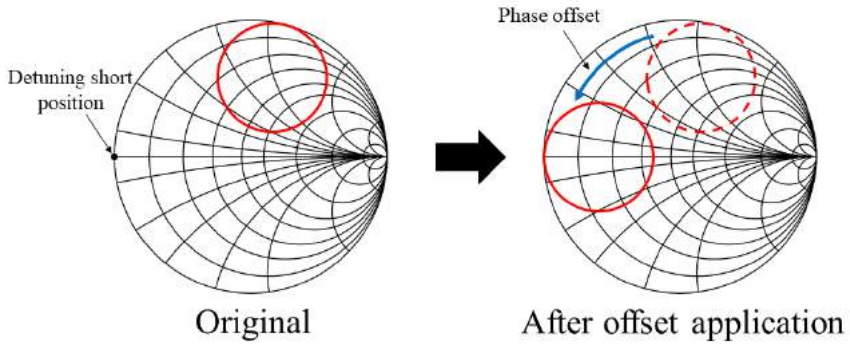


**Figure 3.12** – The effect of the phase offset application in order to correctly measure the Q factor of the structures.

using the following:

$$Q = \frac{f_0}{\Delta f_{-3dB}}, \tag{3.4}$$

where $f_0$ is the resonance frequency and $\Delta f_{-3dB}$ is the -3 dB bandwidth of input impedance magnitude.

Regarding the measurements in transmission, a self resonating coil-loaded loop TX system was used, consisting in an exciting loop and a self-resonant coil. The resonant frequency of the latter was tuned by acting on the pitch between the turns. The distance between coil and the loop was optimized to insure good impedance matching to the 50 Ω impedance of the VNA port. All the measurement were performed with the same TX resonating coils in order to allow fair comparison. Fig. 3.11c shows the measurement setup used for the transmission measurements inside the solution.

### 3.5.3 Results

Measurements were performed both in air and into the saline solution. The quality factor of the self-resonating (2-coil) receiver is given for two configurations: with and without silicone encapsulation. The first one allows enzyme coating. The second one enables comparison with the literature of implantable resonant wireless link [112].

The comparison between the simulated and measured reflection coefficient for RX2, having silicon encapsulation (Fig. 3.11b), in air and when immersed in the solution [1] is showed in Fig. 3.13a. The two curves are comparable. A shift of the resonance frequency towards higher values, of about 5 MHz, is registered between simulation and measurements. Moreover, a poorer matching is observed in measurement, as compared to simulations. This is due to some minor differences between the (ideally) simulated and the (real) measured structures, occurred during the building process, e.g. coils not perfectly rounds, different coil pitches and different distance between the two coils from simulations to measurements. As expected, the presence of the coating isolates well the coils from the lossy medium.

1. The solution was modelled as body fluid, having a frequency dependent behaviour.

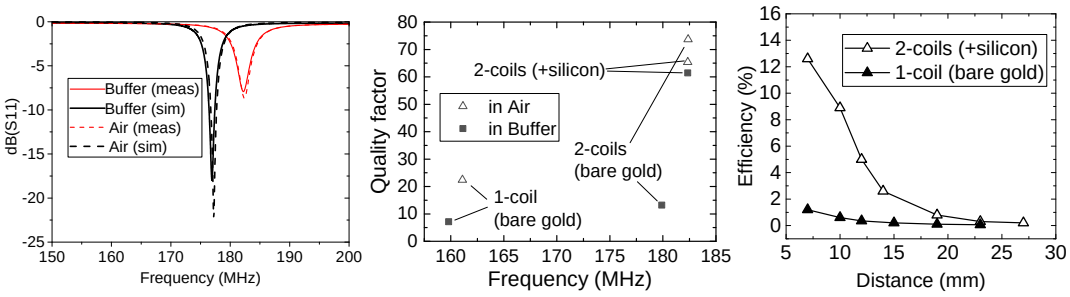


**(a)** **(b)** **(c)**

**Figure 3.13** – The results obtained: Comparison between the $S_{11}$ resulting from simulation and measurements for RX2 considering the silicone coating (a) the measured quality factors (b) and the registered PTE in PBS (c).

Therefore, the curves in air and in the solution are almost coincident, demonstrating the critical importance of the immediate surrounding of the coil.

Fig. 3.13b reports the quality factor of the measured structures. In air, as expected, the 2-coil configuration boosts the Q factor of the structure, resulting in a large improvement from 22 to 74 (when uncoated), and to 65 (when silicon-coated). The decrease of the Q factor after coating is attributed to the silicon dielectric losses.

When inserted in the water-based solution, the resonators exposed to dielectric losses become greatly affected. It is seen that Q factors of the uncoated structures radically drop from 22 to 7 for RX1 (loss of 68.2%) and from 74 to 13 for RX2 (loss of 82.4%). This is mainly due to the electric volumetric energy density located in the parasitic capacitance of the coil, i.e. between the windings. As a matter of fact, RX2 is more sensitive to the change of medium, due to the presence of two coils and thus of higher electric volumetric energy density.

Moreover, when dipped in the solution, all the uncoated structures resonate at lower frequency, due to the dispersion effect of the medium.

Regarding the coated RX2, thanks to the presence of the silicone, it is only slightly sensitive to the change of outer medium. Therefore the quality factor in buffer has evidenced a decrease of 6.1%, due to the residual presence of electric field power density outside the silicon. Also the resonant frequency has almost no shift.

For the sake of comparison, Tab. 3.3 shows the Q factors achieved by similar implants present in the literature. In order to compare different systems having different coil dimensions, a FoM is introduced, defined as:

$$FoM = \frac{Q}{A^{1/2}}, \tag{3.5}$$

where Q is the quality factors and A the area of the section of the secondary coil. As reported in Tab. 3.3, the proposed structure shows the best performances both in air and in buffer.

Finally, the receiving coil has been tested in a full transmission setup (Fig. 3.11c) including a 2-coil resonator as outside TX. The parameter taken into account

**Table 3.3** – The comparison between this work and 4-coil structures present in the literature.

| | Medium | Q factor | Area ($mm^2$) | FoM 1/mm |
|---|---|---|---|---|
| This work | Air | 65.4 | 7 | 24.7 |
| | PBS | 61.4 | 7 | 23.2 |
| [108] | Air | 24 | 25 | 4.8 |
| | Muscle | 17 | 25 | 3.4 |
| [98] | Air | 148 | 314.15 | 8.35 |
| [167] | Air | 11.6 | 4.36 | 5.27 |
| [105] | Air | 152 | 78.5 | 17.15 |
| [168] | Air | 109 | 314.15 | 6.15 |

was the PTE, calculated implementing Eq. 3.2. To perform typical end-user application scenario measurements, the separation between the TX and the saline solution was fixed at 3 mm and the RX device was moved in order to increase the distance (similarly to Fig. 3.11).

Fig. 3.13c shows the efficiency behavior as a function of the distance between the TX and the RX. As expected from Eq. 3.3, the PTE dramatically increases when the 2-coil system and the coating is used. Please note that the TX used for these measurements was not optimized, since this work focuses on the RX side only of the MCR-WPT implantable system. Further improvement of the PTE can be achieved by increasing the parameters of the transmitting side.

### 3.5.4 Conclusion

An original implantable self-resonating coil-loaded loop (2-coil) for wireless power delivery is proposed. Since this structure consists in two separate conductors, it could directly be used to develop the two electrodes of the BFC, without needing two separate resonators that work at two different frequencies.

The quality factor of the structure was raised, in order to increase the WPT efficiency. This was achieved by coating the structure, therefore the BFC cannot be implemented. In the next chapter a possible solution is presented.

## 3.6 Conclusion of Chapter 3

This chapter has focused on the development of an implantable, wireless, mm-sized devices that harvest the power from glucose and oxygen, naturally present is human tissues, and from an EM source placed outside the body. This hybrid-powered device insures continuity of operation even if an external source is not connected/temporary faulty. Moreover, when the TX is placed, communication can be performed to configure the implant or to retrieve the collected data.

After having defined the constraints and having designed a custom waveguide, the concept of a BCA was proven. Due to the trades-off implemented to satisfy both the electrochemical and EM operation, the prototype is as efficient as state-of-the-art BFC or WPT devices, but it proves the feasibility of an hybrid-powered device capable of harvesting different types of energy in a single object, providing thus a large improvement in implant volume.

Furthermore, in order to improve the design performances, a high-Q 2-coil mm-sized resonator has been proposed. This structure has a Q-factor of 61.4 when placed in a PBS solution, improving the performances with respect to similar structures present in the literature. Unfortunately, to achieve this result, the device has been coated with a silicon rubber, not permitting the development of a BFC.

# Chapter 4

# The Threaded-Furrow Geometry

## 4.1 Introduction

This chapter presents all the expects taken into account to improve the wireless Power Transfer Efficiency (PTE) between an implantable structure and a transmitter placed in the outside of the body. The implant receiving coil is used both as antenna for Wireless Power Transfer (WPT) and electrode.

As presented in last section, the PTE of the Biofuel Cell Antenna (BCA) is degraded by using it directly in contact with the high-dielectric and lossy medium, decreasing the performances of the device. It was clearly seen in Sec 3.5, that a possible coating of the electrodes could boost the Q factor of the presented structure from 13 to 61.4.

As a matter of fact, the complete coating is not possible if the coils are used also as electrodes, therefore an alternative has to be found. The critical location of the lossy tissue is where the electric field is maximum, i.e. inside the structure and between the turns of the solenoidal structure. One possible solution is to insert a dielectric object where the electric field reaches the maximum, in order to avoid the main penetration of E field into the tissues.

The next sections will present all the work done to this point. Sec. 4.2 presents an innovative proposed structure, with theoretical bases, simulation and measurements. Sec. 4.3 proposes a design optimization taking into account the whole volume of the implant. The performed measurements on this structure and the results achieved are presented in Sec. 4.4. A first validation of a possible application, beside the BCA, an impedance monitoring system, has been performed and it is presented in Sec. 4.5.

## 4.2 The proposed structure

In this section the proposed structure is presented as well as some theoretical consideration about its quality factor.

### 4.2.1 The role of the quality factor

In the case of a WPT link with one Receiver (RX) and one Transmitter (TX) coil, the PTE, as shown in Eq. (3.3), can be expressed as [98]:

$$PTE = \frac{k_{12}^2 Q_1 Q_2}{1 + k_{12}^2 Q_1 Q_2}, \tag{4.1}$$

where $k_{12}$ is the coupling factor between the TX and RX coils, $Q_1$ and $Q_2$ are the quality factors of the respective coils. As shown in Sec. 1.2, the coupling factor, proportional to the magnetic field generated by the transmitter, is highly affected by the TX-RX distance, while the implant Q factor is independent from it.

Considering a given implantation depth and external Q coil, as Eq. (4.1) shows, the quality factor of the RX side plays a key role, and has to be maximized. Unfortunately, the small dimensions allowed to the implant, as well as the presence of the lossy tissue, highly limit this parameter. Especially, when the double capability (antenna+electrode) of the structure is desired.

In classical implantable-WPT systems, the RX coil is used far below its self resonance and a capacitor is connected to it in order to have an LC resonating tank. Since the quality factor of the coil is the limiting factor, it is interesting to show how the tissues can lower it.

Since the inductor works below its self-resonance, the quality factor of a coil can be defined as [113]:

$$Q = 2\pi \frac{Net\,energy\,stored}{Energy\,dissipated\,per\,cycle} = 2\pi \frac{W_m - W_e}{W_{loss}^{1c}}, \tag{4.2}$$

where $W_m$ and $W_e$ are the average stored magnetic and electric energies, and $W_{loss}^{1c}$ is the energy lost in one oscillation cycle. The loss of energy is due to ohmic, radiation and dielectric losses. The latter is critical when the lossy tissues are present, as explained later in this section.

$W_m$ and $W_e$ are given by:

$$W_m = \frac{\mu}{4} \int_V |\overline{H}|^2 \, dV, \tag{4.3}$$

$$W_e = \frac{\epsilon'}{4} \int_V |\overline{E}|^2 \, dV, \tag{4.4}$$

where $\mu$ is the magnetic permeability, $\overline{H}$ is the magnetic field, $\epsilon'$ is the real part of the electric permittivity and $\overline{E}$ is the electric field. Note that, since there are not magnetic losses in tissues and air, $\mu$ is a real quantity and thus no superscript was used. Moreover, the tissues are transparent to the magnetic field ($\mu_r^{tissue} = 1$). Therefore, the magnetic energy stored can be assumed independent to the medium where the antenna is placed, and it only depends on the dimensions and geometry of the coil.

On the other hand, the parasitic capacitance, and thus the electric energy, increases when the coil is placed inside the body, due to the high dielectric permittivity of the tissues at MHz range [78]. Consequently, as Eq. (4.4) shows, the stored electric energy increases, resulting, from Eq. (4.2), in a lower Q.

Since the tissues are lossy, the power dissipated by the latter is:

$$P_\epsilon = \frac{2\pi f_0}{2} \int_V \epsilon'' |\overline{E}|^2 \, dV, \tag{4.5}$$

where $\epsilon''$ is the imaginary part of the electric permittivity. The integral is evaluated over the regions where $\epsilon''$ is non-vanishing, i.e. inside the tissue.

Eq. (4.2) shows that the magnetic energy has to be maximised while the electric energy, always present in a real inductor due to the parasitic capacitance, as to be as limited as possible. Moreover, the presence of the tissue losses increases the dissipated energy, as Eq. (4.5) shows, further lowering the quality factor of the structure.

In order to avoid these unwanted effects due to the presence of the tissues, the implant coil is often coated with some low dielectric, low losses material, e.g. PDMS. Acting like this, the neighbourhood of the structure, where the electric field is maximum, is isolated from the lossy medium, limiting the decrease of the quality factor. In other words, taking into account Eq. (4.3)-(4.5), the magnetic energy is not affected by the presence of the coating, since it is not a magnetic material. Otherwise, the strongest part of the electric field is *confined* outside the tissues (inside the silicone), limiting Eq. (4.4),(4.5), and thus increasing the quality factor of the structure.

### 4.2.2 The Threaded-Furrow dielectric structure

As introduced in Sec. 3.2, in the case where the implant coil is used also as electrode, the contact between the metal part and the tissue has to be kept. Therefore, no complete coating is allowed. If the bare coil is implanted in the body, without any dielectric, the electric stored energy and dielectric losses will increase, resulting, from Eq. (4.2), in a low Q and thus in a lower link efficiency (Eq. (4.1)).

A possible solution is to insert in the design a dielectric structure that will occupy the volume where the electric field is maximum, i.e. inside the coil and between the turns [169], while keeping the contact between the coil and the tissue.

Fig. 4.1a shows the proposed structure. It consists of a dielectric material shaped as a Threaded-Furrow Geometry (TFG), in other words having a *screw* shape, having radius $r_s$ and height $h_s$, that allows the insertion of the coil, of radius and height $r_c$ and $h_c$ respectively (Fig. 4.1b). The coil is also characterised by its number of turns, $N$, its pitch, defined as $p_c = h_c/N$, and the radius of the wire, $r_w$.

Fig. 4.1c shows the resulting electric field map, obtained by simulation, computed on a section through the axis of the coil. As expected, the electric field is concentrated between the turns of the coil. The coated case is also shown as a comparison. As expected, the field is almost completely confined, increasing the performances of the structure. Finally, when the proposed geometry is taken into account, a proportion of the field is confined inside the structure. Therefore, an improvement of the quality factor of the structure is expected.

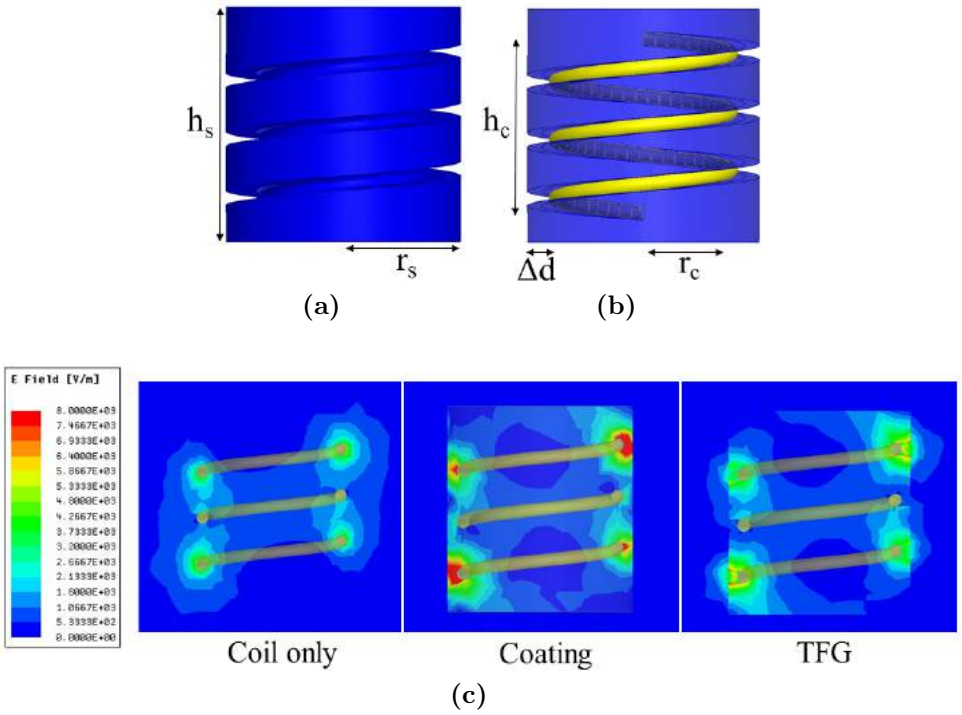


**Figure 4.1** – The proposed dielectric structure: The threaded-furrow dielectric structure (a), the structure with the coil (b) and the simulated electric field in different environments (c).

### 4.2.3 Validation of the structure

#### Simulations

In order to validate the assumptions made in the previous sections, simulations were made to observe the variation of the quality factor in presence of the dielectric geometry and while varying the geometric and dielectric characteristics of the latter. For this series of simulations, the coil was kept constant, having $r_c = 1.5$ mm, $h_c = 3$ mm, $N = 3$ and $r_w = 125\,\mu$m. Also the medium surrounding the structure was kept constant, having $\varepsilon = 75$ and $\sigma = 1.5$ S/m for the all frequency band taken into account. These values were chosen to simulate the presence of a high-dielectric lossy medium, as the human tissues. The dielectric height was also kept constant to $h_s = 4$ mm. Therefore, the TFG exceeded of 0.5 mm on both side of the coil. The coil radius and dielectric constant were swept, keeping the losses of the structure constant: $\tan\delta = 0.001$. In order to compare different dielectric sizes a new parameter is introduced, defined as $\Delta d = r_s - r_c$. Since the coil radius was constant, an increase of $\Delta d$ follows an increase of $r_s$.

Fig. 4.2a shows the results of the simulation while $\Delta d$ and the dielectric constant of the TFG were swept. The quality factor was computed as $Q = Im(Z)/Re(Z)$, where $Z$ is the structure input impedance. As expected, the increase of the dielectric structure radius determines an increase of the quality factor, since more low-lossy material occupy the volume with a non-negligible electric field, i.e. lowering the volumetric losses in the tissue defined in Eq (4.5). Moreover, the increase

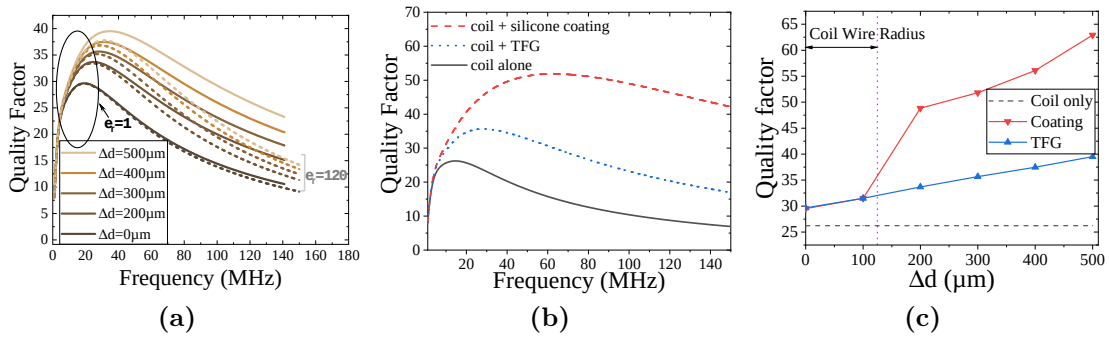


**Figure 4.2** – The simulation results: the quality factor while $\Delta d$ and the dielectric constant of the structure were swept (a), the comparison between coil alone, the TFG and the coated one at $\Delta d = 300\,\mu\text{m}$ (b), and the comparison between the same structures while $\Delta d$ was swept (c).

of the dielectric $\varepsilon_r$ results in an increase of the parasitic capacitance, and thus of the electric energy stored (Eq. (4.4)), resulting in a lower Q. This effect is more important as $r_s$ increases. Therefore, Fig. 4.2a shows that, in order to maximize the performances of the structure, the TFG has to have losses and dielectric constant as low as possible, in continuity with Eq. (4.2)-(4.5).

Fig. 4.2b shows the comparison between the bare coil, the TFG and the coated ones, all having $\Delta d = 300\,\mu\text{m}$, taking into account the best case of Fig. 4.2a, i.e. $\varepsilon_r = 1$ and $\tan\delta = 0.001$ for the proposed geometry and coating. As expected, the quality factor of the structure including the dielectric is placed between the worst case scenario, i.e. no confining structure, and the best one, with the silicone coating. Moreover, the frequency corresponding to the maximum value of the quality factor shifts from lower to higher values, indicating a decrease of the parasitic capacitance as the electric field is less distributed in tissues (confined inside the low-loss dielectric structure).

Fig. 4.2c shows the comparison between the three different structure quality factors, while varying $\Delta d$. For each point the maximum value of Q was computed. The figure confirms the behavior observed in the previous graph: when $\Delta d$ is increased above the wire radius, the coating performances resulted to be the best ones, while also the presence of the TFG increases the performances with respect to the coil alone case. It is interesting to observe the linear behaviour of the TFG curve.

In order to further validate the design and to confirm the assumptions made about the quality factor, Eq. (4.3)-(4.5) were computed in HFSS, taking into account the proposed structure (with $\varepsilon = 1$ and $\tan\delta = 0.001$). The magnetic and electric fields are supposed to be negligible outside the tissue region. In order to compare the structures, the equations were computed at a fixed frequency (25 MHz) for all the structures.

Fig. 4.3a shows the average stored magnetic energy. As expected, since the surrounding tissues and the dielectric material are not sensitive to the magnetic field, the total energy remains constant, and the presence of the geometry does not change the overall value with respect to the coil-only case. The energy inside the

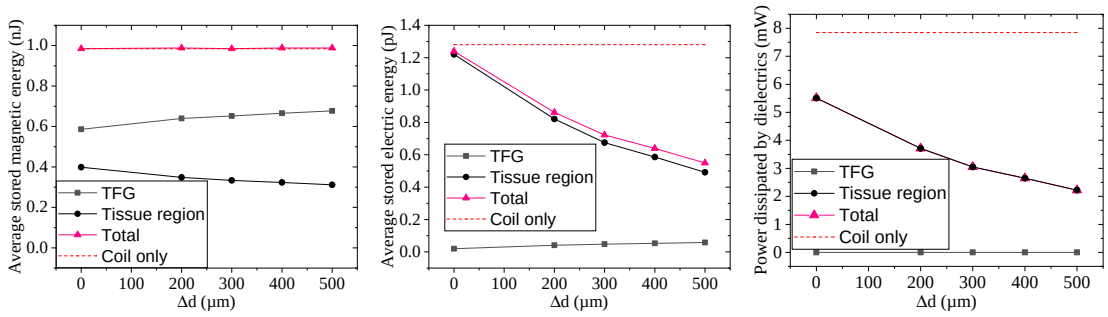


**Figure 4.3** – The simulated energies and power: the average stored magnetic (a) and electric (b) energies, and the power dissipated by dielectrics (c). All the results were computed at 25 MHz, by sweeping $\Delta d$.

dielectric ramps up, as it ramps down in the tissue region, due to the changing of the volume occupied by the two structures while $\Delta d$ increases. The resulting average stored electric energy, described in Eq. (4.4), is shown in Fig. 4.3b. It is seen that, as the low-permittivity dielectric is taking over the volume from the surrounding high-permittivity tissue region, the electric energy ramps down in the tissue while it only slightly increases inside the proposed geometry. Therefore, the overall stored electric energy is decreasing inside as a function of $\Delta d$. The same behavior is recorded when the power dissipated by dielectrics is taken into account (Fig. 4.3c). In this case, since the dissipated power inside the low-lossy dielectric is orders of magnitude lower than the one dissipated inside the surrounding tissue region, the total value is coincident to the latter. The simultaneous decrease of the average stored electric energy (Fig. 4.3b) and the power dissipated by dielectrics (Fig. 4.3c), while the average stored magnetic energy is kept constant (Fig. 4.3a) explains the increase of the quality factor shown in Fig. 4.2c. Fig. 4.3 shows also a clear performance increase with respect to the coil-only case.

### Measurements

In order to validate the simulations, the dielectric structure presented was built by 3D printing, using the DL-260 resin, and then measured were performed on a Keysight E5061B Vector Network Analyzer (VNA). In order to allow the measurements, the coil+geometry structures were embedded into the stripline presented in Sec. 3.3 (Fig. 4.4a) and, for the sake of comparison, the same structure was simulated in HFSS (Fig. 4.4b). The measurements where made with the structure dipped inside a Phosphate-Buffered Saline (PBS) solution in order to mimic the presence of the body, the simulations were performed including a body fluid medium, to emulate the PBS.

Fig. 4.4c shows the resulting quality factors for a core-less and a TFG core ($\Delta d = 130\,\mu$m). As a result, the simulated and measured structure behaviors are comparable, validating the simulations and confirming the performance increase when the dielectric structure is introduced. On the other hand, a difference is registered in correspondence of the maximum values. This can be explained by

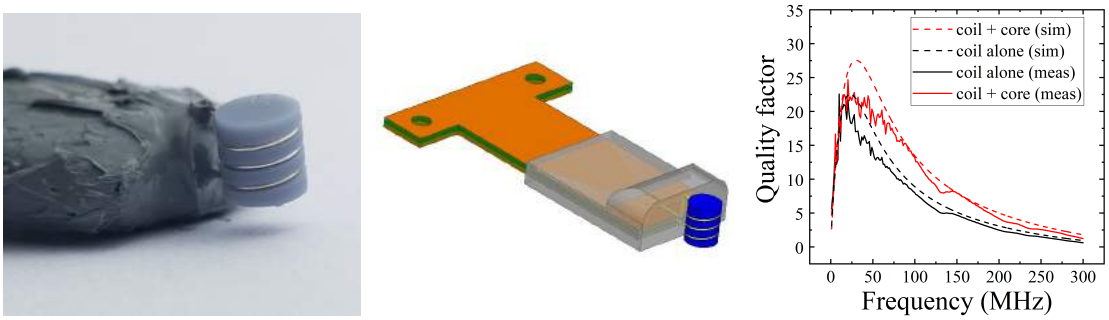


**(a)** **(b)** **(c)**

**Figure 4.4** – The measurement of the proposed structure: the built dielectric TFG (a), the simulation environment (b) and the comparison between simulated and measured quality factors (c).

the difference between the measured and simulated media. In particular, the PBS is more lossy than the body fluid, resulting in more energy dissipated and, from Eq. (4.2), in a lower Q. This is confirmed by the frequency shift that affects both the bare coil and the core-based coil results.

## 4.3 Design of the receiver at constant volume

To further push the study, it is important to consider the overall implanted volume during the optimization. This section presents the development of the RX structure towards this aim, from the definition of a Figure of Merit (FoM), to the simulations performed.

### 4.3.1 The design at constant volume

In contrast with most of the works present in literature, this work takes into account the whole volume of the implant, including the dielectric structure. Unfortunately, the overall implanted volume is barely considered in the literature (coil optimization is usually done without taking the coating volume into account). This leads to an under-estimation of the real volume occupied by the RX. As a matter of fact, this parameter is highly important in implantable structure, since the inflammatory response of the body is dependent on the tissue displacement, and also bigger implants are more invasive, especially in sensitive zones like the brain.

To design the fixed-volume RX coil as well as to compare different structures, the FoM, defined in [112], and presented in 1.2.4, is used. This parameter is especially useful when only the RX is taken into account, since it allows to separately design the RX and the TX. It is obtained by separating the RX and TX parameters of the PTE, defined in Eq. (4.1), and it is defined as:

$$F_{RX} = k_{RX}^2\, Q = \frac{(\mu_{eff} S_{RX})^2}{L}\, Q, \tag{4.6}$$

where $\mu_{eff}$ is the effective magnetic permeability, that can be set equal to $\mu_0$ in tissue environment. $S_{RX}$ is the effective area where the magnetic flux is calculated,

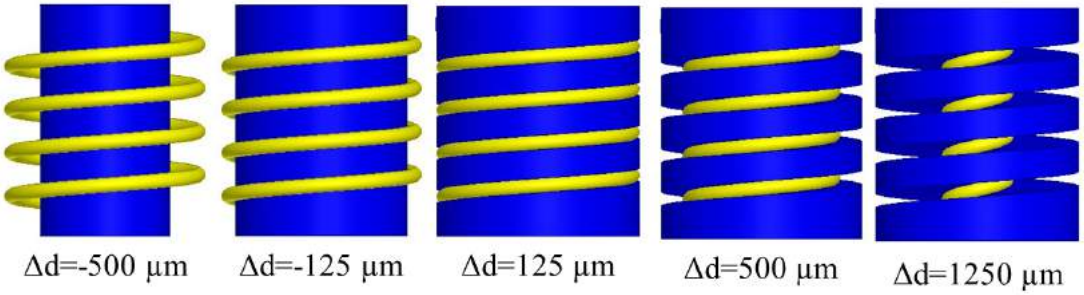


**Figure 4.5** – The design at constant volume: Sketch of different structures having different $\Delta d$. The other parameters are: $r_s = 3.5\,\text{mm}$, $h_s = 4\,\text{mm}$, $h_s = 3\,\text{mm}$, $N = 4$, $r_w = 125\,\mu\text{m}$.

and it can be approximated to the product of the coil section with the number of turns, thus $S_{RX} \approx N\pi r_c^2$. Finally, $L$ and $Q$ are the coil self-inductance and quality factor. Note that no matching between the coil and the load circuit has been taken into account, since it was not part of this study. Taking into account these assumptions in Eq. (4.6), and by discarding the magnetic permeability since it is constant in all the designs, it can be manipulated as:

$$FoM = \frac{(N\pi r_c^2)^2\, Q}{L}, \tag{4.7}$$

expressed in $m^4/H$.

In order to find the best device characteristics, while keeping the whole volume constant, first of all the maximum volume has to be defined. Since the threaded-furrow dielectric structure is the biggest part, the constraints are set to $r_s$ and $h_s$. Once selected, the coil turns and $\Delta d$, are swept, while $h_c$ is kept constant. Fig. 4.5 shows different values of $\Delta d$ with $N = 4$. For the sake of completeness also negative values of $\Delta d$ are taken into account, keeping the coil radius to the maximum value in order to not increase the whole volume ($r_c = r_s^{max} - r_w$) and decreasing the dielectric radius. In this work the maximum dimension of the proposed dielectric structure were set to $h_s = 4$ mm and $r_s = 3.5$ mm, and the wire radius to $r_w = 125\,\mu\text{m}$.

As $\Delta d$ increases, the coil is more confined inside the TFG, allowing more electric field to be "protected" inside the structure, and, as shown in Sec. 4.2, leading to a quality factor improvement. On the other hand, this gain is counterbalanced by the coil radius reduction, decreasing the effective area. A similar effect is expected for the number of turns: by increasing the number of turns the self inductance is increased and the $Q$ factor is decreased, but at the same time the effective area is increased. Therefore, the presence of an optimum value of $\Delta d$ and $N$ that maximise the $FoM$ is expected.

### 4.3.2 Simulation results

Again, the structure shown in Fig. 4.5 was simulated using the EM simulation tool HFSS (Ansoft, Pittsburg, PA), by sweeping $\Delta d$ and $N$ from $-1000\,\mu\text{m}$ to $1250\,\mu\text{m}$ and from 2 to 8, respectively. In order to take into account a real case scenario, the structure was simulated in four different tissue environments: fat,

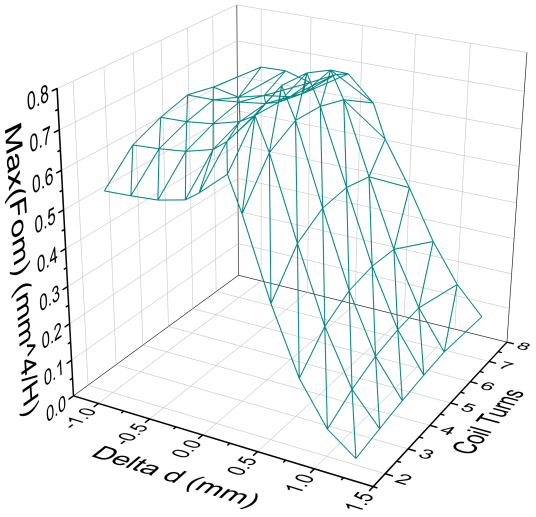


**Figure 4.6** – The resulting simulated FoM in muscle tissue as a function of $\Delta d$ and $N$.

muscle, grey matter and body fluid. In such a way, most of the tissues subject to implantation are taken into account, starting from a low-epsilon low-losses best case scenario (fat), to the high-epsilon high-losses worst case (body fluid). Obviously, the structure is more affected by the surrounding environment in TFG than in coated geometry because in that case there is almost no electric field inside the tissue (Fig. 4.1c).

In order to estimate the $FoM$ defined in Eq. (4.7), the quality factor was computed as indicated in Sec. 4.2, as well as the self inductance, by using the low-frequency value of the apparent inductance, defined as $L^{app} = Im(Z)/(2\pi f)$.

Fig. 4.6 shows the 3D graph of the $FoM$ as a function of $\Delta d$ and the coil turns, taking into account the muscle tissue. In order to build the graph, each combination of $\Delta d$ and $N$ were simulated as a function of frequency, and then the maximum value of $FoM$ was computed, for each structure. Consequently, the different points in the graph correspond to different frequencies. This was chosen since the frequency was not a constraint in this work, and since this study aims at finding the optimum trade-off.

As the figure shows, the FoM is more affected by the variations of $\Delta d$ than the variations of the coil turns. When the radius of the coil is maintained constant and only the number of turns is swept, it can be observed that an increase of the $FoM$ is registered, that reaches its maximum at $N = 4$ and after this value the FoM decreases. This can be easily explained by the initial increase of the effective area while augmenting the turns, but, after $N = 4$, this increase is not enough to compensate the decrease of the quality factor and the simultaneous increase of the self inductance.

To better appreciate the behaviour of the FoM as a function of $\Delta d$, Fig. 4.7 shows this parameter while the coil turns are kept constant to the values that insure the maximum of $FoM$ in each tissue. This value is resulted to be $N = 4$ for muscle, grey matter and body fluid, and $N = 5$ for fat. This is because the lower losses of the latter slow down the decrease of the quality factor as $N$ is increased.

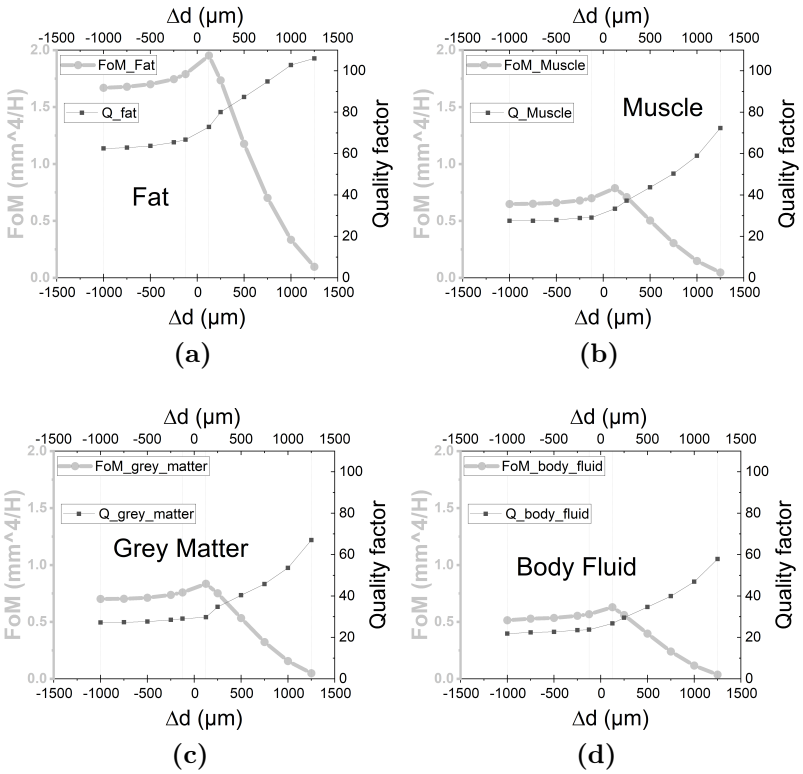


**Figure 4.7** – The simulated $Fom$ and $Q$ at constant volume in fat (a), muscle (b), grey matter (c) and body fluid (d) tissue environment.

For the same reason, as expected, the overall values of the FoM and the quality factor decrease when replacing fat by body fluid.

For all the tissues, the $FoM$ behaviour as a function of $\Delta d$ is the same. For $\Delta d < 0$, the FoM slightly increase with the increase of the dielectric structure dimension, in particular when the cylinder starts to cover the coil ($\Delta d = -r_w$). A maximum is observed when the coil is all the way covered ($\Delta d = r_w$), since in this case the coil is completely covered while the effective surface is at its maximum value. For value of $\Delta d > r_w$, as expected, the quality factor starts to increase but, at the same time, the effective surface starts to decrease (Fig. 4.5). Since the $FoM$ has a quadratic dependence to $S_{RX}$ (Eq. (4.7)), the increase of the $Q$ with $\Delta d$ is not high enough to compensate the decrease of the area. Due to this, the FoM decreases rapidly with the decrease of $r_c$. As a result, for all the tissues taken into account, the best geometry is the one that keeps the coil covered ($\Delta d = r_w$) while keeping the effective area at the maximum value ($r_c = r_s^{max} - r_w$). In this case the quality factor is increased compared to the coil only case, and $S_{RX}$ is kept as high as possible under the design constraints.

## 4.4 Measurements

### 4.4.1 Experimental setup

In order to confirm the simulation performed, some dielectric structures were 3D printed using the DL-260 resin, in continuity with Sec. 4.2. The developed coils have $N = 4$ and different values of $\Delta d$ were chosen (-125, 125, 500 and 1000 µm). Once fabricated, a 250 µm gold wire was wound inside the structures to form the coil, and connected to the stripline, to perform the measurements. In order to ensure as much reproducibility as possible, the connection between the coil and the stripline, by means of the gold wire, was the same for all the structures. Fig. 4.8a shows the structure for $\Delta d = 500$ µm. As for Sec. 4.2, the whole structure was simulated in HFSS, in order to allow comparison between the simulated and measured case. Fig. 4.8b shows the implemented simulated structure. Simulation were performed including tissue environment, in order to reproduce the real case scenario. The tissue was modelled as a cube and the stripline was inserted inside it. Fig. 4.8c shows the whole simulation environment. Measurements were performed using the Keysight E5061B Vector Network Analyser. Minced bovine meat at room temperature (21-23°C), to ensure repeatability, was used to mimic the muscle tissue (Fig. 4.8). The structure attached to the stripline was placed inside a little hole made on the side of the meat, and then the latter was squeezed onto the structure to insure the placement of the meat all around the coil. Fig. 4.8d shows the measurement setup once the structure was in place.

In order to minimize the effect of the stripline in the measurements, a de-embedding routine was set when post-processing the data. Fot that, an open and a short circuit were fabricated by placing the terminations inside the stripline, 2 mm from the end. This because it was no possible to have an ideal configuration at the strucure far end, due to the presence of the lossy tissues. After measurement of the two calibration circuits, the stripline was de-embedded using the following [170]:

$$Z = \frac{1}{Y_{meas} - Y_{open}} - \frac{1}{Y_{short} - Y_{open}}, \tag{4.8}$$

where $Z$ is the de-embedded impedance, $Y_{meas}$ is the measured admittance, $Y_{open}$ and $Y_{short}$ are the measured admittances of the open and short circuits.

### 4.4.2 Results

#### De-embedding

The Q factors resulting from measurements, performed in minced bovine meat, with and without de-embedding are reported in Fig. 4.9a shows the resulting Q factor. For each structure, the two curves are highly comparable, in particular up to about 150 MHz. At higher frequencies, the de-embedded measurements have a slightly higher Q, with a self-resonance frequency projection higher than the simple measured one. This can be explained the de-embedding removes the parasitics introduced by the stripline, in particular in the high-frequency range. On the other hand, the de-embedding post-processing procedure introduces non-negligible *noise*

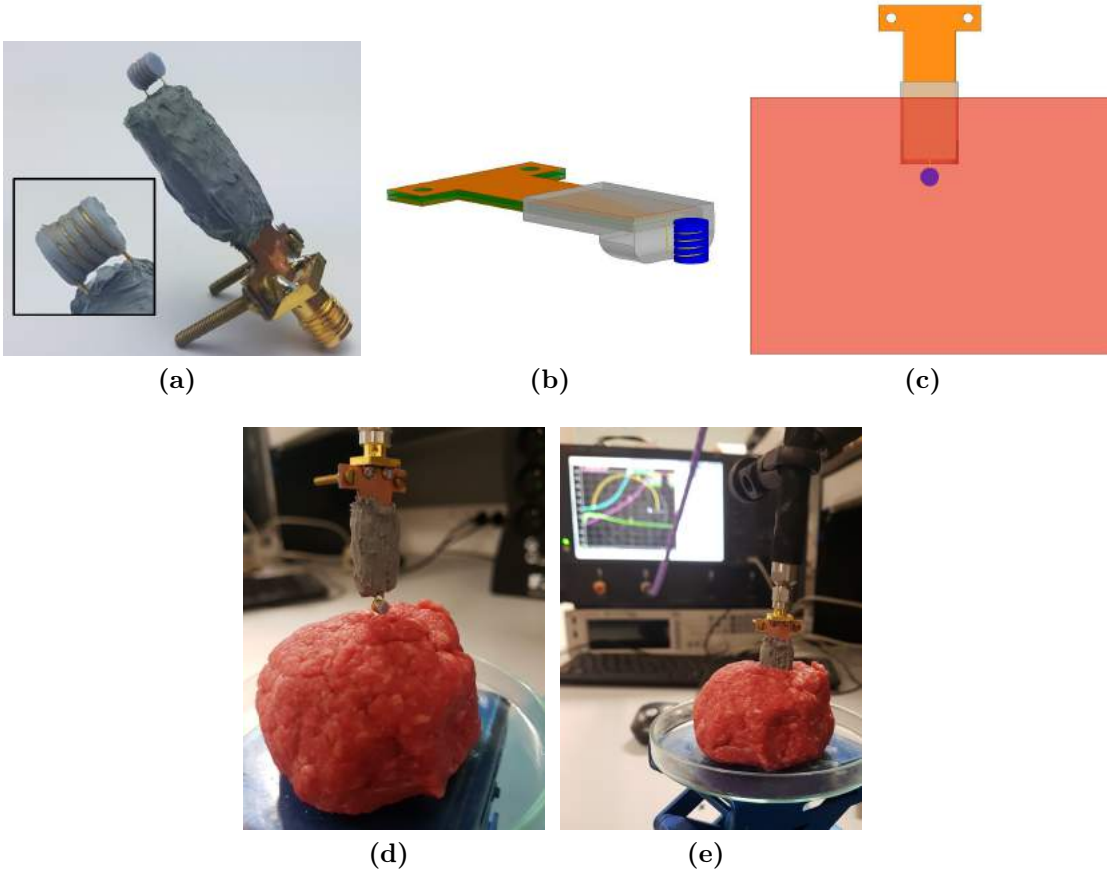

**Figure 4.8** – The built prototypes: the prototype connected to the stripline for $\Delta d = 500\,\mu\text{m}$ (a), the corresponding simulated structure (b) and the simulation environment, including the tissue (c); the minced meat used to mimic the muscle environment (d) and the measurement setup (e).

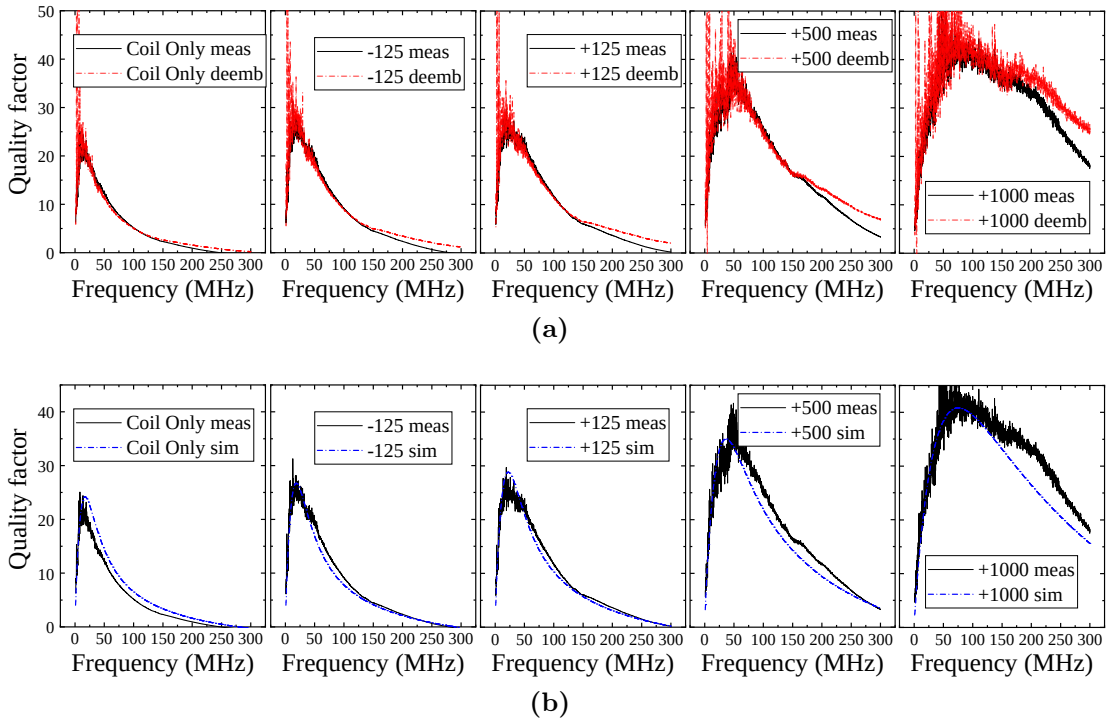


**Figure 4.9** – Measurement results 1: The comparison between the measured quality factor in bovine minced meat for different values of $\Delta d$ before (black) and after (red) de-embedding (a) and the comparison between measured (black) and simulated (blue) ones.

to the measurements. This, added to the fact that the de-embedding results seem very similar to the raw data in the region of interest (i.e. in the neighbourhood of the maximum), led to the decision to not consider the de-embedded measurements for the following analysis of the results.

### Q factor and Figure of Merit

Fig. 4.9b shows the comparison between measurements and simulation as a function of frequency for all the developed structures. The figure evidences a very good agreement between the two curves for each value of $\Delta d$. For $\Delta d = 125\,\mu m$, the maximum measured Q factor is slightly lower than the simulated one. This can be justified by the fact that the developed dielectric structure coil lodgement, due to resolution limits of the 3D printer, is not capable to cover the entire coil wire, exposing the electric field to the lossy tissue. For this reason, in contrast with simulation, the measured Q factors for $\Delta d = -125\,\mu m$ and $\Delta d = 125\,\mu m$ have a very similar behavior. On the other hand, a little increase of the quality factor is witnessed at $\Delta d = 500\,\mu m$ and $\Delta d = 1000\,\mu m$. This is probably because, even if accurately squeezed, the meat is not completely entering inside the dielectric structure depressions.

By taking each Q factor maximum value of Fig. 4.9b, the FoM, defined in Eq. (4.7) was computed. Also in this case, the self inductance was calculated using the low-frequency value of the apparent inductance. Fig. 4.10 shows the

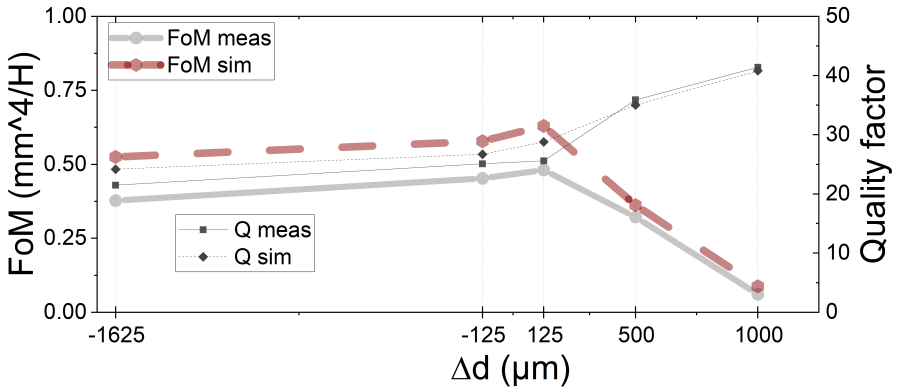


**Figure 4.10** – Measurement results 2: The resulting measured FoM and maximum quality factor in muscle tissue as a function of $\Delta d$ and the comparison with simulations.

FoM, as well as the maximum quality factor, as a function of $\Delta d$ for the measured structures. For the sake of comparison, the simulated FoM and quality factors are also reported. Note that the value $\Delta d = -1625\,\mu m$ corresponds to the case when no dielectric is inserted inside the coil, i.e. the coil-only case.

In continuity with Fig. 4.9b, the maximum measured and simulated quality factors are in very good agreement. The only tangible difference is observed at $\Delta d = 125\,\mu m$, due to the not perfect covering of the coil wire, as introduced earlier in this section.

The resulting FoM has the same behaviour of the simulated curves presented in Sec. 4.3, having the resulting best structure for $\Delta d = 125\,\mu m$. Also in this case the simulations and measurements are in good agreement, with the measured values always underneath the simulated ones. This is because the measured apparent inductances resulted to be slightly greater (of the order of less than 1 nH) than the simulated ones. This difference gets smaller at high values of $\Delta d$, where the two curves are almost overlapping. The overall resulting FoM values, for both simulations and measurements, are lower that the simulated ones presented in Fig. 4.7, this can be easily justified as ideal-case simulation have been undertaken first.

The measurements confirm that the best shape of the dielectric structure to insure good wireless PTE, as well as good contact between the coil/electrode and the tissue, is the one that covers completely the metal, while keeping the largest coil as possible. This structure has also the advantage to put the metal and the tissue in direct contact, while this is harder to achieve when $\Delta d$ increases, due to the fact that the coil metal is insulated inside the furrows of the dielectric (Fig. 4.5) and thus less exposed to the tissues. Therefore, a higher sensitivity of the electrodes is expected for the best structure.

## 4.5 Application

To demonstrate a possible impedancemetry sensor function, impedance measurements of *ex-vivo* tissues were performed using the designed device, opening new

applications such as: small, wireless, energy independent impedancemetry system to monitor the inflammatory response of the body after implantation.

### 4.5.1 Bioimpedance measurements of a swine heart

A first validation of the impedance measurements was performed by using the developed structures presented in Sec. 4.2. A comparison with measurement performed using a human cardiac commercial lead was performed. Two types of tissues were targeted, one characterised by muscular tissue and one having a higher concentration of collagen, as produced in the fibrosis development [171], after an implantation of a foreign object inside the body. Therefore, the two measurements are representative of the inflammatory response of the body, following-up an implantation.

#### Measurement performed

The measurements were performed on an *ex-vivo* young swine (Large White, $40 \pm 5$ kg) heart. Two different regions were selected and measured: the lateral wall of the left ventricles ("healthy") and a region near the auriculo-ventricular ring and the basal region ("collagen"). Fig. 4.11a shows the measured swine heart, the two regions are evidenced. During the measurements, the heart was immersed in a cardioplegic solution and placed on ice in order to avoid fast tissue degradation.

As introduced earlier, two different structures were used to measure the impedance: a Sprint Quattro Secure 6947M (Medtronic, USA) cardiac pacing/defibrillating lead, and the TFG structure fabricated and tested in Sec. 4.2. In the first case the impedance was calculated between the helix electrode, screwed inside the tissue, and the ring electrode, these two electrodes are shown in Fig. 4.11b. In order to allow the measurement using the coil structure, two dielectric geometries were placed end-to-end, each one with a coil and mounted on the stripline presented earlier, as Fig. 4.11c shows. Regarding the proposed structures, two measurement conditions were tested: one by placing the electrodes on surface of the measured medium, and one by making a small incision on the tissue surface et placing the coils inside it.

The measurements were performed using a Solartron 1260 (Ametek, USA) impedance spectrometer, with an amplitude of 100 mV and a frequency sweep from 1 Hz to 1 MHz.

#### Results

Fig. 4.12 shows the measured impedances resulting from the performed tests on the swine heart, using the commercial cardiac lead (Fig. 4.12a) and the structure proposed in this work (Fig. 4.12b). In both graphs, the typical behaviour of the tissue impedance is evidenced, with a shift towards higher frequencies registered while the dielectric structures are used. Also a big shift, of about one order of magnitude, is recorded on the impedance magnitude between the measurements with the two different structures. Both of these results are explained by the change of the measuring electrodes, and therefore by the frequency shift, since no calibrations

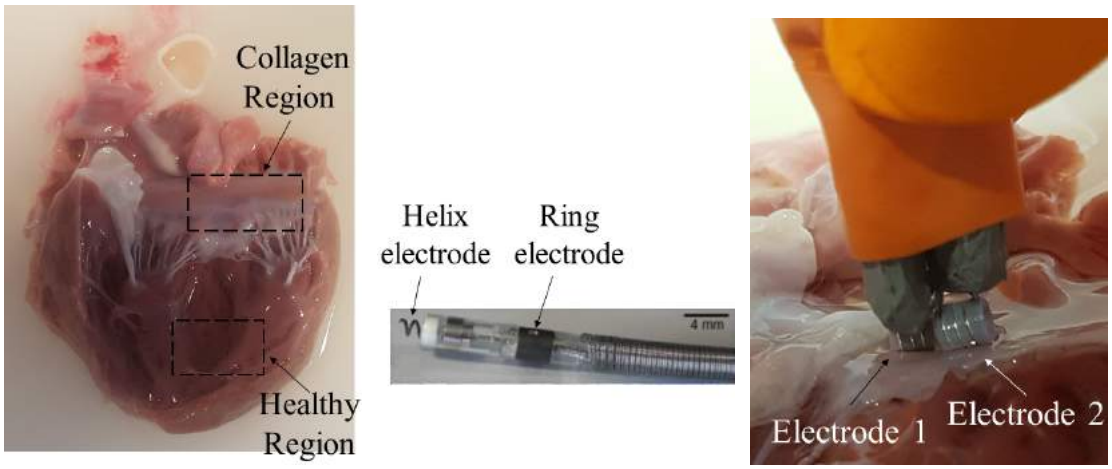


(a) (b) (c)

**Figure 4.11** – The bio-impedance measurement on a swine heart: the measured cardiac tissue (a), the Sprint Quattro Secure 6947M lead (b) and the two dielectric threaded-furrow geometries used as electrodes (c).

are considered to place the reference plane at the end of the structures. Therefore, the impedance of the measuring probes is also taken into account while performing the measurements. This because the goal of these measurements was the observation of a difference in the impedance of the two tissues taken into account, not an absolute measurement of the tissue impedances. Fig. 4.12b also evidences a difference between the two performed measurements using the dielectric structures, with the one performed on the surface resulting to be more sensitive to the change of tissue.

As expected, for both structures, a shift of the impedance magnitude is observed between the "healthy" and the "collagen" tissues, due to the higher conductivity of the second one. Also a significant difference between the phases of the two different tissue types is observed in the high-frequency region. For the sake of completeness, Fig. 4.12c reports the difference between the measured impedance magnitude, defined as $\Delta \mid Z \mid = \mid Z \mid_{healthy} - \mid Z \mid_{collagen}$ in the 10 Hz - 1 MHz range. For the proposed structure, the surface measurement only is reported. The graph shows similar values and behaviour of the two structures. The two curves do not overlap due to the frequency shift between the lead and the TFG measurements.

The results evidence the capability of the proposed structure to observe the impedance difference between an healthy cardiac tissue and a tissue where fibrosis has been developed, opening the possibility to design a wireless impedance monitoring system, capable to monitor the inflammatory response of the body to an implant, by designing a dedicated electronic circuit.

### 4.5.2 Conclusion

A novel structure has been developed in order to improve the WPT capability of a bare coil while keeping the contact between the tissue and the conductor. This allows a sensing or excitation capability of the structure without the need

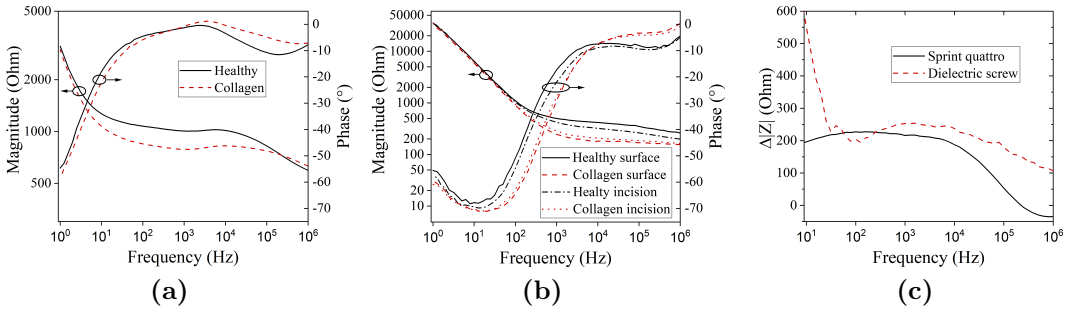


**Figure 4.12** – The measured bio-impedance magnitude and phase: the Sprint Quattro Secure 6947M lead results (a) and the two dielectric structures used as electrodes results (b). For the latter, the two different measurements performed are reported.

of adding external electrodes, minimizing the implant volume. The structure was designed, simulated and validated by measurements. Quality factor improvements were registered compared to the bare coil case.

In order to take into account the whole volume of the implant, a design routine, keeping the volume constant, was defined. In particular, a FoM was used to maximize the RX characteristics, without taking into account the TX placed outside the body.

The best geometry parameters were defined by simulations, taking into account different tissue environments. For all the tissues, the best geometry is resulted when $r_c = r_s^{max} - r_w$ and having 5 turns for fat and 4 turns for the other tissues. In all cases an improvement with respect to the bare coil case was registered.

This assumption was confirmed by measurements in minced meat, that showed very good agreement with simulations.

Finally, impedance measurements of *ex-vivo* swine cardiac tissues have been performed in order to show a possible application of the structure. The proposed structure has evidenced the capability to monitor tissues similar to the evolution of the tissues during a fibrosis development, following an implantation.

# Chapter 5

# Extremely low-cost UHF-RFID batteryless tag body temperature sensor on carboard substrate

In order to extend the Radio Frequency Identification (RFID) tags designed and presented in Chapter 2 to human application, this chapter presents an alternative implementation of the Complementary Split Ring Resonator Antenna, shown in Sec. 2.3. The design of the antenna was edited in order to develop an ultra-low-cost, battery-less wearable Ultra High Frequency (UHF)-RFID tag with body temperature monitoring capabilities. In particular, as presented in the following sections, corrugated cardboard was selected as substrate and the antenna was designed as a sticker, made out of adhesive copper tape. The idea is to allow easy body temperature screening, in case of emergencies, in zones where the low-cost and sourceable of simple substrates are crucial. The following sections describe all the design process, the antenna development and the results achieved.

## 5.1 Introduction

The body temperature increase has been known for years as a first sign of illness [172]. It is an early symptom of epidemic and pandemic diseases like Ebola virus infection [173], Dengue fever [174] and Malaria [175], that are particularly effective in developing countries such the central African countries. An early diagnosis of these infections is crucial in order to contain the diffusion, by isolating the contaminated subjects, and to effectively treat the patients, by also trace the body temperature evolution in time. Therefore, a mass scale temperature screening is required in effected areas. In order to carry out this task, a fast, to screen as many people as possible in the fastest time possible, and contactless, to limit the operator risks, temperature measurement is required. Moreover, due to the economic difficulties of the developing countries, a simple and low cost solution is required to insure the largest screening scale possible.

The most classical way to perform the measurement is carried out by a gallium-in-glass, that has replaced mercury, thermometer, but the measurement can take up to 5 minutes and it requires contact with the patient. Infrared thermometers

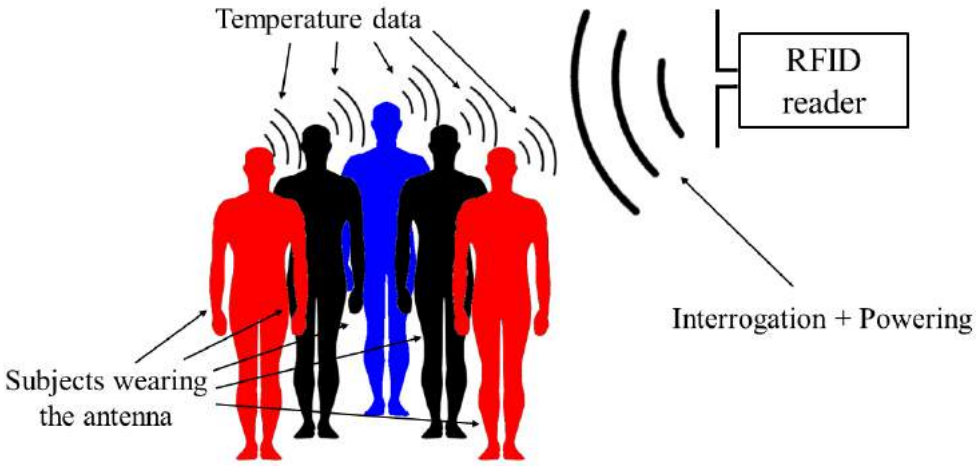


**Figure 5.1** – The setup of the proposed temperature screening system.

offer a faster alternative to check the body temperature, performed in the eardrum, needing direct contact with the body, and the forehead, performed contactless [176]. On the other hand, these devices need to be placed close to the head of a potentially infected subject (at a distance of less than five centimetres) and they allow just one measurement at a time. To overcome these problems, thermal cameras have been used to perform fast tests in crowded places like airports [177]. They seems to be the best choice for mass temperature screening in well developed countries, but their high cost limits their usage in case of epidemics in poorer regions and they are not suitable for continuous monitoring of patients.

One possible solution to overcome all these limitations is the implementation of a wireless Radio Frequency (RF) link between a wearable device having temperature monitoring capabilities, worn by the potentially effected subject, and a base station, where the temperature data are collected. Devices using bluetooth technology have been proposed, but they often rely on batteries [178] or need complex energy harvesting circuits [179] to insure the power amount required to perform the monitoring and communication. Thus, the deployment of these devices in remote areas is limited. RFID tags are a powerful alternative, since they can work in a completely passive mode, harvesting the necessary power from a reader placed inside the minimum tag reading distance. This distance can go up to the order of meters if UHF RFID technology is used [180], also in wearable applications [147]. Fig. 5.1 shows the typical application scenario. A RFID reader is placed in an optimal spot and it sends a signal that interrogates and powers the tags. The potentially effected subjects wear a specially designed tag antenna and they move at a readable distance in order to be detected. The RFID tags collect the temperature information of the subject and send it back, via backscattering, to the reader. Moreover, thanks to the unique identification code of each tag, the subject having fever can be easily detected in case of crowded spaces.

Some wearable temperature sensor RFID tags have been proposed. In [134] the authors propose a highly wearable flexible tag able to monitor the body temperature. This monitoring has been proven during exercise bike effort. The tag was futher miniaturised in [133]. But, as explained in Sec. 2.4, the counterpart of

designing a high wearable epidermal RFID tag is the poor resulting Reading Range (RR), due to the body tissue characteristics [78], as shown in [145]. Therefore, to achieve a RR greater than one meter, a battery is added to this kind of tags [133], improving the chip sensitivity. Highly-wearable epidermal electronic antennas are not suitable if passive long range tags are required. In fact, as mentioned earlier in this manuscript, they are highly affected by the presence of body tissues, where they are often directly attached [159]. Therefore, this kind of design gives priority to patients comfort than radiation performances. On the contrary, in case of emergencies like the ones described in this paper, the effectiveness of the intervention have to be preferred respect to the comfort.

In order to limit the body tissue effects, and thus to increase the RR in passive mode, in [181] a 3D-printed, grounded, wearable, temperature monitoring RFID tag is presented. But the proposed tag includes via-holes, and uses PLA substrate that needs to be shaped using expensive 3D printers. In order to make this technology accessible wherever in the world, including developing countries, low-cost and widely available substrates have to be preferred.

This work proposes to recycle corrugated cardboards. The only part that will be provided is the metal tag, made out of copper adhesive tape, including the RFID chip, that can be easily sticked on the selected substrate. The tag can be carved using low-cost two-axis cutting plotter. The idea is that the operator interested to monitor the temperature can cut the substrate to the desired size and then simply stick the provided metal part. In order to achieve this, the design has to be as simple as possible, not including for example via-holes, allowing the fabrication on low-resolution, low-cost plotters and an easy placement of the metal sticker on the substrate.

The next sections describe all the design process, starting from the definition of the design constrains to the validation of the proposed tag.

## 5.2 Tag design

### 5.2.1 Design constraints and needs

The RFID tag antenna specifications can be divided in two main branches: the tag characteristics and the substrate selection and remarks.

#### Tag characteristics and placement on the body

In order to screen many people at a time, a reasonably high tag RR is required. For this work, a minimum RR of 1 meter was selected. This allow the high placement of the reader antenna, minimizing the superposition of different monitored subject, as Fig.5.1 shows. To achieve this, the tag has to be used in complete passive mode, to avoid the need of batteries and the consequent inoperability in case of battery absence or discharge. As explained in the introduction, the high RR can be obtained in spite of tag wearability.

Moreover, to correctly measure the temperature of the subject, the tag has to allow the chip placement in direct contact to the skin, on the antenna backside. On the other hand, as explained in Sec. 5.1, no via-holes are allowed to connect the

chip pins to the tag frontside, and a single copper tape sticker should be designed to form the whole antenna.

Finally, one other important issue is the placement of the tag on the body surface. In order to allow multiple measurements on different subjects, the forehead was selected. This is also in continuity with infrared thermometers, that are often used on this body part to check the body temperature, since forehead temperature is close to core body temperature.

#### Substrate selection and remarks

Currogated cardboard was selected as substrate thanks to its wide availability and low-cost. This material is often used to pack many goods like medicines and food, thus is highly probable that it can be found also in any remote areas. Moreover, thanks to the low density of this material, it presents quite low dielectric losses [182] as an extremely low-cost material not originally designed for RF purposes. In particular, cardboard having a flat linerboard on both sides was chosen, since it allows an easy placement of the copper tape sticker. A thickness of 3 mm was taken into account for the tag design.

On the other hand, due to the wood nature of this material, the cardboard absorbs the humidity, changing its dielectric characteristics. This is particularly important in this work, since the countries taken into account are often characterised by high humidity levels. It has been shown that the cardboard water content can pass from 6-10g/100g at 40% relative humidity, to 14-18g/100g at 90% relative humidity [183]. Consequently, the material dielectric permittivity can vary from 1.28 at 6.5g/100g to 1.4 at 18g/100g. Also the dielectric losses, expressed with the $\tan\delta$, are affected, passing from 0.007 to 0.027 from 6g/100g to 18g/100g respectively. In the worst case scenario of 25g/100g water content, the resulting cardboard measured dielectric permettivity and losses are 1.5 and 0.038 respectively [184]. Other parameters can affect these values, like cardboard density, and material wear. These dielectric shifts have to be taken into account during the design process, since the tag antenna has to be usable with any cardboard type in any humidity condition.

### 5.2.2 The proposed tag antenna [1]

In continuity with other tags proposed in literature to monitor the body temperature [133, 181], the EM4325 (EM-Microelectronics, Switzerland) Integrated Circuit (IC) was selected. This UHF-RFID chip has an in-built temperature sensor that ranges from $-40$°C to 60°C with a resolution of 0.25°C. This resolution is high enough to detect possible effected people, who can be then controlled with more sensitive instruments in case of positive response. This chip is characterised by an impedance of 17.6-j113 Ω at 915 MHz and a relatively limited sensitivity in passive mode $p_c = -4.5$ dBm [136].

1. An antenna with a shape similar to the one proposed here was already presented in Sec. 2.3, as mentioned at the beginning of this chapter. However, for the sake of chapter completeness, the design steps are here reported, with more comprehensive analysis.

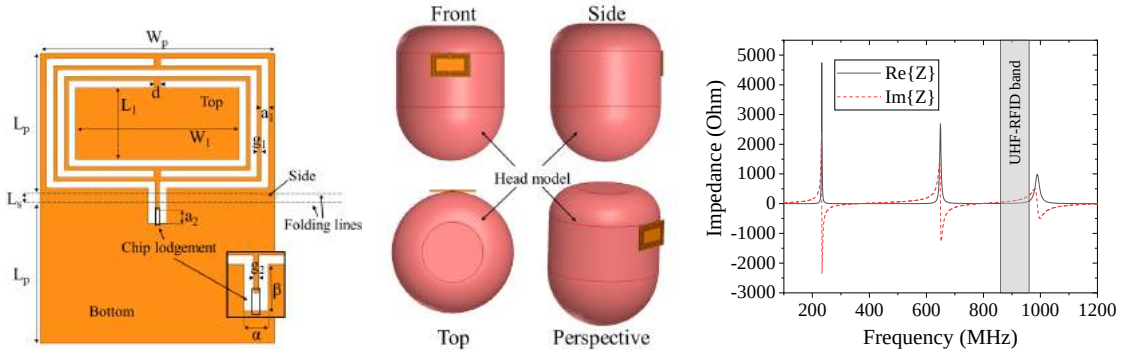


**(a)** **(b)** **(c)** .

**Figure 5.2** – The proposed patch tag: single-patch antenna shape and dimension (a), the assembled antenna placed on the fronthead of an head model (b) and the simulated broadband input impedance of the tag (c)

In order to attain the required RR, it was chosen to include a ground plane in the design, to preserve good radiation performances when the antenna is worn by the subject [185]. Due to image theory, dipole-like antennas lose their advantageous radiation characteristics when placed upon a metal ground plane. This is because the field created by the current flowing through the antennas is cancelled by its image source. On the contrary, horizontal magnetic flow produces an in-phase image source, enhancing its radiation performances [186]. In this work a slot antenna was designed to produce the horizontal magnetic flow.

Fig. 5.2a shows the planar shape of the proposed copper sticker that has to be folded on the cardboard substrate to form the antenna. When attached to the substrate, it covers three sides of it. The shorted side (*side* in the figure), beside presenting good radiation performances [187], ensures the mechanical continuity between the top radiating side and the bottom side, having the ground plane and the chip lodgement. This allows to have the full antenna in a single patch sticker. Fig. 5.2b shows the representation of the real application scenario: the assembled antenna is placed on the forehead of a person in order to monitor his body temperature.

The tag itself consists in a folded patch with three slots. The two inner slots form a complementary split ring resonator, that has been already used to design RFID grounded antennas [158]. The third, outer slot is included to achieve a third resonance, as Fig. 5.2c shows. This resonance is meant to ensure highest radiation performances and bandwidth (as seen from simulations). Therefore, the antenna was shaped to have his third resonance just above the UHF-RFID bandwidth (860-960 MHz). Moreover, the outer slot has a stub (evidenced in the Fig. 5.2a), that allows the placement, without via-holes, of the chip on the bottom side, in direct contact with the skin. By acting on $\beta$, the resonance frequency can be easily tuned, to match the desired value, in case of particularly frequency band constraints.

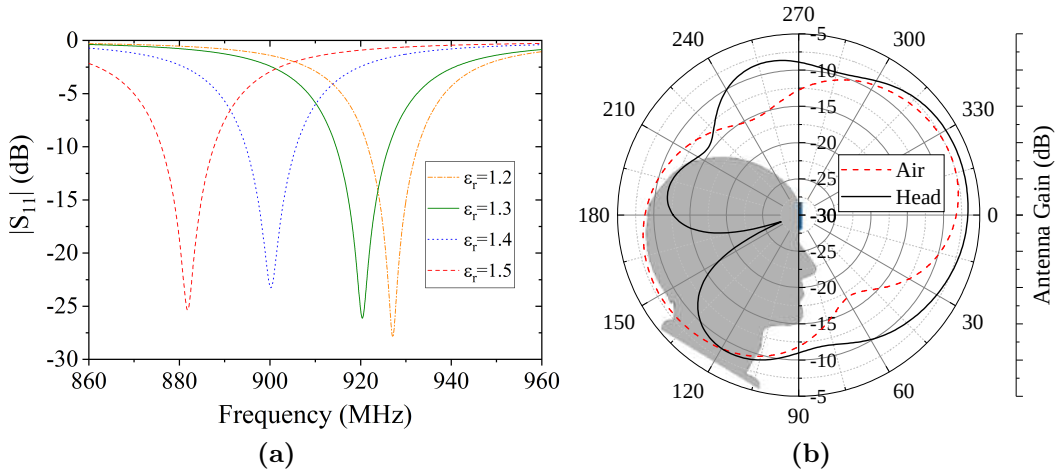


**Figure 5.3** – The simulation results: the simulated |S11| in air for different substrate epsilon (a) and the simulated radiation pattern for $\phi = 90°$ in air and on the head model at 915 MHz, including a human head silhouette carrying the tag antenna (in blue) (b).

### 5.2.3 Tag antenna dimensioning

The antenna was simulated using Ansoft High-Frequency Simulation Software (HFSS) in order to obtain optimal dimensioning. Design attentions were paid to the two critical aspects of an RFID tag: the chip impedance matching and the antenna gain.

The resulting optimal dimension, for a substrate thickness of 3 mm are (in mm): $L_p = 45$, $L_s = 3$, $L_1 = 23$, $W_p = 75$, $W_1 = 52.5$, $a_1 = 2.3$, $a_2 = 4.4$, $g_1 = 1.2$, $g_2 = 1.3$, $d = 2$, $\alpha = 5.9$ and $\beta = 11.3$.

Since the tag has to be resilient to the shifts of the substrate dielectric permittivity, this parameter was swept and the tag dimensions were optimized in order to allow good impedance matching in the whole $\epsilon$ range. Simulations were performed on air by sweeping this parameter from 1.2 to 1.5, for the reason explained in the last section. The dielectric losses were kept constant to a worst-case value $\tan\delta = 0.03$. Fig. 5.3a shows the resulting |S11|, with respect to the chip impedance, for the considered $\epsilon$ values and antenna dimension previously mentioned. The antenna shows a good matching (|S11| < -20 dB) for all the considered permittivities, and all the resonance frequencies are within the UHF-RFID range. For this study, the whole 860-960 MHz bandwidth was considered, since most developing countries do not have band regulations inside this range [188].

The simulated radiation pattern at 915 MHz, considering $\epsilon = 1.3$ and $\tan\delta = 0.03$, for $\phi = 90°$ is shown in Fig. 5.3b. Two different conditions were taken into account: tag in air and placed on the forehead. For the latter, the head model shown in Fig. 5.2c was taken into account. The head was designed as a cylinder having radius 10 cm and height 250 cm. To obtain a *head-like* shape, the two circular edges were rounded with a radius of 5 cm for the upper side, and 10 cm for the lower one. The head model dielectric proprieties were set equal to the human head average proprieties: $\epsilon_{head} = 41.2$ and $\sigma_{head} = 0.95$ S/m [142].

The antenna was specially designed to have a main lobe tilted with respect to the tag perpendicular axis, in order to better radiate towards the reader, placed in a higher position than the subjects heads. This if it is worn with the shorted side up, as Fig. 5.2b shows. A human head silhouette is included in the figure, including the sketch of the tag profile, to help the comprehension of radiation pattern. In air, the antenna shows two main lobes, due to the reduced ground plane size When the antenna is worn, as expected, a single main lobe is obtained, having more omnidirectional characteristics with respect to the air case. Also radiation improvements are registered in the head case: the maximum gain passes from $-7.48$ dB in air to -6.47 dB on the head. It has been estimated from simulations that the stub presence highly decreases the maximum gain, of about 4-5 dB, but its design is required to comply with the design constrains (IC in contact with the head).

The resulting radiation properties are also robust to the frequency and substrate permittivity shifts. The maximum gain ranges from -8.35 dB at 860 MHz to -7.38 dB at 942 MHz in air, with a $\Delta gain_{air} = 0.97$ dB. On the head, the registered shift is $\Delta gain_{head} = 0.38$ dB, ranging from -6.74 at 960 MHz to -6.36 at 874 MHz. Also a gain shift of less than 1 dB was recorded for both simulated cases, while passing from $\epsilon = 1.3$ to $\epsilon = 1.5$ for the cardboard.

Finally, the antenna polarization resulted to be linear, having the polarization plane perpendicular to the tag long edge, i.e. the tag is vertically polarized if placed on the head in the intended way, as shown in Fig. 5.2b.

## 5.3 Antenna characterization

The designed patch was fabricated using a low-cost cutting plotter (Silhouette CAMEO 3, Ankersmit, France). Fig 5.4a shows the resulting shape, including the RFID chip. Kapton adhesive tape was used in order to avoid unwanted pin short contacts. To reproduce a real case scenario, a random corrugated cardboard box, used to deliver electronic components, having wall thickness of 3 mm, was cut to obtain the 75 x 45 $cm^2$ substrate. The bottom part of Fig 5.4a shows the resulting substrate. As previously mentioned, the precise dielectric characteristics of the material were unknown.

The adhesive copper tape was accurately sticked onto the cardboard. Fig. 5.4b shows top and bottom sides of the resulting structure. The tag RF characteristics were then studied, and are reported in the next sections. In order to fit the measurements with the simulations, retrosimulations were necessaries in HFSS, to evaluate the cardboard dielectric constant. Also in this case the simulated cardboard $\tan\delta$ was kept constant to 0.03.

### 5.3.1 VNA measurements and results

The first characterization was performed using a Keysight E5061B Vector Network Analyser to study the antenna in reflection. To measure the tag impedance, the technique presented in Sec. 2.2.2 was used. The test fixture shown in 2.3a was soldered to the two ends of the antenna chip lodgement, perpendicular to the

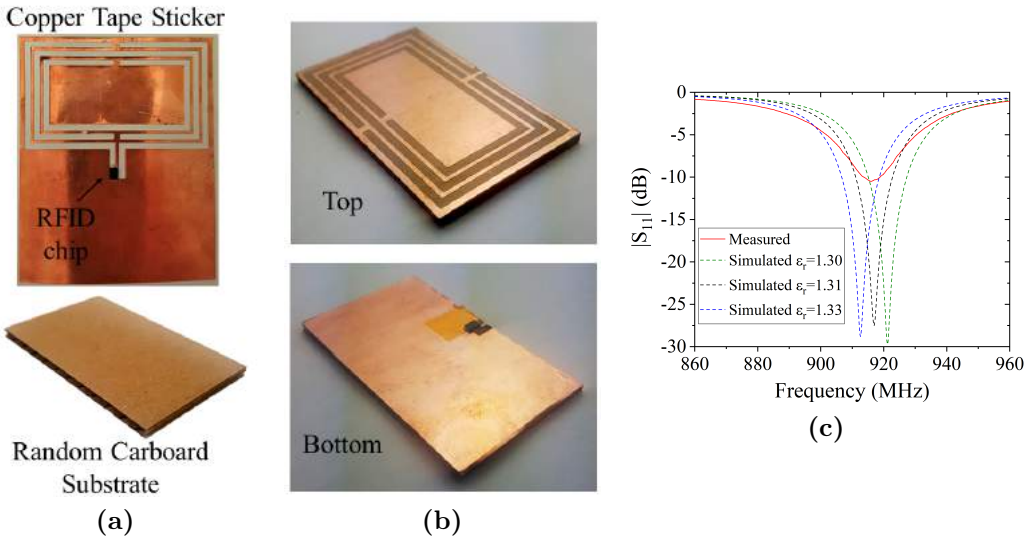


**Figure 5.4** – The fabricated tag antenna: The two antenna components (a), the assembled antenna (b) and the measured reflection coefficient (c).

antenna bottom plate. Two U.FL cables, were connected to two VNA ports and then calibrated using the calibration kit shown in 2.3c. Finally, the antenna was connected and the procedure presented in [157] was implemented. Measurements in air only were performed, since, due to the presence of the test fixture, forehead measurements were not possible.

Fig. 5.4c shows the resulting measured |S11| parameter and the comparison with simulations, plotted with respect to the chip impedance. The measured tag presented a resonance at 916 MHz, with a magnitude of -10.5 dB. It turned out to have a good agreement with the simulated structure having $\epsilon = 1.31$, as the figure shows. For the sake of completeness, the simulated curves for $\epsilon = 1.30$ and $\epsilon = 1.33$ are also reported. The differences in magnitude and width can be explained by the $\tan\delta$ differences between the measurement and simulations and, mostly, by the presence of the test fixtures, the cables and the measurement setup in the near field of the antenna, that modify the EM field configuration and thus the tag impedance.

### 5.3.2 Radiation characterization

#### Measurement setup

The manufactured tag, including the RFID chip (Fig. 5.4b), radiation properties were characterised using the turn-on method [189] in order to measure the tag realised gain. This parameter, formed by the product between the tag radiation gain $G$ and transmission coefficient $\tau$, is the most important figure of merit to quantify the performances of an RFID tag.

In particular, a commercially available equipment, the Voyantic Tagformance, was used at this purpose. This instrument, that acts as an RFID reader, was connected to a linearly-polarized log-periodic antenna having known gain and cable losses. The tag was placed at a fixed distance to it. This reader, for each swept


(a) (b) (c) (d)

**Figure 5.5** – The tag characterisation: The on-body measurement on the arm (a), chest (b), head (c) and on a body phantom (d).

frequency, is able to measure the minimum transmitted power required to read the tag. Then, by inverting Eq. (2.3), the realized gain can be computed. To maximise the polarization efficiency, the reader and tag antenna were oriented accordingly. The frequency was swept with a step of 5 MHz and the transmitter power step was 0.5 dBm.

Measurements were performed in air, using a tag holder having epsilon close to 1, and while reproducing some real case scenarios, placing the tag on different body parts. In particular, the tag was measured while placed on the arm (Fig. 5.5a), chest upon a cotton t-shirt (Fig. 5.5b) and the targeted spot of this work: the forehead (Fig. 5.5c). Please note that in this last case the antenna was tilted of 90° degrees with respect to the designed scenario of Fig. 5.2b, in order to match the reader antenna polarization. Finally, the antenna was also measured when placed on a phantom model, mimicking muscle tissue, having declared characteristics of $\epsilon_{phantom} = 54.5$ and $\sigma_{phantom} = 0.6$ S/m (AET Aqueous gel No. 36 [190]). For all the measurements the distance between the two antennas was set to 50 cm.

### Results

Fig. 5.6 shows the resulting realized gains and the comparisons with the simulations. In Fig. 5.6a the realized gain is computed in air and on the head, taking into account simulations and measurements. In continuity with the previous section, the simulated cardboard permittivity was swept to search the value that better fits the measurement. As evidenced in the reflection coefficient measurement, the measured tag shows good agreement with $\epsilon = 1.31$ in air. The higher registered gain can be explained by a difference between the simulated and real cardboard characteristics. Regarding the head measurement, a resonance frequency red-shift was observed with respect to the air case. This was expected due to the presence of the high dielectric tissues and the absence of the additional copper foil added in the setup presented in Sec. 2.3. Lower agreement between simulation and measurement was evidenced, probably due to the differences between the head model and the real one, and the 90° tilt between simulation and measurement. Moreover, some alignment offset between the two antennas might have occurred. But, for

both cases, the results are coherent with simulations.

The maximum registered realized gain in air and on the head is -7.2 dB at 915 MHz and -7.6 at 895 MHz, respectively. The resulting maximum estimated reading ranges, by assuming the worldwide maximum allowed EIRP of 4 W, are $RR_{air} = 1.21$ m and $RR_{head} = 1.18$ m, both satisfying the design constraint of a minimum RR of one meter.

Fig. 5.6b shows the measured realized gains obtained in air, for different antenna placements on the body and on the muscle phantom. Regarding the arm, two different situations were taken into account, with the tag more (Arm pos. 1 in the figure) or less (Arm pos. 2) adherent to the skin. All the obtained maximums are inside the UHF-RFID band, while significant magnitude differences were observed. This is explained by the different dielectric proprierties for each case, that modify the resonance frequency, the gain and the transmission coefficient. The resilience of the tag, to its position, could be increased by enlarging the bottom ground side at the sections where the electric density energy presents a peak [185], but paying this with an increase of the overall tag footprint, further reducing the patient comfort/acceptance.

The radiation pattern for the air case was obtained by turning the tag antenna on its holder, and recording the realized gain. Fig. 5.6c shows the resulting values compared to the simulation considering, $\epsilon = 1.3$ and $\tan\delta = 0.03$. Also in this case the results are in good agreement, evidencing the designed main radiation direction tilt of about 30°.

## 5.4 Temperature measurements

As a last step, temperature measurements were performed while the tag antenna was worn on a subject, to validate also the reading capability of the proposed tag antenna.

In order to confirm the soundness of the forehead choice as targeted spot, the tag was placed in the different body parts shown in Fig. 5.5 (for the chest case, the tag was placed underneath the t-shirt to insure skin contact). Temperature data were collected by means of a special designed software (property of Radiosense s.r.l., Italy) and a commercial reader. To reproduce a real case scenario, a fast acquisition of about 20 second was made for each position. The software was programmed to have a sample rate of 12 samples per second. Finally, the measurements were compared to the one obtained using a commercially available infrared tympanic thermometer.

Fig. 5.7a shows the resulting temperature values. The values recorded on the arm and on the chest are substantially coincident, having values oscillating between 31.5°C and 32°C for the chest and 31.75°C and 31.25°C for the arm. Therefore, an offset of about 5°C was recorded in comparison with the thermometer, which value was 36.9°C. As expected, the temperature data recorded on the fronthead, oscillating between 34.75°C and 35°C are closer to the one of the thermometer, having an offset of about 2°C. Moreover, this temperature recording is resulted to be the most stable, having less oscillations respect to the other two. The presence of this offset, towards lower temperatures was already reported in [134], and it

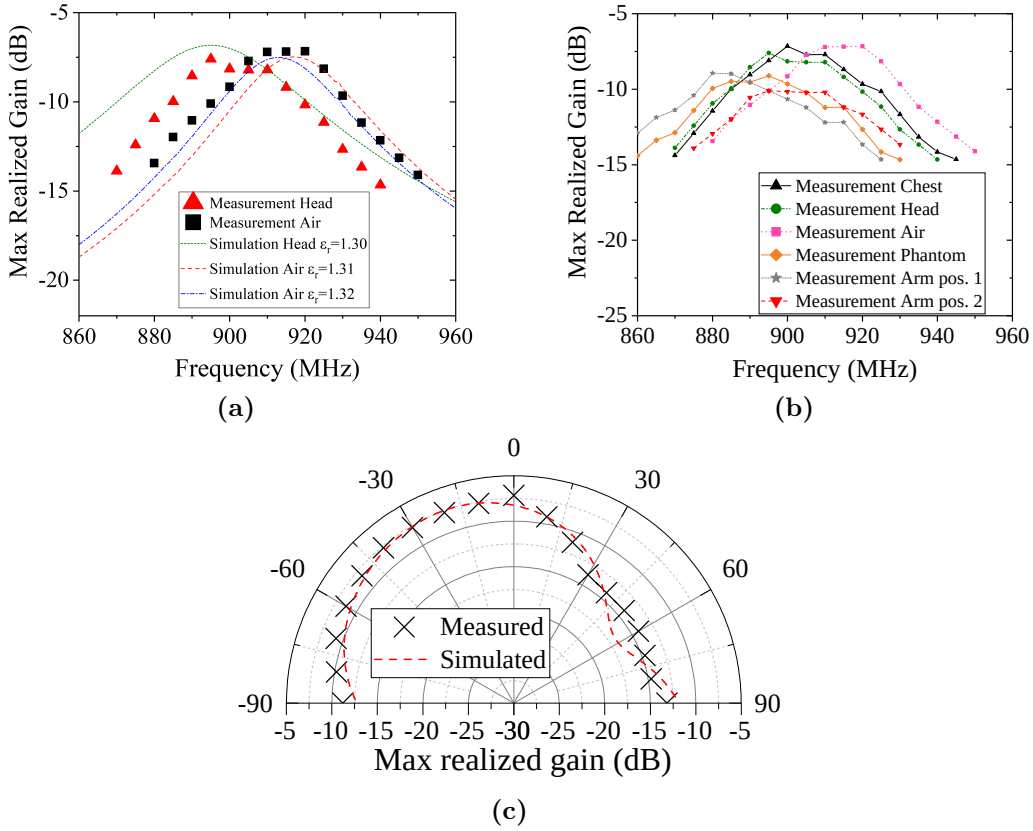


**Figure 5.6** – The measured realized gain: The comparison between measurements and simulations in air and on the head (a), the obtained realized gain for different tag placements on the body (b) and the measured radiation pattern for $\phi = 90°$ in air (c).

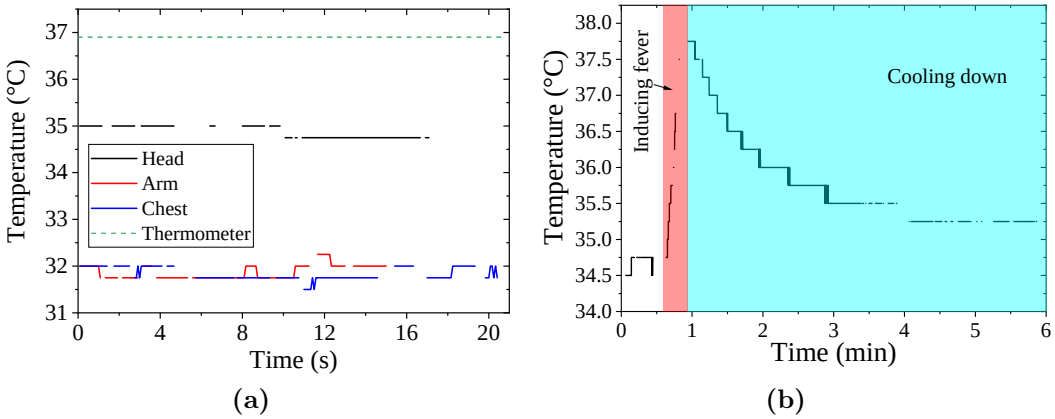


**Figure 5.7** – The validation of the temperature monitoring system: the comparison between the wirelessly acquired temperature, in different spots, with an infrared tympanic thermometer (a) and the skin recorded temperature, on the head, while a fever was induced (b).

can be easily removed using a calibration procedure [133]. Beside the offset due to the non-calibration, a difference between the tympanic and forehead measurements has to be expected, since the infrared thermometer measures the internal tympanic temperature, generally having higher value than the skin temperature.

As a final validation, the tag was tested in case of a body temperature increase, and a subsequently decrease. To obtain this, the tag antenna was worn by a subject and monitored, with the same equipment and settings than last experiment. The skin temperature, without the presence of the antenna, was increased by means of a hairdryer for about 20 seconds, in order to simulate the advent of a fever. Then, the subsequently temperature decrease was observed during about 5 minutes.

The resulting collected temperature data are shown in Fig. 5.7b. Starting from an initial value that oscillates between 34.5 and 34.75°C, a clear temperature increase was observed during the fever induction. Also the temperature decrease was observed, that reached a value of 35.25°C after 6 minutes. The chip resolution of 0.25°C can be clearly observed during this cooling time. From these results it can be concluded that the proposed wireless temperature monitoring system is capable to register temperature shifts, due to the presence of a fever.

## 5.5 Conclusion

The fifth chapter presents an extension of the complementary split ring resonator antenna presented in chapter 2 to human applications. In particular it proposes an ultra-low-cost temperature monitoring device to allow mass screening for example in case of epidemic emergencies in remote areas.

The design constraints were defined and, starting from them, a sticker antenna, out of adhesive copper tape, is presented. This device can be attached to a widely available cardboard substrate, in order to form the antenna. The design of the device was optimized by means of simulations. In particular, design attention has been dedicated to the robustness of the tag faced to oscillation of the dielectric properties of the substrate.

The resulting design, having a footprint of 75x45 $mm^2$, has been developed and tested in different scenarios. The resulting RR of about 1.2 m, in air and with the antenna placed on the head, is high enough to allow easy measurement by readers mounted over doors or on ceilings.

Finally, temperature measurements have been carried out. The resulting data show that the device needs to be calibrated but it is suitable for temperature monitoring.

# Conclusion

This dissertation describes the results of the research carried out during this three year PhD work. During this period, novel hybrid strategies to power an implantable medical device, including one autonomous and one wireless power transfer harvesting technique, have been proposed. Passive wearable sensors have been implemented to continuously monitor the body activity, with application in laboratory rodents and human subjects. First of all, the selected power harvesting technique, the Biofuel cell (BFC), has been successfully monitored *in-vivo*, thanks to a proposed measurement setup. Moreover, the concept of the hybrid device has been validated through measurements and design improvement, on the Electromagnetic (EM) side, has been achieved. Finally, a passive wearable Radio Frequency Identification (RFID) tag was proposed to perform body temperature screening with ultra-low cost devices.

## Synthesis

**Chapter 1:** The first chapter reviewed the necessary knowledge on the subjects taken into account during this work, describing different aspects of the implantable and wearable medical devices. Regarding the first, some possible applications have been presented, as well as the different power approaches that can be used to avoid the presence of batteries. Special attention has been paid to hybrid powered devices and the strategies that can be carried out to improve the implants performances. For the wearable case, the emphasis has been placed on the batteryless long-range RFID sensor tags, subject of this work. A review of the proposed sensing devices present in literature is presented, as well as the main design parameters that have to be taken into account. In this chapter, the foundations of this dissertation have been laid.

**Chapter 2:** The second chapter presents a batteryless Ultra High Frequency (UHF) RFID communication link in order to monitor a BFC implanted in a laboratory rodent. Four different antennas have been designed and developed, all with different characteristics. In particular, priority has been assigned to the independence of the antenna parameters from the biological medium for one design, and the wearability for the key feature of the last two antennas. Simulations have been performed and all the designs have been validated by measurements. As final result of this part, two implanted electrodes, modified with enzymes, have been monitored *in-vitro* and *in-vivo* on a laboratory rat, free to move inside its cage.

**Chapter 3:** In the third chapter, the development process of the hybrid powered device has first led to the definition of some design constraints. Thanks to that, the concept of a Biofuel Cell Antenna (BCA) has been proven. The resulting BFC provided 0.35 µW and the maximum achieved Power Transfer Efficiency (PTE) was 0.5% at a transmitter/receiver distance of 2 cm. Both of these values are not representative of the state of the art, e.g. in the order of 500 µW for the BFC, therefore intensive optimization is still needed. Moreover, an high-Q 2-coil mm-sized resonator has also been proposed. This structure has a Q-factor of 61.4 when placed in a PBS solution, improving the performances with respect to other structures present in the literature. To achieve this result, the device has been coated with a silicon rubber, not permitting the development of a BFC on the coils.

**Chapter 4:** In the fourth chapter, a dielectric structure has been proposed, in order to improve the Q factor of an implanted coil while it remains in contact with the surrounding medium, e.g. the body tissue, avoiding the complete implant encapsulation, and thus compatible with BFC development. The proposed design has been simulated and measured with comparable results and performance improvements have been recorded with respect to bare metal case in a tissue-like medium. This design was then optimized for a constant volume, including the dielectric structure. Simulations, confirmed by measurements, led to conclude that the best design is the one that ensures maximum coil radius, to maximize the coupling factor, and minimum possible difference between the dielectric structure radius and the coil radius ($\Delta d$) within the volume constraint, to maximize the Q factor. An improvement of the defined Figure of Merit (FoM) has been achieved including the defined geometry. Finally, to validate a possible application, impedance measurement has been successfully carried out on a swine heart.

**Chapter 5:** The last chapter presents the design of a ultra-low cost UHF-RFID tag with temperature monitor capabilities. The designed structure presents itself as a single adhesive copper tape sticker that can be attached to random cardboard substrate. Also in this case the device has been simulated and measured, leading to a Reading Range (RR) of about 1.2 m when measured in air or on the forehead. Finally, temperature measurements where carried out, validating the sensing capabilities of the designed RFID tag.

# Perspectives

## *In-vivo* rat monitoring

The measurement platform proposed for the BFC monitoring in laboratory rodent led to a successfully measurement, evidencing the potentiality of this technology. Starting from the proposed structure, many improvements can be envisaged, on both hardware and software sides. In the reader software side, not subject of this study, it can be modified in order to allow the monitoring, at the same time, of more than one rat. This will improve the system monitoring capabilities, e.g.

by placing two rats in the same cage. On the other hand, to achieve this, also the tag lodgement has to be redesigned, to improve the mechanical robustness of the device for the presence of many animals in the same cage. The software routine can also be improved by including the temperature measurement when voltage monitoring is carried out. This may allow a possible correlation between voltage and animal temperature shifts. In this case, hardware modifications are required, in order to ensure the physical contact between the RFID Integrated Circuit (IC) and the animal skin, to properly monitor the temperature. This, can be easily achieved by soldering the IC and the electrodes connector on the two different sides of the tag and use the antenna designed to be placed at 1 mm distance with the rat skin. Moreover, the tag design can be edited to include a load resistance placed in parallel with the sensor inputs, to allow the monitoring of the power delivered by the biofuel. Finally, the RR of the whole system can be improved by using last generation chips with sensor interfaces, e.g. [191], that have higher sensitivity with respect to the selected IC. On the counterpart, in this case, the embedded temperature sensor will be lost, and both reader software and antenna tag need to be redesigned, in order to be compatible with the new chip.

### Biofuel cell antenna

This work validated the feasibility of the BCA concept, with the hybrid capability implemented in the same receiver structure. Moreover, a first optimization, in the Radio Frequency (RF) side, has been carried out. Starting from the results achieved, many future works can be envisaged, towards a complete operability of this device. First of all, regarding the electrochemistry side, the stability of the BFC needs to be highly improved. Indeed, the lifetime of this device in one of the most critical aspects to develop a true alternative to batteries. Moreover, the enzyme deposition needs to be optimized, to improve the repeatability and to insure an homogeneous coating of the electrodes. This is specially true when microporous electrodes will be used in the device design, needed to achieve higher harvested power. The two upgrades achievable in the short term are the development of a device using microporous electrodes and the Threaded-Furrow Geometry (TFG), in order to improve the BFC and the Wireless Power Transfer (WPT) features of the implant, respectively. In particular, for the latter, a two-coil receiver can be implemented, in order to provide the two electrodes and to improve the Q factor of the structure. To achieve this, the coupling between the two implanted coils needs to be optimized, to ensure the maximum power to the load. Beside these aspects, the implant circuit has to be designed and added, it will collect and merge the two harvested energies to power the sensing/actuator/stimulating circuit. Finally, to complete the whole system, the transmitter coil has to be optimized to ensure the higher possible magnetic field to the implant while respecting the regulations on the transmitted power. Once the system will be optimized in all the aspects, it can be used to design an actual working implant, e.g. glucose monitoring system, stimulator, sensing system, etc..

### Threaded-Furrow geometry

Alongside the BCA application, the proposed structure may be used to implement different implanted devices with a simple and classical WPT scheme. In this case the one (or two) coil structure can be used as impedancemetry system, or for different applications. In continuity with the assertions of the last section, the circuital part of the implant needs to be designed.

### Cardboard tag antenna

Finally, the RFID tag presented in chapter 5 can be tested in a real-case scenario of mass temperature screening, in different environments characterised by different humidities. Moreover a special dedicated reader software can be implemented, in order to collect the temperature data, and to notify any anomaly in the monitored body temperature.

## Afterword

In order to bring innovative and groundbreaking solutions to improve the healthcare, in particular when electronics is involved, the classical research, considering one single aspect at a time, is no longer viable. It needs to step aside to allow the developing of high-multidisciplinary projects, where all the different research aspects are taken into account at the same time, in order to team up and overcome limitation that seemed insurmountable until recently. This dissertation is a good example of this new way of thinking the academic research, bringing totally different expertise to work together on a shared objective.

The high-multidisciplinary nature of this research project made this PhD work very challenging but, at the same time, very stimulating. Working on the borderline between electronics, biology, material science and electrochemistry has demanded continuous confrontations between completely different way of thinking and backgrounds, leading to - in my opinion - a mutual enriching experience. Sitting around a table and sharing the design needs and constraints from each side of the project, searching for the best trade-offs, requires flexibility and efforts to understanding point of views far from the *comfort zone*. Although these positive aspects, multidisciplinary projects can also easily lead to difficulties and frustrations, mainly due to the lack of elasticity and communication between and inside the different research partners, which forms the foundation of a good teamwork. In order to get the best from each domain, the work should be carried out in a shared way, with continuous discussions and design confrontations, and not independently, with each side focusing on its own results. This can lead to better and more *easily-reachable* research results, avoiding misunderstandings, and the needing of forced, and not anticipated, design adaptations on the fly during the developing process.

In conclusion, this three years work represents only the first steps in this new and very interesting topic for the MDA research team of the IMS laboratory, and I am glad to have been part of it. Having this opportunity has allowed me to widen my horizons, forcing me to always take into account the whole picture while making a new decision. This topic is far away from being completely covered and -

to me - this PhD work can be the starting point to the development of innovative solutions to improve the healthcare. With good improvements and keeping the communication as a priority, this field can be further explored, and it could lead to very interesting, and hopefully game-changing, results.

# Bibliography


[1] James B. Weitzman. "Electronic Medical Devices; A Primer for Pathologists". In: *Archives of Pathology & Laboratory Medicine* 127.7 (2003), pp. 814–825.

[2] J. Andreu-Perez et al. "From Wearable Sensors to Smart Implants-–Toward Pervasive and Personalized Healthcare". In: *IEEE Transactions on Biomedical Engineering* 62.12 (2015), pp. 2750–2762.

[3] Flavia Vitale and Brian Litt. "Bioelectronics: the promise of leveraging the body's circuitry to treat disease". In: *Bioelectronics in Medicine* 1.1 (2018), pp. 3–7.

[4] Cheng Chen et al. "Current and Emerging Technology for Continuous Glucose Monitoring". In: *Sensors (Basel, Switzerland)* 17.1 (2017), p. 182. ISSN: 1424-8220.

[5] Duarte Dias and João Paulo Silva Cunha. "Wearable Health Devices-Vital Sign Monitoring, Systems and Technologies". In: *Sensors (Basel, Switzerland)* 18.8 (2018), p. 2414.

[6] Rim Negra, Imen Jemili, and Abdelfettah Belghith. "Wireless Body Area Networks: Applications and Technologies". In: *Procedia Computer Science* 83 (2016), pp. 1274–1281.

[7] Jaemin Kim, Roozbeh Ghaffari, and Dae-Hyeong Kim. "The quest for miniaturized soft bioelectronic devices". In: *Nature Biomedical Engineering* 1 (2017), p. 0049.

[8] Achraf Ben Amar, Ammar B. Kouki, and Hung Cao. "Power Approaches for Implantable Medical Devices". In: *Sensors (Basel, Switzerland)* 15.11 (2015), pp. 28889–28914. ISSN: 1424-8220.

[9] Hatice Ceylan Koydemir and Aydogan Ozcan. "Wearable and Implantable Sensors for Biomedical Applications". In: *Annual Review of Analytical Chemistry* 11.1 (2018), pp. 127–146.

[10] Dennis Fitzpatrick. *Implantable Electronic Medical Devices*. Oxford: Academic Press, 2015.

[11] P. A. Catherwood, D. D. Finlay, and J. A. D. McLaughlin. "Intelligent Subcutaneous Body Area Networks: Anticipating Implantable Devices". In: *IEEE Technology and Society Magazine* 35.3 (2016), pp. 73–80.

[12] L. S. Y. Wong et al. "A very low-power CMOS mixed-signal IC for implantable pacemaker applications". In: *IEEE Journal of Solid-State Circuits* 39.12 (2004), pp. 2446–2456.

[13] Daniel R. Merrill, Marom Bikson, and John G. R. Jefferys. "Electrical stimulation of excitable tissue: design of efficacious and safe protocols". In: *Journal of Neuroscience Methods* 141.2 (2005), pp. 171–198.

[14] A. Kiourti and K. S. Nikita. "A Review of In-Body Biotelemetry Devices: Implantables, Ingestibles, and Injectables". In: *IEEE Transactions on Biomedical Engineering* 64.7 (2017), pp. 1422–1430.

[15] W. Greatbatch and C. F. Holmes. "History of implantable devices". In: *IEEE Engineering in Medicine and Biology Magazine* 10.3 (1991), pp. 38–41.

[16] D. Wessels. "Implantable pacemakers and defibrillators: device overview & EMI considerations". In: *2002 IEEE International Symposium on Electromagnetic Compatibility.* Vol. 2, 911–915 vol.2.

[17] Didier Klug et al. "Pacemaker Lead Infection in Young Patients". In: *Pacing and Clinical Electrophysiology* 26.7p1 (2003), pp. 1489–1493. ISSN: 0147-8389.

[18] Robert J. Russo et al. "Assessing the Risks Associated with MRI in Patients with a Pacemaker or Defibrillator". In: *New England Journal of Medicine* 376.8 (2017), pp. 755–764.

[19] Joshua Guag, Bisrat Addissie, and Donald Witters. "Personal medical electronic devices and walk-through metal detector security systems: assessing electromagnetic interference effects". In: *BioMedical Engineering OnLine* 16.1 (2017), p. 33.

[20] Dwight Reynolds et al. "A Leadless Intracardiac Transcatheter Pacing System". In: *New England Journal of Medicine* 374.6 (2015), pp. 533–541.

[21] Paula Sánchez et al. "Safety and usefulness of a second Micra transcatheter pacemaker implantation after battery depletion". In: *EP Europace* 21.6 (2019), pp. 885–885. ISSN: 1099-5129.

[22] Joel S. Perlmutter and Jonathan W. Mink. "DEEP BRAIN STIMULATION". In: *Annual Review of Neuroscience* 29.1 (2006), pp. 229–257.

[23] A. P. Amar et al. "Vagus Nerve Stimulation". In: *Proceedings of the IEEE* 96.7 (2008), pp. 1142–1151.

[24] Blake S. Wilson et al. "Better speech recognition with cochlear implants". In: *Nature* 352.6332 (1991), pp. 236–238.

[25] Derrick L. Cheng, Paul B. Greenberg, and David A. Borton. "Advances in Retinal Prosthetic Research: A Systematic Review of Engineering and Clinical Characteristics of Current Prosthetic Initiatives". In: *Current Eye Research* 42.3 (2017), pp. 334–347.

[26] Eberhart Zrenner et al. "Subretinal electronic chips allow blind patients to read letters and combine them to words". In: *Proceedings. Biological sciences* 278.1711 (2011), pp. 1489–1497.

[27] I. A. Mashhadi et al. "A New Wireless Power-Transfer Circuit for Retinal Prosthesis". In: *IEEE Transactions on Power Electronics* 34.7 (2019), pp. 6425–6439.

[28] D. J. Levinthal and K. Bielefeldt. "Systematic review and meta-analysis: Gastric electrical stimulation for gastroparesis". In: *Autonomic Neuroscience* 202 (2017), pp. 45–55.

[29] Saleem Islam et al. "Long-term outcomes of gastric electrical stimulation in children with gastroparesis". In: *Journal of Pediatric Surgery* 51.1 (2016), pp. 67–71.

[30] Jee Woong Lee et al. "Emerging Neural Stimulation Technologies for Bladder Dysfunctions". In: *Int Neurourol J* 19.1 (2015), pp. 3–11.

[31] Pauline Schaepelynck. "The Implantable Insulin Pump". In: *Handbook of Diabetes Technology*. Ed. by Yves Reznik. Cham: Springer International Publishing, 2019, pp. 47–55.

[32] Gavriel Iddan et al. "Wireless capsule endoscopy". In: *Nature* 405.6785 (2000), pp. 417–417.

[33] Ana-Maria Singeap, Carol Stanciu, and Anca Trifan. "Capsule endoscopy: The road ahead". In: *World journal of gastroenterology* 22.1 (2016), pp. 369–378.

[34] Hyunjoo J. Lee et al. "MEMS devices for drug delivery". In: *Advanced Drug Delivery Reviews* 128 (2018), pp. 132–147.

[35] Pui Mun Lee, Ze Xiong, and John Ho. "Methods for powering bioelectronic microdevices". In: *Bioelectronics in Medicine* 1.3 (2018), pp. 201–217.

[36] Bojing Shi, Zhou Li, and Yubo Fan. "Implantable Energy-Harvesting Devices". In: *Advanced Materials* 30.44 (2018), p. 1801511.

[37] Taher Ghomian and Shahab Mehraeen. "Survey of energy scavenging for wearable and implantable devices". In: *Energy* 178 (2019), pp. 33–49.

[38] Ross Kerley, Xiucheng Huang, and Dong Sam Ha. "Energy Harvesting from the Human Body and Powering up Implant Devices". In: *Nano Devices and Circuit Techniques for Low-Energy Applications and Energy Harvesting*. Ed. by Chong-Min Kyung. Dordrecht: Springer Netherlands, 2016, pp. 147–180.

[39] P. D. Mitcheson et al. "Energy Harvesting From Human and Machine Motion for Wireless Electronic Devices". In: *Proceedings of the IEEE* 96.9 (2008), pp. 1457–1486.

[40] Katrine Lundager et al. "Low Power Design for Future Wearable and Implantable Devices". In: *Journal of Low Power Electronics and Applications* 6.4 (2016), p. 20.

[41] Yang Yang, Xiao-Juan Wei, and Jing Liu. "Suitability of a thermoelectric power generator for implantable medical electronic devices". In: *Journal of Physics D: Applied Physics* 40.18 (2007), pp. 5790–5800.

[42] S. Koul, S. Ahmed, and V. Kakkar. "A comparative analysis of different vibration based energy harvesting techniques for implantables". In: *International Conference on Computing, Communication & Automation*, pp. 979–983.

[43] Zhengbao Yang et al. "High-Performance Piezoelectric Energy Harvesters and Their Applications". In: *Joule* 2.4 (2018), pp. 642–697.

[44] Faizan Ali et al. "Piezoelectric energy harvesters for biomedical applications". In: *Nano Energy* 57 (2019), pp. 879–902.

[45] S. Ahmed and V. Kakkar. "An Electret-Based Angular Electrostatic Energy Harvester for Battery-Less Cardiac and Neural Implants". In: *IEEE Access* 5 (2017), pp. 19631–19643.

[46] M. V. Tholl et al. "An Intracardiac Flow Based Electromagnetic Energy Harvesting Mechanism for Cardiac Pacing". In: *IEEE Transactions on Biomedical Engineering* 66.2 (2019), pp. 530–538.

[47] L. Bereuter et al. "Energy Harvesting by Subcutaneous Solar Cells: A Long-Term Study on Achievable Energy Output". In: *Annals of Biomedical Engineering* 45.5 (2017), pp. 1172–1180.

[48] Lodrick Makokha Wangatia et al. "Biomedical electronics powered by solar cells". In: *Current Opinion in Biomedical Engineering* (2019).

[49] Z. Chen et al. "A Single-Chip Solar Energy Harvesting IC Using Integrated Photodiodes for Biomedical Implant Applications". In: *IEEE Transactions on Biomedical Circuits and Systems* 11.1 (2017), pp. 44–53.

[50] E. Katz. "Implantable biofuel cells operating in vivo: Providing sustainable power for bioelectronic devices: From biofuel cells to cyborgs". In: *2015 6th International Workshop on Advances in Sensors and Interfaces (IWASI)*, pp. 2–13.

[51] Gymama Slaughter and Tanmay Kulkarni. "Enzymatic Glucose Biofuel Cell and its Application". In: *Journal of Biochips & Tissue Chips* 05.01 (2015).

[52] N. Mano, F. Mao, and A. Heller. "Characteristics of a Miniature Compartmentless Glucose-O2 Biofuel Cell and Its Operation in Living Plant". In: *Journal of the American Chemical Society* 125.21 (2003), pp. 6588–6594.

[53] Gymama Slaughter and Tanmay Kulkarni. "A self-powered glucose biosensing system". In: *Biosensors and Bioelectronics* 78 (2016), pp. 45–50.

[54] Gymama Slaughtr and Tanmay Kulkarni. "Highly Selective and Sensitive Self-Powered Glucose Sensor Based on Capacitor Circuit". In: *Scientific Reports* 7.1 (2017), p. 1471.

[55] A. F. Yeknami et al. "A 0.3-V CMOS Biofuel-Cell-Powered Wireless Glucose/Lactate Biosensing System". In: *IEEE Journal of Solid-State Circuits* 53.11 (2018), pp. 3126–3139.

[56] Serge Cosnier, Alan Le Goff, and Michael Holzinger. "Towards glucose biofuel cells implanted in human body for powering artificial organs: Review". In: *Electrochemistry Communications* 38 (2014), pp. 19–23.

[57] Denis Desmaële, Louis Renaud, and Sophie Tingry. "A wireless sensor powered by a flexible stack of membraneless enzymatic biofuel cells". In: *Sensors and Actuators B: Chemical* 220 (2015), pp. 583–589.

[58] M. Falk et al. "Self-powered wireless carbohydrate/oxygen sensitive biodevice based on radio signal transmission". In: *PLoS One* 9.10 (2014), e109104.

[59] A. Kobayashi et al. "An energy-autonomous bio-sensing system using a biofuel cell and 0.19V 53uW 65nm-CMOS integrated supply-sensing sensor with a supply-insensitive temperature sensor and inductive-coupling transmitter". In: *2016 IEEE Biomedical Circuits and Systems Conference (BioCAS)*. 2016, pp. 148–151.

[60] Alexander Kuhn and Matthias Heim. "Highly Ordered Macroporous Electrodes". In: *Springer Handbook of Electrochemical Energy*. Ed. by Cornelia Breitkopf and Karen Swider-Lyons. Berlin, Heidelberg: Springer Berlin Heidelberg, 2017, pp. 143–206.

[61] Feng Gao et al. "Engineering hybrid nanotube wires for high-power biofuel cells". In: *Nature Communications* 1.1 (2010), p. 2.

[62] Liu Deng et al. "A biofuel cell with enhanced performance by multilayer biocatalyst immobilized on highly ordered macroporous electrode". In: *Biosensors and Bioelectronics* 24.2 (2008), pp. 329–333.

[63] Abdelkader Zebda et al. "Challenges for successful implantation of biofuel cells". In: *Bioelectrochemistry* 124 (2018), pp. 57–72.

[64] K. Agarwal et al. "Wireless Power Transfer Strategies for Implantable Bioelectronics". In: *IEEE Reviews in Biomedical Engineering* 10 (2017), pp. 136–161.

[65] Muhammad Mujeeb-U-Rahman et al. "Optical power transfer and communication methods for wireless implantable sensing platforms". In: *Journal of Biomedical Optics* 20.9 (2015), pp. 1–9, 9.

[66] A. Saha et al. "A wireless optical power system for medical implants using low power near-IR laser". In: *2017 39th Annual International Conference of the IEEE Engineering in Medicine and Biology Society (EMBC)*, pp. 1978–1981.

[67] Caerwyn Ash et al. "Effect of wavelength and beam width on penetration in light-tissue interaction using computational methods". In: *Lasers in Medical Science* 32.8 (2017), pp. 1909–1918.

[68] Hamid Basaeri, David B. Christensen, and Shad Roundy. "A review of acoustic power transfer for bio-medical implants". In: *Smart Materials and Structures* 25.12 (2016), p. 123001.

[69] R. V. Taalla et al. "A Review on Miniaturized Ultrasonic Wireless Power Transfer to Implantable Medical Devices". In: *IEEE Access* 7 (2019), pp. 2092–2106.

[70] A. Ibrahim, M. Meng, and M. Kiani. "A Comprehensive Comparative Study on Inductive and Ultrasonic Wireless Power Transmission to Biomedical Implants". In: *IEEE Sensors Journal* 18.9 (2018), pp. 3813–3826.

[71] Shaul Ozeri and Doron Shmilovitz. "Ultrasonic transcutaneous energy transfer for powering implanted devices". In: *Ultrasonics* 50.6 (2010), pp. 556–566.

[72] Stanley B. Barnett et al. "The sensitivity of biological tissue to ultrasound". In: *Ultrasound in Medicine & Biology* 23.6 (1997), pp. 805–812.

[73] N. Shinohara. "Power without wires". In: *IEEE Microwave Magazine* 12.7 (2011), S64–S73.

[74] H. Kim et al. "Review of Near-Field Wireless Power and Communication for Biomedical Applications". In: *IEEE Access* 5 (2017), pp. 21264–21285.

[75] J. S. Ho, S. Kim, and A. S. Y. Poon. "Midfield Wireless Powering for Implantable Systems". In: *Proceedings of the IEEE* 101.6 (2013), pp. 1369–1378.

[76] C. Liu et al. "Design and Safety Considerations of an Implantable Rectenna for Far-Field Wireless Power Transfer". In: *IEEE Transactions on Antennas and Propagation* 62.11 (2014).

[77] Aqeel Mahmood Jawad et al. "Opportunities and Challenges for Near-Field Wireless Power Transfer: A Review". In: *Energies* 10.7 (2017), p. 1022.

[78] C. Gabriel, S. Gabriel, and E. Corthout. "The dielectric properties of biological tissues: I. Literature survey". In: *Physics in Medicine and Biology* 41.11 (1996), p. 2231.

[79] B. Lee and M. Ghovanloo. "An Overview of Data Telemetry in Inductively Powered Implantable Biomedical Devices". In: *IEEE Communications Magazine* 57.2 (2019), pp. 74–80.

[80] André Kurs et al. "Wireless Power Transfer via Strongly Coupled Magnetic Resonances". In: *Science* 317.5834 (2007).

[81] "IEEE Standard for Safety Levels with Respect to Human Exposure to Radio Frequency Electromagnetic Fields, 3 kHz to 300 GHz". In: *IEEE Std C95.1-2005 (Revision of IEEE Std C95.1-1991)* (2006), pp. 1–238.

[82] A. S. Y. Poon, S. O' Driscoll, and T. H. Meng. "Optimal Frequency for Wireless Power Transmission Into Dispersive Tissue". In: *IEEE Transactions on Antennas and Propagation* 58.5 (2010), pp. 1739–1750.

[83] Devansh R. Agrawal et al. "Conformal phased surfaces for wireless powering of bioelectronic microdevices". In: *Nature Biomedical Engineering* 1 (2017), p. 0043.

[84] S. Kim, J. S. Ho, and A. S. Y. Poon. "Wireless Power Transfer to Miniature Implants: Transmitter Optimization". In: *IEEE Transactions on Antennas and Propagation* 60.10 (2012), pp. 4838–4845. ISSN: 0018-926X.

[85] C. Liu, Y. Zhang, and X. Liu. "Circularly Polarized Implantable Antenna for 915 MHz ISM-Band Far-Field Wireless Power Transmission". In: *IEEE Antennas and Wireless Propagation Letters* 17.3 (2018), pp. 373–376.

[86] S. Bandyopadhyay and A. P. Chandrakasan. "Platform Architecture for Solar, Thermal, and Vibration Energy Combining With MPPT and Single Inductor". In: *IEEE Journal of Solid-State Circuits* 47.9 (2012), pp. 2199–2215.

[87] H. Uluşan et al. "A triple hybrid micropower generator with simultaneous multi-mode energy harvesting". In: *Smart Materials and Structures* 27.1 (2017), p. 014002.

[88] S. Chamanian et al. "Power-Efficient Hybrid Energy Harvesting System for Harnessing Ambient Vibrations". In: *IEEE Transactions on Circuits and Systems I: Regular Papers* 66.7 (2019), pp. 2784–2793.

[89] J. Katic, S. Rodriguez, and A. Rusu. "A High-Efficiency Energy Harvesting Interface for Implanted Biofuel Cell and Thermal Harvesters". In: *IEEE Transactions on Power Electronics* 33.5 (2018), pp. 4125–4134.

[90] A. Sanni, A. Vilches, and C. Toumazou. "Inductive and Ultrasonic Multi-Tier Interface for Low-Power, Deeply Implantable Medical Devices". In: *IEEE Transactions on Biomedical Circuits and Systems* 6.4 (2012), pp. 297–308.

[91] M. Meng and M. Kiani. "A Hybrid Inductive-Ultrasonic Link for Wireless Power Transmission to Millimeter-Sized Biomedical Implants". In: *IEEE Transactions on Circuits and Systems II: Express Briefs* 64.10 (2017), pp. 1137–1141.

[92] K. S. Guillory, A. K. Misener, and A. Pungor. "Hybrid RF/IR transcutaneous telemetry for power and high-bandwidth data". In: *The 26th Annual International Conference of the IEEE Engineering in Medicine and Biology Society.* Vol. 2, pp. 4338–4340.

[93] J. Charthad et al. "A mm-Sized Implantable Medical Device (IMD) With Ultrasonic Power Transfer and a Hybrid Bi-Directional Data Link". In: *IEEE Journal of Solid-State Circuits* 50.8 (2015), pp. 1741–1753.

[94] R. Shadid et al. "Hybrid Inductive Power Transfer and Wireless Antenna System for Biomedical Implanted Devices". In: *Progress In Electromagnetics Research C* 88 (2018), pp. 77–88.

[95] John S. Ho et al. "Wireless power transfer to deep-tissue microimplants". In: *Proceedings of the National Academy of Sciences* 111.22 (2014), pp. 7974–7979.

[96] H. Lhermet et al. "Efficient Power Management Circuit: From Thermal Energy Harvesting to Above-IC Microbattery Energy Storage". In: *IEEE Journal of Solid-State Circuits* 43.1 (2008), pp. 246–255.

[97] G. Chowdary, A. Singh, and S. Chatterjee. "An 18 nA, 87% Efficient Solar, Vibration and RF Energy-Harvesting Power Management System With a Single Shared Inductor". In: *IEEE Journal of Solid-State Circuits* 51.10 (2016), pp. 2501–2513.

[98] A. K. Ramrakhyani, S. Mirabbasi, and Chiao Mu. "Design and optimization of resonance-based efficient wireless power delivery systems for biomedical implants". In: *IEEE Trans Biomed Circuits Syst* 5.1 (2011), pp. 48–63.

[99] IFAC-CNR. *Dielectric proprierties of body tissues*. Accessed Sept. 14, 2019. URL: http://niremf.ifac.cnr.it/tissprop/htmlclie/htmlclie.php.

[100] Andreas Christ et al. "Assessing Human Exposure to Electromagnetic Fields From Wireless Power Transmission Systems". In: *Proceedings of the IEEE* 101.6 (2013), pp. 1482–1493.

[101] George C. McConnell et al. "Implanted neural electrodes cause chronic, local inflammation that is correlated with local neurodegeneration". In: *Journal of Neural Engineering* 6.5 (2009), p. 056003.

[102] U. Jow and M. Ghovanloo. "Design and Optimization of Printed Spiral Coils for Efficient Transcutaneous Inductive Power Transmission". In: *IEEE Transactions on Biomedical Circuits and Systems* 1.3 (2007), pp. 193–202.

[103] U. M. Jow and M. Ghovanloo. "Modeling and Optimization of Printed Spiral Coils in Air, Saline, and Muscle Tissue Environments". In: *IEEE Transactions on Biomedical Circuits and Systems* 3.5 (2009), pp. 339–347.

[104] Mohamad Sawan et al. "Multicoils-based inductive links dedicated to power up implantable medical devices: modeling, design and experimental results". In: *Biomedical Microdevices* 11.5 (2009), p. 1059.

[105] M. Kiani, U. M. Jow, and M. Ghovanloo. "Design and Optimization of a 3-Coil Inductive Link for Efficient Wireless Power Transmission". In: *IEEE Transactions on Biomedical Circuits and Systems* 5.6 (2011), pp. 579–591.

[106] R. F. Xue, K. W. Cheng, and M. Je. "High-Efficiency Wireless Power Transfer for Biomedical Implants by Optimal Resonant Load Transformation". In: *IEEE Transactions on Circuits and Systems I: Regular Papers* 60.4 (2013), pp. 867–874.

[107] K. Na et al. "Tracking Optimal Efficiency of Magnetic Resonance Wireless Power Transfer System for Biomedical Capsule Endoscopy". In: *IEEE Transactions on Microwave Theory and Techniques* 63.1 (2015), pp. 295–304.

[108] C. L. Yang et al. "Efficient Four-Coil Wireless Power Transfer for Deep Brain Stimulation". In: *IEEE Transactions on Microwave Theory and Techniques* 65.7 (2017), pp. 2496–2507.

[109] M. Schormans, V. Valente, and A. Demosthenous. "Practical Inductive Link Design for Biomedical Wireless Power Transfer: A Tutorial". In: *IEEE Transactions on Biomedical Circuits and Systems* 12.5 (2018), pp. 1112–1130.

[110] D. Ahn and M. Ghovanloo. "Optimal Design of Wireless Power Transmission Links for Millimeter-Sized Biomedical Implants". In: *IEEE Transactions on Biomedical Circuits and Systems* 10.1 (2016), pp. 125–137.

[111] A. Ibrahim and M. Kiani. "A Figure-of-Merit for Design and Optimization of Inductive Power Transmission Links for Millimeter-Sized Biomedical Implants". In: *IEEE Trans Biomed Circuits Syst* 10.6 (2016), pp. 1100–1111.

[112] Y. Cheng, G. Wang, and M. Ghovanloo. "Analytical Modeling and Optimization of Small Solenoid Coils for Millimeter-Sized Biomedical Implants". In: *IEEE Transactions on Microwave Theory and Techniques* 65.3 (2017), pp. 1024–1035.

[113] Ali M. Niknejad. *Electromagnetics for High-Speed Analog and Digital Communication Circuits*. Cambridge: Cambridge University Press, 2007.

[114] A. Mosenia et al. "Wearable Medical Sensor-Based System Design: A Survey". In: *IEEE Transactions on Multi-Scale Computing Systems* 3.2 (2017), pp. 124–138.

[115] F. BinDhim Nasser and Lyndal Trevena. "There's an App for That: A Guide for Healthcare Practitioners and Researchers on Smartphone Technology". In: *Online journal of public health informatics* 7.2 (2015), e218–e218.

[116] T. Liang and Y. J. Yuan. "Wearable Medical Monitoring Systems Based on Wireless Networks: A Review". In: *IEEE Sensors Journal* 16.23 (2016), pp. 8186–8199.

[117] A. Dionisi et al. "Autonomous Wearable System for Vital Signs Measurement With Energy-Harvesting Module". In: *IEEE Transactions on Instrumentation and Measurement* 65.6 (2016), pp. 1423–1434.

[118] Y. Chong et al. "Energy Harvesting For Wearable Devices: A Review". In: *IEEE Sensors Journal* (2019), pp. 1–1.

[119] P. Nepa and H. Rogier. "Wearable Antennas for Off-Body Radio Links at VHF and UHF Bands: Challenges, the state of the art, and future trends below 1 GHz". In: *IEEE Antennas and Propagation Magazine* 57.5 (2015), pp. 30–52.

[120] Yvan Duroc and Smail Tedjini. "RFID: A key technology for Humanity". In: *Comptes Rendus Physique* 19.1 (2018), pp. 64–71. ISSN: 1631-0705. URL: http://www.sciencedirect.com/science/article/pii/S1631070518300124.

[121] J.-M. Laheurte et al. *UHF RFID Technologies for Identification and Traceability*. Wiley, 2014.

[122] J. Fernandez-Salmeron et al. "Passive UHF RFID tag with multiple sensing capabilities". In: *Sensors (Basel)* 15.10 (2015), pp. 26769–82.

[123] M. Pasca et al. "UHF front-end feeding RFID-based body sensor networks by exploiting the reader signal". In: *Radio Science* 51.5 (), pp. 481–489.

[124] L. Wang et al. "Toward a Wearable RFID System for Real-Time Activity Recognition Using Radio Patterns". In: *IEEE Transactions on Mobile Computing* 16.1 (2017), pp. 228–242.

[125] S. Amendola, L. Bianchi, and G. Marrocco. "Movement Detection of Human Body Segments: Passive radio-frequency identification and machine-learning technologies". In: *IEEE Antennas and Propagation Magazine* 57.3 (2015), pp. 23–37.

[126] S. Acharya et al. "Ensemble Learning Approach via Kalman Filtering for a Passive Wearable Respiratory Monitor". In: *IEEE Journal of Biomedical and Health Informatics* 23.3 (2019), pp. 1022–1031.

[127] S. Amendola, V. Di Cecco, and G. Marrocco. "Numerical and Experimental Characterization of Wrist-Fingers Communication Link for RFID-Based Finger Augmented Devices". In: *IEEE Transactions on Antennas and Propagation* 67.1 (2019), pp. 531–540.

[128] Long Feiyuan et al. "Implementation and wireless readout of passive UHF RFID strain sensor tags based on electro-textile antennas". In: *2015 9th European Conference on Antennas and Propagation (EuCAP)*, pp. 1–5.

[129] Y. Liu et al. "An improved design of wearable strain sensor based on knitted RFID technology". In: *2016 IEEE Conference on Antenna Measurements & Applications (CAMA)*, pp. 1–4.

[130] D. Shuaib et al. "The possibilities of embroidered passive UHF RFID textile tags as wearable moisture sensors". In: *2017 IEEE 5th International Conference on Serious Games and Applications for Health (SeGAH)*, pp. 1–5.

[131] H. Habib et al. "Experimental study on UHF RFID tags integrated in medical bandage and paper-based materials". In: *2017 IEEE International Symposium on Antennas and Propagation & USNC/URSI National Radio Science Meeting*, pp. 2429–2430.

[132] A. P. Sample et al. "Design of an RFID-Based Battery-Free Programmable Sensing Platform". In: *IEEE Transactions on Instrumentation and Measurement* 57.11 (2008), pp. 2608–2615.

[133] S. Amendola et al. "Design, Calibration and Experimentation of an Epidermal RFID Sensor for Remote Temperature Monitoring". In: *IEEE Sensors Journal* 16.19 (2016), pp. 7250–7257.

[134] S. Milici et al. "Epidermal RFID passive sensor for body temperature measurements". In: *2014 IEEE RFID Technology and Applications Conference (RFID-TA)*, pp. 140–144.

[135] AMS. *SL900A tag chip datasheet*. 2018. URL: https://ams.com/documents/20143/36005/SL900A_DS000294_4-00.pdf/68d176d5-3c33-cd40-42d0-53c5de38b01f.

[136] EM-Microelectronics. *EM4325 tag chip datasheet*. Accessed Sept. 2, 2019. 2019. URL: https://www.emmicroelectronic.com/sites/default/files/products/datasheets/4325-ds_0.pdf.

[137] J. S. Besnoff et al. "Battery-free multichannel digital ECG biotelemetry using UHF RFID techniques". In: *2013 IEEE International Conference on RFID (RFID)*, pp. 16–22.

[138] A. Dementyev and J. R. Smith. "A wearable UHF RFID-based EEG system". In: *2013 IEEE International Conference on RFID (RFID)*, pp. 1–7.

[139] X. Lin and B. Seet. "Battery-Free Smart Sock for Abnormal Relative Plantar Pressure Monitoring". In: *IEEE Transactions on Biomedical Circuits and Systems* 11.2 (2017), pp. 464–473.

[140] A. Wickramasinghe et al. "Sequence Learning with Passive RFID Sensors for Real-Time Bed-Egress Recognition in Older People". In: *IEEE Journal of Biomedical and Health Informatics* 21.4 (2017), pp. 917–929.

[141] C. Miozzi et al. "A General-Purpose Small RFID Epidermal Datalogger for Continuous Human Skin Monitoring in Mobility". In: *2018 IEEE/MTT-S International Microwave Symposium - IMS*, pp. 371–373.

[142] M. C. Caccami et al. "Graphene oxide-based radiofrequency identification wearable sensor for breath monitoring". In: *IET Microwaves, Antennas & Propagation* 12.4 (2018), pp. 467–471.

[143] S. Nappi et al. "Flexible pH Sensor for Wireless Monitoring of the Human Skin from the Medimun Distances". In: *2019 IEEE International Conference on Flexible and Printable Sensors and Systems (FLEPS)*, pp. 1–3.

[144] P. V. Nikitin et al. "Power reflection coefficient analysis for complex impedances in RFID tag design". In: *IEEE Transactions on Microwave Theory and Techniques* 53.9 (2005), pp. 2721–2725.

[145] T. Kellomaki. "On-Body Performance of a Wearable Single-Layer RFID Tag". In: *IEEE Antennas and Wireless Propagation Letters* 11 (2012), pp. 73–76.

[146] S. Amendola and G. Marrocco. "Optimal Performance of Epidermal Antennas for UHF Radio Frequency Identification and Sensing". In: *IEEE Transactions on Antennas and Propagation* 65.2 (2017), pp. 473–481.

[147] C. Occhiuzzi, S. Cippitelli, and G. Marrocco. "Modeling, Design and Experimentation of Wearable RFID Sensor Tag". In: *IEEE Transactions on Antennas and Propagation* 58.8 (2010), pp. 2490–2498.

[148] Yang Li et al. "Wearable RFID-enabled sensor nodes for biomedical applications". In: *2008 58th Electronic Components and Technology Conference*, pp. 2156–2159.

[149] M. S. Islam et al. "Converting a Wireless Biotelemetry System to an Implantable System Through Antenna Redesign". In: *IEEE Transactions on Microwave Theory and Techniques* 62.9 (2014), pp. 1890–1897.

[150] Philippe Cinquin et al. "A Glucose BioFuel Cell Implanted in Rats". In: *PLOS ONE* 5.5 (2010), e10476.

[151] Jorge A. Castorena-Gonzalez et al. "Biofuel Cell Operating in Vivo in Rat". In: *Electroanalysis* 25.7 (2013), pp. 1579–1584.

[152] A. Zebda et al. "Single Glucose Biofuel Cells Implanted in Rats Power Electronic Devices". In: *Scientific Reports* 3 (2013), p. 1516.

[153] Sarra El Ichi-Ribault et al. "Remote wireless control of an enzymatic biofuel cell implanted in a rabbit for 2 months". In: *Electrochimica Acta* 269 (2018), pp. 360–366.

[154] Lucia Ardoino et al. "A radio-frequency system for in vivo pilot experiments aimed at the studies on biological effects of electromagnetic fields". In: *Physics in Medicine and Biology* 50.15 (2005), p. 3643.

[155] R. Meys and F. Janssens. "Measuring the impedance of balanced antennas by an S-parameter method". In: *IEEE Antennas and Propagation Magazine* 40.6 (1998), pp. 62–65.

[156] A. S. Meier and W. P. Summers. "Measured Impedance of Vertical Antennas over Finite Ground Planes". In: *Proceedings of the IRE* 37.6 (1949), pp. 609–616.

[157] Qing Xianming, Goh Chean Khan, and Chen Zhi Ning. "Impedance Characterization of RFID Tag Antennas and Application in Tag Co-Design". In: *IEEE Transactions on Microwave Theory and Techniques* 57.5 (2009), pp. 1268–1274.

[158] S. Zuffanelli et al. "On-metal UHF-RFID passive tags based on complementary split-ring resonators". In: *IET Microwaves, Antennas & Propagation* 11.7 (2017), pp. 1040–1044.

[159] Dae-Hyeong Kim et al. "Epidermal Electronics". In: *Science* 333.6044 (2011), pp. 838–843.

[160] John A. Rogers, Roozbeh Ghaffari, and Dae-Hyeong Kim. *Stretchable Bioelectronics for Medical Devices and Systems*. 1st ed. Springer, 2016.

[161] Ping Mei et al. "Digital Fabrication and Integration of a Flexible Wireless Sensing Device". In: *IEEE Sensors Journal* 17.21 (2017), pp. 7114–7122.

[162] Sabrina M. Smith and Matthew J. Zirwas. "Nonallergic Reactions to Medical Tapes". In: *Dermatitis* 26.1 (2015), pp. 38–43.

[163] A. Susanto et al. "Performance of Zn-Cu and Al-Cu Electrodes in Seawater Battery at Different Distance and Surface Area". In: *International Journal of Renewable Energy Research* 7.1 (), pp. 298–303.

[164] Stéphane Reculusa et al. "Design of Catalytically Active Cylindrical and Macroporous Gold Microelectrodes". In: *Advanced Functional Materials* 21.4 (2011), pp. 691–698.

[165] K. F. Gey. "The concentration of glucose in rat tissues". In: *The Biochemical journal* 64.1 (1956), pp. 145–150.

[166] J. Song et al. "Optimization of Wireless Sensors Based on Intermodulation Communication". In: *IEEE Transactions on Microwave Theory and Techniques* 61.9 (2013), pp. 3446–3452.

[167] M. Zargham and P. G. Gulak. "Fully Integrated On-Chip Coil in 0.13 µm CMOS for Wireless Power Transfer Through Biological Media". In: *IEEE Transactions on Biomedical Circuits and Systems* 9.2 (2015), pp. 259–271. ISSN: 1932-4545.

[168] Z. Liu, Z. Zhong, and Y. Guo. "In Vivo High-Efficiency Wireless Power Transfer With Multisine Excitation". In: *IEEE Transactions on Microwave Theory and Techniques* 65.9 (2017), pp. 3530–3540.

[169] F. S. Chute and F. E. Vermeulen. "A Visual Demonstration of the Electric Field of a Coil Carrying a Time-Varying Current". In: *IEEE Transactions on Education* 24.4 (1981), pp. 278–283. ISSN: 0018-9359.

[170] M. C. A. M. Koolen, J. A. M. Geelen, and M. P. J. G. Versleijen. "An improved de-embedding technique for on-wafer high-frequency characterization". In: *Proceedings of the 1991 Bipolar Circuits and Technology Meeting*. 1991, pp. 188–191.

[171] Joshua G. Travers et al. "Cardiac Fibrosis: The Fibroblast Awakens". In: *Circulation research* 118.6 (2016), pp. 1021–1040.

[172] E. F. J. Ring. "Progress in the measurement of human body temperature". In: *IEEE Engineering in Medicine and Biology Magazine* 17.4 (1998), pp. 19–24.

[173] R T Emond et al. "A case of Ebola virus infection". In: *British Medical Journal* 2.6086 (1977), pp. 541–544.

[174] F. Ibrahim et al. "Dengue fever (DF) and dengue haemorrhagic fever (DHF) symptoms analysis from an expert system perspective". In: *Proceedings. IEEE International Multi Topic Conference, 2001. IEEE INMIC 2001. Technology for the 21st Century.* Pp. 212–215.

[175] Roger Weber et al. "Knowledge, Attitudes and Practices of Business Travelers Regarding Malaria Risk and Prevention". In: *Journal of Travel Medicine* 10.4 (2006), pp. 219–224.

[176] Vallire D. Hooper and Jeannette O. Andrews. "Accuracy of Noninvasive Core Temperature Measurement in Acutely Ill Adults: The State of the Science". In: *Biological Research For Nursing* 8.1 (2006), pp. 24–34.

[177] Guanghao Sun et al. "Applications of Infrared Thermography for Noncontact and Noninvasive Mass Screening of Febrile International Travelers at Airport Quarantine Stations". In: *Application of Infrared to Biomedical Sciences*. Ed. by Eddie Y. K. Ng and Mahnaz Etehadtavakol. Singapore: Springer Singapore, 2017, pp. 347–358.

[178] W. Haines et al. "Wireless system for continuous monitoring of core body temperature". In: *2017 IEEE MTT-S International Microwave Symposium (IMS)*, pp. 541–543.

[179] T. Wu et al. "An Autonomous Wireless Body Area Network Implementation Towards IoT Connected Healthcare Applications". In: *IEEE Access* 5 (2017), pp. 11413–11422. ISSN: 2169-3536.

[180] K. V. S. Rao, P. V. Nikitin, and S. F. Lam. "Antenna design for UHF RFID tags: a review and a practical application". In: *IEEE Transactions on Antennas and Propagation* 53.12 (2005), pp. 3870–3876.

[181] R. Colella and L. Catarinucci. "Wearable UHF RFID Sensor-Tag Based on Customized 3D-Printed Antenna Substrates". In: *IEEE Sensors Journal* 18.21 (2018), pp. 8789–8795.

[182] I. Kharrat et al. "Low-Loss Paper Substrate for Printed High Efficiency Antennas at 2.45 GHz". In: *IEEE Antennas and Wireless Propagation Letters* 14 (2015), pp. 1400–1403.

[183] Jorge Marcondes. "Corrugated fibreboard in modified atmospheres: Moisture sorption/desorption and shock cushioning". In: *Packaging Technology and Science* 9.2 (1996), pp. 87–98.

[184] M. Sivakumar and D. D. Deavours. "A Dual-Resonant Microstrip Antenna for Paperboard in the Cold Chain". In: *2008 IEEE Sarnoff Symposium*. 2008, pp. 1–5.

[185] G. A. Casula et al. "Robustness of Wearable UHF-Band PIFAs to Human-Body Proximity". In: *IEEE Transactions on Antennas and Propagation* 64.5 (2016), pp. 2050–2055.

[186] Li Deng et al. "Alumina ceramic slot antenna for UHF RFID tag embedded in vehicles". In: *Microwave and Optical Technology Letters* 58.5 (2016), pp. 1150–1154.

[187] C. Occhiuzzi, S. Cippitelli, and G. Marrocco. "Modeling, Design and Experimentation of Wearable RFID Sensor Tag". In: *IEEE Transactions on Antennas and Propagation* 58.8 (2010), pp. 2490–2498.

[188] GS1. *Regulatory status for using RFID in the EPC Gen2 (860 to 960 MHz) band of the UHF spectrum*. Accessed: Sept. 2, 2019. 2019. URL: https://www.gs1.org/sites/default/files/docs/epc/uhf_regulations.pdf.

[189] P. V. Nikitin and K. V. S. Rao. "Theory and measurement of backscattering from RFID tags". In: *IEEE Antennas and Propagation Magazine* 48.6 (2006), pp. 212–218.

[190] AET Inc. 2019. URL: https://www.aetjapan.com/english/index.php?hardware.

[191] Farsens. *ROCKY100 tag chip datasheet*. Accessed Sept. 19, 2019. 2017. URL: http://www.farsens.com/wp-content/uploads/2017/12/DS-ROCKY100-V04.pdf.